PERFORMANCE OPTIMIZATION OF FLOATING OFFSHORE WIND TURBINE DESIGNS ALLOWING LARGE ROTATIONAL MOTIONS

A Dissertation

by

JU GAO

Submitted to the Office of Graduate and Professional Studies of
Texas A&M University
in partial fulfillment of the requirements for the degree of

DOCTOR OF PHILOSOPHY

Chair of Committee,	John Sweetman
Committee Members,	Jeffrey Falzarano
	Richard Mercier
	Ayal Anis
Head of Department,	Sharath Girimaji

December 2019

Major Subject: Ocean Engineering

ABSTRACT

A newly evolving concept in utility-scale floating wind turbines is investigated through design optimization. The ideal hull length is selected from seven new designs, based on optimizing the trade-off between minimizing structural weight and maximizing electricity harvest. The seven new spar-buoy designs have drafts ranging from 62 to 120 m. Each floater hull has been developed in conformance with industry-standard structural guide API Bulletin 2U. Performance is assessed with the Loose software using time-domain analysis and irregular winds and waves. The simulation method is based on multi-body theory in Euler-space, which does not rely on small-angle assumptions. Nonlinear hydrostatic restoring forces and moments are derived for large rotational angles in the pitch-roll-yaw Euler angle sequence. Environmental forcing by wind is computed using aero-elastic theory. A new individual pitch control (IPC) method based on DISCON control routine is investigated as a possible means to improve generating efficiency. The pitch angle of each blade is individually controlled relative to a mean angle computed by DISCON to maintain the ideal angle of attack by removing the angle change caused by inclining tower. A comparison of the generating efficiency between IPC and traditional collective pitch control shows that IPC is not an effective way to increase output power.

A new analytical far wake model for yawed or tilted wind turbines is developed based on the Joukowski transformation and conservation of momentum and mass. The wake cross section at any downstream distance is divided into a series of annular rings, inside which conservation of momentum is applied. The wake of a yawed or tilted wind turbine evolves into a kidney or oval shape, depending on the incoming wind speed and the angle of yaw or tilt. The Joukowski transformation is used to predict both kidney-shaped and oval far wakes. The analytical model is calibrated using numerical simulations computed for different angles of tilt and different wind speeds using a large eddy computational fluid dynamic model. The new wake model is easy to use and requires only minimal computational expense to predict the wake expansion shape and the varying velocity within the wake field. Comparison between the new wake model and numerical simulation results demonstrates that the newly developed wake model effectively predicts both the wake boundaries and the wake velocity deficit.

Fatigue damage is assessed for blades of floating offshore wind turbines operating on three different hull configurations using two different strain-based methods. The hull configurations are selected to cover a wide range of rotational stiffness. Nonlinear beam theory is applied to compute the 3-D beam displacements along the turbine blades. Time histories of the same beam displacements are converted to maximum principal strains and to normal strains, and then the maximum principal strain method, one of the commonly used multiaxial fatigue analysis methods, and the normal strain method are used to compute the fatigue damage of the blade shell, respectively. Results show that the two methods yield meaningfully different predictions of fatigue lives and locations of fatigue failures. The normal strain method significantly underpredicts fatigue damage compared with the maximum principal strain method. Blade fatigue on floaters with very low rotational stiffness is found to be worse than on those with moderate rotational stiffness.

Performance of downstream FOWT's in the wakes of upstream turbines is assessed including electricity harvest and structural resonant responses. Results demonstrate that wakes have significant impact on power generation of downstream turbines and can excite resonant responses of platforms.

DEDICATION

To my parents and my best friends for their trust, support and sacrifice.

ACKNOWLEDGMENTS

First of all, I would like to express my sincere thanks to my advisor, Prof. John Sweetman, for his invaluable advice, support, and encouragement during my study at Texas A&M University. I appreciate all his guidance that helped me solve and correct all the problems I've met during my research. My thanks go to him for editing my paper so many times with great patience and guiding me how to write better papers.

I would like to thank all the professors who have taught me and helped me with my research, Prof. Richard Mercier, Prof. Jeffrey Falzarano, Prof. Anis, Prof. Juan J. Horrillo, and Prof. A. Wood. Prof. Mercier's course named Dynamic Offshore Structures is one of the most helpful courses for my offshore studies. Both Prof. Mercier and Prof. Falzarano's advice on the dynamic resonant influences between turbines of the proposal of my preliminary exam is highly important and useful. Prof. Anis's suggestion that the current should also be included in the study of dynamic response of offshore structures is necessary and helpful. Prof. Horrillo has provided guidance and help for my computational fluid dynamic study. Prof. Wood has given advice on my dissertation.

I want to thank the technical lab coordinator, Mr. Cory Froelich, and the Help Desk staff of Texas A&M High Performance Research Computing. I really appreciate all the technical and timely help from them.

I would also like to thank the professors who offered me the opportunity to be a teaching assistant at Texas A&M University, which lets me practice my teaching skills.

Last but not the least, I would like to thank my parents and my dearest friends for their support and encouragement all the time. I would like to thank my friend Altaf for her great advice on my presentation. I appreciate and treasure the memory of spiritual support from Weijia, who encouraged me to continue my education all the time.

CONTRIBUTORS AND FUNDING SOURCES

Contributors

This work was supported by a dissertation committee consisting of Professor John Sweetman (advisor), Jeffrey Falzarano, and Richard Mercier of the Department of Ocean Engineering and Professor Ayal Anis of the Department of Marine Sciences.

All work for the dissertation was completed by the student, under the advisement of John Sweetman of the Department of Ocean Engineering.

Funding Sources

This work was made possible in part by the National Science Foundation under Grant Number CBET-1133682.

Its contents are solely the responsibility of the authors and do not necessarily represent the official views of the National Science Foundation.

NOMENCLATURE

ABL	Atmospheric Boundary Layer
BEM	Blade Element Momentum
CFD	Computational Fluid Dynamic
CFL	Courant-Friedrichs-Lewy
CPC	Collective Pitch Control
CVP	Counter-rotating Vortex Pair
DEL	Damage-equivalent Load
FEM	Finite Element Method
EOM	Equation of Motion
FOWF	Floating Offshore Wind Farm
FOWT	Floating Offshore Wind Turbine
GDW	Generalized Dynamic Wake
IEC	International Electrotechnical Commission
IPC	Individual Pitch Control
LES	Large Eddy Simulation
MBBT	Momentum-based Beam Theory
MCM	Momentum Cloud Method
NREL	National Renewable Energy Laboratory
OpenFOAM	Open Source Field Operation and Manipulation
SOWFA	Simulator for Wind Farm Applications
SWL	Still Water Level

TABLE OF CONTENTS

Page

ABSTRACT ii

DEDICATION iv

ACKNOWLEDGMENTS v

CONTRIBUTORS AND FUNDING SOURCES vi

NOMENCLATURE vii

TABLE OF CONTENTS viii

LIST OF FIGURES xi

LIST OF TABLES xv

1. INTRODUCTION AND LITERATURE REVIEW 1

  1.1 Introduction 1
  1.2 Literature Review 2
  1.3 Mathematical Background 6
    1.3.1 Environmental Conditions 7
      1.3.1.1 Wave Conditions 7
      1.3.1.2 Wind Conditions 8
    1.3.2 Theoretical Wake Deficit Models 9
    1.3.3 Large Eddy Simulation Method 10
    1.3.4 Fatigue Analysis 12
  1.4 Unique Contribution 13
  1.5 Organization of Dissertation 14

2. DESIGN OPTIMIZATION OF HULL SIZE FOR SPAR-BASED FLOATING OFFSHORE WIND TURBINES 16

  2.1 Introduction 16
  2.2 Seven New Floater Designs Conforming to API Practice 19
  2.3 Nonlinear Hydrostatics 22
  2.4 Individual Pitch Control 27
  2.5 Simulation Methodology 30
    2.5.1 Momentum Cloud Method 30
    2.5.2 Restoring Loads from Mooring Lines 31

2.5.3 Wind Loads 32
2.5.4 Wave Loads 32
2.6 Performance of the Seven New Designs 33
2.7 Conclusions 45

3. A SEMI-EMPIRICAL WAKE MODEL FOR YAWED OR TILTED WIND TURBINES BASED ON THE JOUKOWSKI TRANSFORMATION 47

3.1 Introduction 47
3.2 Derivation, Calibration, and Application of the Wake Model for a Yawed or Tilted Turbine 52
3.2.1 Derivation of the Joukowski-transformation-based Wake Model 52
3.2.2 Calibration of the Parameters of the Joukowski Transformation 58
3.2.2.1 Parameters for a Kidney Shape 59
3.2.2.2 Parameters for an Oval Shape 60
3.2.3 Application of the Joukowski-transformation-based Wake Model 60
3.3 Validation of the Joukowski-transformation-based Wake Model Using Simulation Results 61
3.3.1 Simulation Models 61
3.3.2 Comparison between the Joukowski-transformation-based Wake Model and Simulation Results 64
3.3.3 Wake Expansion and Shift 69
3.3.4 Vertical and Spanwise Wake Profiles 71
3.3.5 Application of the Wake Model to Calculate Power Generation and Fatigue Loading 74
3.4 Conclusions 79

4. MULTIAXIAL FATIGUE ASSESSMENT OF FLOATING OFFSHORE WIND TURBINE BLADES OPERATING ON COMPLIANT FLOATING PLATFORMS 81

4.1 Introduction and Background 81
4.1.1 Introduction 81
4.1.2 Background 84
4.1.2.1 Simulation of FOWT System 85
4.1.2.2 Momentum-based Beam Theory 85
4.1.2.3 Parameterization of Multiaxial Loading 88
4.1.2.4 Fatigue Life Prediction 88
4.2 Methodology 89
4.2.1 Strain Calculation at a Point 89
4.2.2 Computation of Fatigue Damage 90
4.3 Fatigue Analysis 91
4.3.1 Numerical Simulation Models 91
4.3.1.1 FOWT Models 91
4.3.1.2 Material of Blade Shells 92
4.3.1.3 Environmental Loading 94
4.3.2 Results of Fatigue Analysis 96

        - 4.3.2.1 Fatigue Damage 96
        - 4.3.2.2 Comparison of Strains 102
  - 4.4 Conclusions 106

5. ASSESSMENT OF POWER GENERATION AND RESONANCE RESPONSES OF DOWNSTREAM TURBINES 107
  - 5.1 Introduction 107
  - 5.2 Simulation Results 108
    - 5.2.1 Power Generation 109
    - 5.2.2 Resonance of Downstream FOWT's 113
  - 5.3 Conclusions 117

6. SUMMARY AND CONCLUSIONS 118
  - 6.1 Summary and Conclusions 118
  - 6.2 Future Work 120

REFERENCES 121

APPENDIX A. COEFFICIENTS OF NONLINEAR HYDROSTATIC STIFFNESS MATRIX 133

APPENDIX B. INTERACTION OF WAVES AND CURRENTS AND WAVE STRETCHING 135
  - B.1 Mathematical Background 135
    - B.1.1 Interaction of Waves and Currents 135
    - B.1.2 Wheeler Stretching 136
  - B.2 Simulation Results 136

LIST OF FIGURES

FIGURE Page

1.1 Shapes of blade cross sections. 3

2.1 General view of seven new floaters. Reprinted with permission from Springer [10]. 21

2.2 Comparison of hull pitch displacements at rated wind speed. Reprinted with permission from Springer [10]. 22

2.3 Inertial and body-fixed coordinate systems in Loose. Reprinted with permission from Springer [10]. 23

2.4 Blade geometry for analysis of a horizontal axis wind turbine. Reprinted with permission from Springer [10]. 28

2.5 Incoming wind acting on wind turbine. Reprinted with permission from Springer [10]. 29

2.6 Floater draft VS power. Reprinted with permission from Springer [10]. 35

2.7 Pitch displacements of platforms VS power. Reprinted with permission from Springer [10]. 36

2.8 Comparison of rotor speed at rated wind speed. Reprinted with permission from Springer [10]. 37

2.9 Comparison of output power at rated wind speed. Reprinted with permission from Springer [10]. 37

2.10 Comparison of blade pitch angle at rated wind speed. Reprinted with permission from Springer [10]. 38

2.11 Total weight-cost per unit power output for nine wind speeds. Reprinted with permission from Springer [10]. 39

2.12 Percentage reduction in weight-cost (WR) VS percentage reduction in electricity harvest (PR). Reprinted with permission from Springer [10]. 40

2.13 Attack angle comparison between CPC and IPC for model with 74 m draft at 13 m/s constant wind speed with constant platform pitch angle. Reprinted with permission from Springer [10]. 41

2.14 Axial induction factor comparison between CPC and IPC for model with 74 m draft at 13 m/s constant wind speed with constant platform pitch angle. Reprinted with permission from Springer [10]. 41

2.15 Blade Pitch Angle of CPC for model with 74 m draft at 13 m/s constant wind speed with constant platform pitch angle. Reprinted with permission from Springer [10]. .. 42

2.16 Blade Pitch Angle of IPC for model with 74 m draft at 13 m/s constant wind speed with constant platform pitch angle. Reprinted with permission from Springer [10]. .. 42

2.17 Attack angle comparison between CPC and IPC for model with 74 m draft at 13 m/s mean wind speed. Reprinted with permission from Springer [10]. 43

2.18 Axial induction factor comparison between CPC and IPC for model with 74 m draft at 13 m/s mean wind speed. Reprinted with permission from Springer [10]. 43

2.19 Power comparison between CPC and IPC for model with 74 m draft at 13 m/s mean wind speed. Reprinted with permission from Springer [10]. 44

3.1 Wake flow of a turbine with an inclining tower. 49

3.2 Control volume of wake flow of a tilted turbine. 53

3.3 Circle to kidney shape. 56

3.4 Circle to oval. 57

3.5 Simulation flow domain. 62

3.6 Normalized streamwise velocity on the Y-Z plane at various distances downstream for FOWT with 74 m draft subject to 11 m/s wind speed. 65

3.7 Normalized streamwise velocity at X=7D. 66

3.8 Normalized streamwise velocity profile along spanwise direction at X=7D, Z=Wake Center. 67

3.9 Normalized average wake velocity inside wake boundary at X=7D. 68

3.10 Comparison of wake radii. 70

3.11 Comparison of wake center trajectories for twelve cases. 71

3.12 Vertical profiles of normalized streamwise velocity at X=7D, Y=0D. 72

3.13 Normalized streamwise velocity profile along the spanwise direction at X=7D, Z=Hub Height. 73

3.14 Normalized streamwise velocity profile along the spanwise direction at X=7D, Z=153 m. 74

3.15 Comparison of wake center shift using CFD and Jiménez's wake model. 75

3.16 Rotor speeds computed in the wake of four methods. 76

3.17 Power generation computed in the wake of four methods. 77

3.18 Maximum principal strains computed in the wake of four methods. 78

4.1 Coordinate systems. 86
4.2 CLD of S1 with R=10, R=-1, R=0.1. Reprinted from [1]. 93

4.3 Weibull distribution of wind speeds at $(-20°, 45°)$. 95

4.4 Point experiencing maximum fatigue damage at section 15 based on the maximum principal strain method. 98

4.5 Points experiencing maximum fatigue damages at section 8 based on the normal strain method. 99

4.6 Strains at section 8 of the turbine with 74 m draft at 12 m/s wind. 102

4.7 Strains at section 15 of the turbine with 74 m draft at 12 m/s wind. 103

4.8 Maximum principal and normal strains of the turbine with 74 m draft at 12 m/s wind. 104

4.9 Maximum principal and normal strains at section 8 of the turbine with 74 m draft at 12 m/s wind. 105

4.10 Maximum principal and normal strains at section 15 of the turbine with 74 m draft at 12 m/s wind. 105

5.1 Locations of downstream wind turbines. 109

5.2 Comparison of pitch displacements, rotor speeds, and power output of FOWT's with 74 m draft among turbine locations (1) to (6) at 9 m/s wind. 110

5.3 Comparison of pitch displacements, rotor speeds, and power output of FOWT's with 74 m and 120 m drafts among turbine locations (4) to (6) at 9 m/s wind. 111

5.4 Comparison of pitch displacements, rotor speeds, and power output of FOWT's with 74 m and 120 m drafts among turbine locations (4) to (6) at 13 m/s wind. 112

5.5 Comparison of pitch displacements, rotor speeds, and power output of FOWT's with 74 m draft among turbine locations (4) to (9) at 9 m/s wind. 113

5.6 Displacements of the downstream turbine with 74 m draft at 9 m/s wind. 115

5.7 Displacements of downstream turbine with 74 m draft at 13 m/s wind. 115

5.8 Power spectrum of displacements of downstream turbine with draft 74 m under 9 m/s wind. 116

5.9 Power spectrum of displacements of downstream turbine with draft 74 m under 13 m/s wind. 116

B.1 Comparison of hull pitch displacement for five cases under normal condition. 137

B.2 Comparison of hull roll displacement for five cases under normal condition. 138

B.3 Comparison of output power for five cases under normal condition. 138

B.4 Comparison of hull pitch displacement for cases without wind loads. 139

B.5 Comparison of hull roll displacement for cases without wind loads. 139

B.6 Comparison of hull pitch displacement for five cases under extreme condition. 140

B.7 Comparison of hull roll displacement for five cases under extreme condition. 141

LIST OF TABLES

TABLE Page

2.1 Parameters of seven new floaters. Reprinted with permission from Springer [10]..... 20

2.2 Parameters of T-section rings of floaters. Reprinted with permission from Springer [10]........ 20

2.3 Significant wave heights and peak periods relevant to hub-height wind speeds. Reprinted with permission from Springer [10]........ 34

3.1 Mean platform pitch angles relevant to hub-height wind speeds for three FOWT designs........ 63

3.2 Mean thrust coefficient, wake expansion factor, and wake center shift distance....... 69

3.3 Mean rotor speed, mean power generation, and 1-day fatigue damage 79

4.1 Locations of 23 cross sections........ 92

4.2 Properties of material S1. Reprinted from [1]. 93

4.3 Probabilities, peak periods, and significant wave heights associated with hub-height wind speeds........ 96

4.4 Maximum fatigue damage of each FOWT at each wind speed 97

4.5 Maximum fatigue damage corresponding to frequency of each wind speed..........101

1. INTRODUCTION AND LITERATURE REVIEW

1.1 Introduction

Wind is an increasingly important source of renewable energy that is presently undergoing a period of rapid expansion worldwide. New technologies continue to be developed for offshore floating wind as new wind farms are sited in increasingly deep waters. The world's first full-scale floating wind farm was installed and began to deliver electricity to the northeast coast of Scotland in 2017 [2], each of five 6-MW wind turbines is supported by a spar-type floater. There are two different methods to increase the return on investment of floating offshore wind farms (FOWF's): reduce the cost of the wind farm with minimal loss of power, and increase the power generation through improved design, operation or arrangement of wind turbines within the wind farms.

The capital cost of the floater supporting the turbine represents about 18% of the total capital cost of a complete offshore wind turbine development [3]. Reducing the cost of the spar-type floater is one possible way to reduce the overall cost of a wind turbine development. It is obvious that truncating the platforms can save on the structural cost of floating offshore wind turbines (FOWT's). The resulting shorter floaters are expected to undergo significant pitch and yaw motions, which could result in meaningful gyroscopic coupling associated with the huge rotating blades.

Various alternatives to increase power output from the overall wind farm will be investigated in the proposed thesis. Alternatives will include enhancing the efficiency of the turbine itself, and decreasing the influence of rotor wakes of an upstream turbine that otherwise reduce the efficiency of downstream turbines. An implementation of individual pitch control (IPC) will be investigated to potentially improve generating efficiency, such that the angle of attack remains optimal as each blade progresses through the swept area. The performance of a FOWT in a wind farm is subject to a decreased wind speed and also an increased dynamic loading arising from the increased turbulence induced by upstream turbines. A new semi-empirical wake model of a turbine with an inclined tower will be derived to describe the wake deficit of the far wake based on conservation of momentum and mass. The characteristics of far wakes will be applied to assess power performance of downstream FOWT's at different locations.

1.2 Literature Review

Various floater concepts for offshore wind turbine platforms have been investigated including spar buoys, tension leg platforms, and barges; these design concepts have been based on developments in the offshore oil and gas business. The first FOWT, the Hywind, consists of a spar-type floater supporting a 2-MW generator. The Hywind was installed and tested in the North Sea in 2009 [4]. The OC3-Hywind model is a numerical model based on the original Hywind spar floater, combined with the NREL 5-MW baseline turbine [4]. The OC3-Hywind has become a baseline design case used by many researchers in the offshore wind field.

The possibility of reducing the overall cost by reducing the cost of the floater is not new. Floater costs can be reduced by truncating the platform without introducing a dramatic decrease in electricity generation, as reported by Wang and Sweetman [5]. They develop three truncated platform designs based on the OC3-Hywind concept, with drafts of 97, 89, and 84 m. The floater designs developed in their work are based on volumetric weights from the OC3 design, such that estimates of the steel weights and therefore costs are relatively rough. Fylling and Berthelsen [6] optimize designs of spar-type FOWT support structures to minimize costs of the spar buoy, mooring lines, and cable. Hall et al. [7] improve FOWT support structure designs by optimizing the relationship between cost and nacelle acceleration using genetic algorithms; they conclude that designs with a central cylinder surrounded by three or six outer cylinders have better performance than conventional single-cylinder structure. The complexity of support floaters in each of the above two investigations may introduce additional costs and concept risks that have not been quantified, so these types of floaters are not considered in the current work.

The design of the truncated floaters in this proposed thesis is based on the OC3-Hywind model introduced by Jonkman [4]. The cut-in, rated, and cut-out wind speeds of the NREL 5-MW turbine of this model are 3 m/s, 11.4 m/s, and 25 m/s respectively, the start-up and rated rotor speeds are 6.9 rpm and 12.1 rpm respectively, the run-pitch value is 0 degrees, and the rated generator torque is 43,094 Nm. The eight different blade cross sections of the NREL 5-MW turbine from root to tip are shown in Figure 1.1. Details of the blade sectional information are not available to the public, such as the material of the blades and the internal structural arrangement.

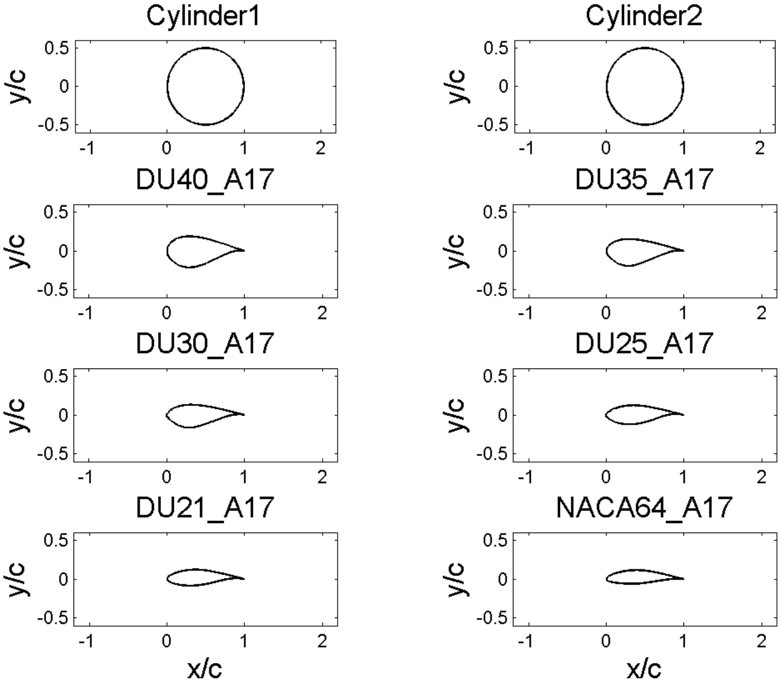

Figure 1.1: Shapes of blade cross sections.

The well-recognized industry-standard software package, FAST [8], is commonly used to simulate the dynamic response of both onshore and offshore wind turbines in the time-domain. The development of FAST includes a small-angle assumption, which limits its application to floaters rotating less than 20 degrees. A computational tool called Loose can realize the simulation of shorter floaters with rotational displacements of unlimited size. Loose is a multi-body solver based on the momentum cloud method (MCM), which is fundamentally based on the conservation of momentum [9]. The equations of motion (EOM's) in Loose are based on the Newton's second law and conservation of momentum derived in terms of pitch-roll-yaw sequenced Euler angles. The dynamic motions of the FOWT are coupled in the time domain independent of any small-angle assumptions. The external forces applied in the EOM's include gravity, restoring forces from hydrostatics and mooring lines, wind forces on the blades, and wave and hydrodynamic damping forces; external moments include restoring moments from hydrostatics and wind moments on the blades. Nonlinear hydrostatic restoring forces and moments in the EOM's are derived with pitch-roll-yaw Euler angle sequence [10], which is compatible with the existing Euler sequence used throughout Loose. This derivation is based on the analytical approach developed by AI-Solihat and Nahon [11] who solve the hydrostatic restoring forces and moments using the roll-pitch-yaw Euler sequence. The aerodynamic loads on the blades are calculated within Loose using the AeroDyn subroutine and the pre-existing DISCON control routine. Simulation results from Loose for the OC3-Hywind model have been verified through critical comparison with FAST [12] for small rotational angles. No comparison between Loose and FAST is possible for large angles of inclination because FAST relies on a small-angle assumption rather than application of sequenced Euler angles.

Wind flow that has passed a turbine can be divided into a near wake, downstream of the rotor and within approximately three rotor diameters, and a far wake that is beyond the near wake. The wake of the blades of a turbine consists of vortex sheets from the trailing edge of each blade, smaller vortices generated at each blade tip, plus a hub vortex generated at the center of the rotor [13]. The characteristics of turbine wakes have been studied theoretically, numerically, and experimentally. Kinematic methods are commonly used to describe a wake velocity deficit and the wake boundary. A simple top-hat shape model for the deficit of wake velocity based on conservation of momentum is proposed and developed by Jensen [14], Katic et al. [15], and Frandsen et al. [16]. Another wake deficit model based on conservation of mass and momentum, plus an assumption that the wake deficit is distributed as a Gaussian distribution is derived by Bastankhah and Porté-Agel [17]. These wake models are commonly used to model the wake for horizontal axis wind turbines with vertical towers. A turbine is described as having yaw angles if the rotational plane is not perpendicular to incoming winds. The shape of the wake expansion of a yawed turbine is found to have an asymmetric kidney shape. This phenomenon is first reported by Howland et al. [18], who study the wake under uniform inflow conditions for yawed turbines. Bastankhah and Porté-Agel [19] explain that the formation of the kidney shape results from a counter-rotating vortex pair (CVP) and can be predicted using conservation of mass. They also derive the wake deflection and the wake trajectory of a yawed wind turbine based on the governing equations of the fluid field. Another analytical wake model is developed based on both analytical and numerical studies to predict the wake trajectory of turbines under the yawed motion by Qian and Ishihara [20]. The wake flow of a FOWT with leaning tower may appear similar to that of turbines with yaw displacement because the rotational plane of the turbine is circular and axisymmetric around the hub axis. Rockel et al. [21] study the influence of the platform pitch on the wake flow using a model wind turbine in a wind tunnel. Later, Rockel et al. [22] study the development of the wake of a FOWT and compare it with the wake of a fixed turbine. These kinematic methods reduce computation expense and are easy to use. Unfortunately, they also have significant shortcomings: the kinematic model proposed for one condition may not be suitable for other cases, the solution of velocity field may not be sufficiently accurate, turbulence may not be accurately considered, and most of these models are appropriate only for modeling the far wake and not the near wake.

Computational fluid dynamic (CFD) methods solving the Navier-Stokes equations are broadly used to model the wake domain. The turbulence model, large eddy simulation (LES), can be used to save computational expense by neglecting the smallest length scales. Xiao and Yang [23] use LES to study the impact of swell-induced pitch motion on wakes. There are open source codes used to perform CFD simulation such as the Open Source Field Operation and Manipulation (OpenFOAM) [24]. OpenFOAM includes a series of numerical solvers for solving different types of CFD problems and both pre-processing and post-processing utilities used to prepare meshes and process results. The transient pisoFoam solver in OpenFOAM is designed to solve incompressible turbulent flow. The “piso” refers to the PISO algorithm (Pressure-Implicit with Splitting of Operators). It reduces computational expense by enabling use of larger time steps. This solver includes the large eddy simulation (LES) turbulence model that is generally applied to compute the flow field of the turbine wakes.

The Simulator for Wind Farm Applications (SOWFA) [25] is used to solve the wake field and inflow turbulence. SOWFA is developed at the National Renewable Energy Laboratory (NREL) with a computational core based on OpenFOAM. The pisoFoamTurbine solver in SOWFA is based on the OpenFOAM pisoFoam solver. This solver applies actuator line models to represent the effect the turbine has on the wind. Both OpenFOAM and SOWFA are commonly used to study the flow field of wind turbines. The large eddy simulator in OpenFOAM is used to study the interactions between the wake flow of turbines and the atmospheric boundary layer [26]. SOWFA is applied to optimize the energy production with yaw control strategy by decreasing the wake effects to the downstream turbines by Gebraad et al. [27]. The main advantage of the CFD method is the ability to compute details of the wake flow fields; the main disadvantage is the complexity required to create wind turbine models and the extremely large computational intensity necessary to model a large wind domain.

The fatigue loads acting on the downstream turbines are also important. The impacts of atmospheric and wake turbulence on the fatigue loading on two onshore NREL 5-MW turbines are studied by Lee et al. [28]. They study the damage-equivalent loads (DELs) to estimate the fatigue life of turbines. They conclude that the surface roughness and wake from upstream turbines increase the fatigue load, while the instability condition of the atmosphere has only minor influence. Both short-term and lifetime DELs can be calculated using a code, developed by NREL called MLife [29]. The loading on the turbine blades used to analyze the fatigue life of blades can be computed using BeamDyn. BeamDyn is a time-domain structural-dynamics module for slender structures developed by NREL [30]. An alternate non-linear beam model based on conservation of momentum has been developed by Tang and Sweetman [31], which can be applied to model turbine blades to calculate loads on different blade sections.

1.3 Mathematical Background

The mathematical background related to this study is introduced including the environmental conditions for the numerical simulation, the commonly used theoretical wake models, large eddy simulation method used for wake flow field study, and fatigue analysis method for turbine blades.

1.3.1 Environmental Conditions

1.3.1.1 Wave Conditions

FOWT's are subject to irregular winds and waves. Random waves can be described by a power spectrum. The one-dimensional Pierson-Moskowitz spectrum is developed for fully developed waves in the North Atlantic Ocean, assuming deep water, unlimited fetch, and no swell [32]:

$$S(f) = \alpha_p g^2 (2\pi)^{-4} f^{-5} exp[-\frac{5}{4}(\frac{f}{f_p})^4] \tag{1.1}$$

in which f is the wave frequency, α_p is the energy scale equal to 0.0081, f_p is the peak frequency and depends only on the wind speed, $f_p U_{19.5}/g = 0.14$, in which $U_{19.5}$ is the wind speed at height equal to 19.5 m above the sea surface.

The JONSWAP spectrum is a modification of the Pierson-Moskowitz spectrum for developing waves with the limited fetch in the North Sea [33]:

$$S(f) = \alpha g^2 (2\pi)^{-4} f^{-5} exp[-\frac{5}{4}(\frac{f}{f_{peak}})^{-4}] \gamma^{exp[-\frac{1}{2}(\frac{f/f_{peak}-1}{\sigma})^2]} \tag{1.2}$$

in which α is the energy scale parameter, f_{peak} is the frequency scale parameter, γ is the shape parameter equal to 3.3, σ is the shape parameter equal to 0.07 if $f \leq f_p$ and equal to 0.09 if $f > f_p$.

The Pierson-Moskowitz spectrum has no effect from fetch comparing with the JONSWAP spectrum. The two spectra are substantially identical for relatively benign wave conditions such as those applied as operational conditions for floating wind turbines. The Pierson-Moskowitz spectrum is chosen as the wave environmental condition for the assessment of power performance of FOWT's.

Swells are waves generated by distant weather systems and not by local winds. They are generally smoother and have longer periods than wind waves. Swells are not considered in the simulation since this study is not for a specific location and only wind waves and associated winds are considered.

1.3.1.2 Wind Conditions

Wind turbines are all sited within the atmospheric boundary layer (ABL), which is about 1 km thick in contact with the sea surface. The ABL is neutral if only the mechanical interaction between the sea surface and the air is considered. Monin-Obukhov theory is commonly used to describe the wind profile for the neutral atmospheric surface layer and the logarithmic form of the vertical distribution of horizontal mean wind speeds is expressed as [34]:

$$u(z) = \frac{u_*}{\kappa}[ln(\frac{z}{z_0}) - \Psi(\frac{z}{L})] \tag{1.3}$$

in which u is the wind speed at height z, u_* is the friction velocity, κ is the von Karman's constant, z_0 is the roughness length, L is the Monin-Obukhov length, and Ψ is a stability correction function. The wind speed is characterized by Ψ, u_*, and z_0. Ψ equals 0 for a neutral stability condition and the mean wind speed can be rearranged as [35]:

$$u(z) = u(z_{ref})\frac{ln(\frac{z}{z_0})}{ln(\frac{z_{ref}}{z_0})} \tag{1.4}$$

A constant value, 0.0002 m, is typically taken as the roughness length of sea surface, which is in accordance with the European Wind Atlas [36].

The turbulent velocity fluctuations are described by a wind spectrum. The Kaimal spectral model specified by the International Electrotechnical Commission (IEC) for the normal turbulence is used in this study, which is designed for neutral stability condition [35]:

$$S_k(f) = \frac{4\sigma_k^2 L_k/V_{hub}}{(1 + 6fL_k/V_{hub})^{\frac{5}{3}}} \tag{1.5}$$

in which the subscript k indicates the three velocity component directions, f is the frequency, σ_k is the standard deviation of the velocity component, L_k is the integral scale parameter of the velocity component, and V_{hub} is the mean wind speed at the hub height.

1.3.2 Theoretical Wake Deficit Models

Theoretical wake models can be used to describe the distribution of wake velocity at downstream locations. There are several theoretical wake models used to describe downstream wake velocities, including: the top-hat model ([14, 15]), which is based on the conservation of momentum, Gaussian shape model [17], which is based on the conservation of momentum and mass, and the turbulent jet model, which is based on Abramovich's theory of turbulent jets [37]. These models include variable parameters that can be adjusted to conform the wake profile to model test and numerical simulation results. The conservation of momentum equation is expressed as shown in Equation 1.6. This form neglects the acceleration, pressure, gravity, and viscosity and yields a simple expression for the thrust [17]:

$$T = \int_A \rho U_w (U_0 - U_w) dA \tag{1.6}$$

in which T is the total force acting on the control volume used for conservation of momentum, ρ is the density of air, U_w is the wake velocity, U_0 is the free stream velocity, and A is the wake cross-sectional area. The thrust force T can also be expressed as:

$$T = \frac{1}{2} C_T \rho A_0 U_0^2 \tag{1.7}$$

in which C_T is the thrust coefficient and A_0 is the area of the rotor plane.

The top-hat model is a wake velocity deficit model that is simple and is commonly used. It assumes that the wake expands linearly as $d_w = d_0 + 2kx$ and the wake velocity is a constant value for the wake at any downstream distance x [15]:

$$U_w = U_0 \left[1 - \frac{1 - \sqrt{1 - C_T}}{(1 + 2kx/d_0)^2} \right] \tag{1.8}$$

in which k is the wake expansion factor and d_0 is the turbine diameter.

The wake velocity deficit has been observed to be distributed approximately as a Gaussian shape in the far wake in numerous wind-tunnel experiments and numerical simulations ([38, 39]). Bastankhah and Porté-Agel [17] propose a Gaussian-shaped wake model based on conservation of mass and momentum. Their velocity deficit model is expressed as:

$$\begin{aligned}\frac{\triangle U}{U_0} = &\left[1-\sqrt{1-\frac{C_T}{8(k^*x/d_0+0.2\sqrt{\beta})^2}}\right]* \\ &exp\left\{-\frac{1}{2(k^*x/d_0+0.2\sqrt{\beta})^2}\left[(\frac{z-z_h}{d_0})^2+(\frac{y}{d_0})^2\right]\right\}\end{aligned} \tag{1.9}$$

in which $\triangle U$ is the velocity deficit, k^* is the wake growth rate, y and z are the spanwise and vertical positions, z_h is the hub height, and β is equal to $0.5 * (1+\sqrt{1-C_T})/\sqrt{1-C_T}$. This model has been shown to be superior to simple top-hat models through comparison with model test results, wind tunnel measurements, and numerical simulation results. The wake flow is in the downstream direction in these wake models. The wake flow of a yawed turbine is shifted to the left or right depending on turbine yaw. The wake center shift angle and the wake velocity deficit of turbines with yaw angle θ are derived based on conservation of momentum and mass [40]:

$$\alpha \approx \frac{cos^2\theta sin\theta\frac{C_T}{2}}{(1+\frac{2kx}{d_0})^2} \tag{1.10}$$

$$\triangle U \approx U_0\frac{cos^3\theta\frac{C_T}{2}}{(1+\frac{2kx}{d_0})^2} \tag{1.11}$$

1.3.3 Large Eddy Simulation Method

The large eddy CFD simulation model (LES) is broadly used for turbulence modeling because it is much more efficient at solving the Navier-Stokes equations; the increased efficiency results from neglecting the smallest length scales. The divergence-free form of the Navier-Stokes equation represents conservation of momentum and conservation of mass for incompressible flow. It has been expressed as [41]:

$$\mathbf{u}_t + \nabla \cdot (\mathbf{u}\mathbf{u}^T) - \frac{1}{Re} \triangle u + \nabla p = \mathbf{f} \tag{1.12}$$

$$\nabla \cdot \mathbf{u} = 0 \tag{1.13}$$

in which **u** is the 3-dimensional velocity vector, t is the time, p is the pressure, Re is the Reynolds number, and **f** is the body force acting on the field.

The space-filtered governing equations for the LES model can be expressed as [41]:

$$\overline{\mathbf{u}}_t + \nabla \cdot (\overline{\mathbf{u}\mathbf{u}^T}) - \frac{1}{Re} \triangle \overline{u} + \nabla \overline{p} = \overline{\mathbf{f}} \tag{1.14}$$

$$\nabla \cdot \overline{\mathbf{u}} = 0 \tag{1.15}$$

The nonlinear filtered advection term $\overline{\mathbf{u}\mathbf{u}^T}$ can be solved by defining the subgrid-scale stress tensor:

$$\tau(\mathbf{u}, \mathbf{u}) = \overline{\mathbf{u}\mathbf{u}^T} - \overline{\mathbf{u}}\overline{\mathbf{u}}^T \tag{1.16}$$

One of the most common sub-grid scale eddy viscosity models is the Smagorinsky model [42]:

$$\nu_T = ((C_S\delta)^2)|\nabla^s \mathbf{w}| \tag{1.17}$$

in which ν_T is the turbulent viscosity coefficient, $\mathbf{w} \cong \overline{\mathbf{u}}$, C_S is a constant value, and δ is the filter width.

The mesh size of the numerical LES model is an important factor that influences the convergence of solutions of the partial differential equations. The mesh grids must satisfy the Courant-Friedrichs-Lewy (CFL) condition [43]:

$$C = \frac{u\Delta t}{\Delta x} + \frac{v\Delta t}{\Delta y} + \frac{w\Delta t}{\Delta z} \leq C_{max} \tag{1.18}$$

in which C is the Courant number, u, v, and w are magnitudes of the velocity components in three directions, Δt is the time step, Δx, Δy, and Δz are the grid lengths in three directions, C_{max} is typically taken as 1.

1.3.4 Fatigue Analysis

Fatigue is an important design consideration for wind turbines. Wind turbine blades are subject to nonproportional cyclic multiaxial loading including aerodynamic loading, gravitational loading, and inertial loading, which lead to multiaxial states of stress and strain, and thus the multiaxial fatigue analysis instead of the uniaxial fatigue analysis is necessary for fatigue life prediction of turbine blades. Multiaxial stresses or strains are generally reduced to an equivalent uniaxial stress or strain for fatigue analysis. The stress-life and strain-life methods are two commonly used methods to predict the fatigue life. Multiaxial fatigue analysis theories based on the strain-life method are discussed below.

The three methods of the static yield criteria are the octahedral shear strain theory (von Mises strain theory), the maximum principal strain theory, and the maximum shear strain theory [44]:

$$\begin{aligned}\triangle\epsilon_{eq} =& \frac{1}{\sqrt{2}(1+\nu)} * \\ &\sqrt{(\triangle\epsilon_x - \triangle\epsilon_y)^2 + (\triangle\epsilon_y - \triangle\epsilon_z)^2 + (\triangle\epsilon_x - \triangle\epsilon_z)^2 + \frac{3}{2}(\triangle\gamma_{xy}^2 + \triangle\gamma_{yz}^2 + \triangle\gamma_{xz}^2)}\end{aligned} \tag{1.19}$$

$$\triangle\ \epsilon_{eq} = \triangle\epsilon_1 \tag{1.20}$$

$$\frac{\triangle\gamma_{eq}}{2} = \frac{\triangle\epsilon_1 - \triangle\epsilon_3}{2} \tag{1.21}$$

in which $\triangle\epsilon_{eq}$ is the equivalent strain range, $\triangle\epsilon_x$, $\triangle\epsilon_y$, $\triangle\epsilon_z$, $\triangle\gamma_{xy}$, $\triangle\gamma_{yz}$, and $\triangle\gamma_{xz}$ are ranges of the six strain components, $\triangle\epsilon_1$ and $\triangle\epsilon_3$ are ranges of the principal strains.

The above strain-based multiaxial fatigue theories are not suitable for all materials and loading conditions. A suitable method for computing the equivalent strain should be chosen based on the material property and the strain state. The three stress-based methods of the static yield criteria are similar to the three strain-based methods.

The Whöler relation [45] as shown in Equation 1.22 characterizes the material performance under high-cycle fatigue loading. This relation can be expressed as the stress-cycle (S-N) curve.

$$N_f \triangle S^m = K \tag{1.22}$$

in which $\triangle S$ is the magnitude of constant stress, m is the Whöler's coefficient, and K is a variable relate to material damage at failure.

This S-N curve describes the fatigue damage of one load condition. Elements of wind turbine blades are subject to complex loading conditions, which can be reduced to simple stress or strain reversals. The cycles of varying stress or strain reversals for analyzing fatigue data are commonly counted with rainflow-counting algorithm [46]. Miner's rule can be used to accumulate all damages acting at one location [47]:

$$D = \sum \frac{n_i}{N_i} \leq D_{cr} \tag{1.23}$$

in which n_i is the number of cycles of the stress σ_i, N_i is the number of cycles to failure, and D_{cr} is the total damage.

1.4 Unique Contribution

The unique contributions of this research include: 1) development of structural designs to demonstrate that truncating the floater hull reduces cost with only minor impact on electricity harvest; 2) development of a simple individual pitch control method to investigate the possibility of mitigating the reduction in power generation associated with turbine lean; 3) derivation of a semi-empirical wake model to describe the wake profile and the wake expansion shape of a yawed or tilted wind turbine; 4) optimization of the power generation of FOWT's with truncated platforms; 5) assessment of multiaxial fatigue analysis of blades of FOWT's operating on compliant floating platforms; 6) assessment of performance of power generation of downstream turbines at different locations.

1.5 Organization of Dissertation

This dissertation focuses on performance optimization of FOWT's including design of supporting structures, wake effects impacting on the downstream turbines, and prediction of fatigue life of turbine blades.

Development of new floaters is presented in Chapter 2. A family of seven spar-type floaters based on the OC3-Hywind model is designed in conformance with the industrial structural rule. The nonlinear hydrostatic loads of floaters with large rotational motions are derived based on the pitch-roll-yaw Euler angles and applied to Loose. Dynamic responses of FOWT's with the newly designed floaters are then assessed. The optimal floater is determined through the tradeoff between structural cost and power generation. A FOWT with this optimal floater is used as a reference model for further study. A new individual pitch control method in order to improve power generation is also developed based on optimization of attack angle of each turbine blade.

A new semi-empirical wake model based on the Joukowski transformation is developed for a yawed or tilted wind turbine in Chapter 3. The derivation is based on conservation of mass and momentum. A series of numerical simulation cases with different free stream wind speeds and tilt angles is computed using CFD method. Both the wake shape and wake velocity distribution of the new wake model are calibrated with numerical results. The new wake model is finally applied to assess power generation and to predict fatigue lives of turbine blades.

Multiaxial fatigue analysis of turbine blades of three FOWT's operating on newly designed floaters is assessed in Chapter 4. Turbine models are chosen from Chapter 2 and fatigue analysis of these models with truncated floaters is computed and compared to study the effect from stiffness of floaters on the fatigue life of turbine blades based on the strain-life method. Strains at any location along a turbine blade are derived based on the MBBT method. The maximum principal strain method is applied for the multiaxial fatigue analysis and the normal strain method is used for the simple uniaxial fatigue analysis. Fatigue results of the two methods are compared and discussed.

Power generation of downstream turbines at different locations is computed and compared in Chapter 5. Resonant responses of downstream FOWT's excited by wakes from upstream turbines are then studied.

Summary, conclusions, and future work are presented in Chapter 6.

2. DESIGN OPTIMIZATION OF HULL SIZE FOR SPAR-BASED FLOATING OFFSHORE WIND TURBINES *[1]

2.1 Introduction

Wind is an increasingly important source of renewable energy that is presently undergoing a period of rapid expansion worldwide. New technologies continue to be developed for offshore floating wind as new wind farms are sited in increasingly deep waters. Various floater concepts for offshore wind turbine platforms have been investigated including spar buoys, tension leg platforms, and barges, with these design concepts based on developments in the offshore oil and gas business. The first floating offshore wind turbine (FOWT), the Hywind, consists of a spar-type floater supporting a 2-MW generator. Hywind was installed and tested in the North Sea in 2009 [4]. The world's first full-scale floating wind farm was installed and began to deliver electricity to the northeast coast of Scotland in 2017 [2], and is also a spar-type floater. Many spar-based floating wind turbine designs are based on the OC3-Hywind. This numerical model was introduced by Jonkman [4]; it is based on the Hywind spar floater combined with the NREL 5-MW baseline turbine. The OC3-Hywind has become a baseline design case used by many researchers in the offshore wind field.

The capital cost of the floater supporting the turbine represents about 18% of the total capital cost of a complete offshore wind turbine development [3]. The work presented here investigates the possibility of reducing overall costs by reducing the cost of the floater, in this case the spar structure. It has been shown [5] that floater costs can be reduced by truncating the platform, without introducing a dramatic decrease in electricity generation. Three truncated platform designs were developed based on the OC3-Hywind concept, with drafts of 97, 89, and 84 m. The floater designs developed in that work were based on volumetric weights from the OC3 design, such that the steel

---

[1] Reprinted with permission from Springer [10].

weights and therefore costs were relatively rough estimates. Capital cost of the structure is significant but does not completely dominate project economics; other costs of an offshore wind turbine development include costs of turbine, grid connection, management, operation and maintenance, and decommissioning. Fylling and Berthelsen [6] optimize designs of spar-type FOWT support structures to minimize costs of the spar buoy, mooring lines, and cable. The work presented here is to optimize the ratio between cost and electricity generation, rather than to exclusively focus on cost. Hall et al. [7] optimize FOWT support structure designs to optimize the relationship between cost and nacelle acceleration using genetic algorithms; they conclude that designs with a central cylinder surrounded by three or six outer cylinders have better performance than conventional single-cylinder structure. The work presented here is focused exclusively on spar-type buoyant structures and does not investigate other structure concepts.

Here, numerical models of seven new floaters are presented and critically compared in terms of steel weight and electrical generation potential. The structural weight of each of these competing designs is based on a preliminary structure designed in conformance with a recognized design standard: Bulletin 2U on Stability Design of Cylindrical Shells from the American Petroleum Institute (API) [48]. Development of these designs requires more than simply following the structural code: this new class of floaters allows significant pitch and yaw angles, which can result in meaningful gyroscopic coupling caused by the huge rotating blade. The dynamic coupling has been simulated in the time-domain using a computational tool called Loose. Loose is a multi-body solver based on the momentum cloud method (MCM), which is fundamentally based on the conservation of momentum [9]. Loose directly applies Newton's second law to set up equations of motion (EOM's) in terms of pitch-roll-yaw sequenced Euler angles, which are solved in the time domain independent of any small-angle assumptions. The simulation results of Loose for the OC3-Hywind model have been verified through critical comparison with the well-recognized industry-standard FAST software package [12] for small rotational angles. No comparison between Loose and FAST is possible for large angles of inclination because FAST relies on a small-angle assumption rather than application of sequenced Euler angles. The transformation matrices developed and applied in

FAST become sufficiently non-orthogonal that the code cannot converge.

Some of the newly-proposed floater designs have low hydrostatic restoring stiffness, resulting in large angles between the tower and a vertical axis such that the wind is not perpendicular to the rotor disk. This paper briefly investigates the potential to improve generating efficiency by individually controlling the pitch angle of each blade, such that the angle of attack remains optimal as each blade progresses through the swept area. A very simple and idealized individual pitch control (IPC) method is employed to assess the potential for improved generating efficiency if all other considerations are neglected. Computed generating efficiency using idealized IPC is critically compared with efficiency computed for traditional collective pitch control (CPC) to assess the potential for efficiency improvements. Prior work on IPC (e.g., [49] and [50]) has not been focused on efficiency improvements: that work was to apply separate PID controllers for each blade to reduce fatigue loading on the blades. Both the IPC and CPC control systems applied in this work are based on the pre-existing DISCON control routine [4], which has been coupled with the Loose software [12]. A variable-speed generator-torque controller in DISCON varies the generator torque to maximize output power when the wind speed is lower than the rated wind speed. A proportional integral blade pitch controller in DISCON varies the pitch angle of each blade to maintain constant rated generator torque when the wind speed is above the rated wind speed. The instantaneous blade pitch angles found by the controller are passed to AeroDyn to calculate the wind loads on the blades. The cut-in, rated, and cut-out wind speeds of this turbine are 3 m/s, 11.4 m/s, and 25 m/s respectively, the start-up and rated rotor speeds are 6.9 rpm and 12.1 rpm respectively, the run-pitch value is 0 degrees, and the rated generator torque is 43,094 Nm [4] for both CPC and IPC.

The development of the seven new floater designs is presented in Section 2.2; a precise analytical method used to compute hydrostatic restoring forces and moments based on sequenced Euler angles without application of small-angle assumptions is developed and presented in Section 2.3; an individual pitch control method is presented in Section 2.4; details of the simulation methodology and computation of environmental loading are presented in Section 2.5, and results are analyzed and critically compared in Section 2.6. Overall results indicate the proposed new class of floater designs is both technically feasible and appears to be economically superior to existing floaters.

2.2 Seven New Floater Designs Conforming to API Practice

A family of seven new spar-buoy platforms with drafts ranging from 62 to 120 m have been preliminarily designed based on the concept of the OC3-Hywind model provided by Jonkman [4]. All seven designs are in conformance with the industry-standard structural guide, API Bulletin 2U [48]. The designs have been explicitly checked for local shell buckling, general instability, column buckling of the ring stiffened cylindrical shell, and material yielding. Figure 2.1 shows a comparative view of the seven new floaters. The components of each of the wind turbines above the supporting platform are the same as OC3-Hywind, including the tower, nacelle, and rotor. The top of the OC3-Hywind platform is 10 m above the still water level (SWL). The diameter of the platform from the top to 4 m below the SWL is 6.5 m. The platform from 4 m below the SWL to 12 m below the SWL is tapered with the diameter increasing linearly from 6.5 to 9.4 m. The cylindrical shell from 12 m below the SWL to the bottom of the platform is 108 m. The only modification to the external shape of the existing OC3 Hywind concept for each of the designs presented here is shortening the lower cylindrical shell. Internal structure is designed in accordance with API practice for each of the competing designs. The ballast weight for the 120 m platform is set to maintain the same total weight as Hywind such that the draft of the free-floating platform remains constant. This design work was necessary because the original specification of the OC3 Hywind did not include structural details. Specific parameters including draft (D), hull mass (M_h), total mass of the floater (M_t), roll inertia about mass center of the floater (I_x), pitch inertia about mass center of the floater (I_y), yaw inertia about platform centerline (I_z), mass center of the floater below SWL (C_m), displacement volume (V_d), metacentric height of the turbine model (GM), and natural frequency of platform pitch (f) are summarized in Table 2.1; sizes of T-section ring-stiffeners are provided in Table 2.2. The metacentric height GM is evaluated with Equation 2.1 as below:

$$GM = KB + BM - KG \tag{2.1}$$

in which KB and KG are the center of buoyancy and the center of gravity above the bottom of the floater, respectively; BM is the distance between the center of buoyancy and the metacenter, which equals $\frac{I_{xx}}{V_d}$, in which I_{xx} is the second moment of the water plane area.

Table 2.1: Parameters of seven new floaters. Reprinted with permission from Springer [10].

Floater No.	1st	2nd	3rd	4th	5th	6th	7th
D $[m]$	120	97	89	79	74	67	62
M_h $[kg]$	1.22E+6	9.85E+5	9.06E+5	8.02E+5	7.52E+5	6.80E+5	6.29E+5
M_t $[kg]$	7.47E+6	5.83E+6	5.26E+6	4.55E+6	4.19E+6	3.70E+6	3.34E+6
I_x $[kg \cdot m^2]$	4.31E+9	2.31E+9	1.81E+9	1.28E+9	1.06E+9	8.03E+8	6.48E+8
I_y $[kg \cdot m^2]$	4.31E+9	2.31E+9	1.81E+9	1.28E+9	1.06E+9	8.03E+8	6.48E+8
I_z $[kg \cdot m^2]$	9.29E+7	7.27E+7	6.56E+7	5.68E+7	5.24E+7	4.63E+7	4.19E+7
C_m $[m]$	-100.30	-81.16	-74.46	-66.12	-61.93	-56.07	-51.86
V_d $[m^3]$	8029	6433	5878	5184	4837	4351	4004
GM $[m]$	25.99	17.04	13.71	9.40	7.10	3.77	1.18
f $[Hz]$	0.049	0.042	0.038	0.032	0.028	0.020	0.010

Table 2.2: Parameters of T-section rings of floaters. Reprinted with permission from Springer [10].

web height of rings $[m]$	0.04
web thickness of rings $[m]$	0.02
flange width of rings $[m]$	0.25
flange thickness of rings $[m]$	0.025
ring spacing $[m]$	1.20
shell thickness $[m]$	0.033

Each of the seven floaters also has been designed to have adequate hydrostatic stability and benign dynamic performance. Time-domain nonlinear dynamic simulations of system performance have been performed on each design subject to the nacelle rated wind speed and an associated wave condition which conforms a fully-arisen Pierson-Moskowitz sea state. The maximum nacelle acceleration in the direction along the spin axis observed in any of the simulation results is 4 m/s^2, which was observed for the 120 m platform. Nacelle acceleration generally decreases with decreasing floater length because floater stiffness in the pitch direction decreases. The average hull pitch displacement shown in Figure 2.2 ranges from 3.5 degrees for the 120 m model to 33 degrees for the 62 m model. Dynamic simulations are performed using the Loose simulation software, which does not rely on the small-angle assumptions implicit to several industry-standard wind turbine simulators (e.g., FAST). The pre-existing version of Loose computed hydrostatic restoring moments using the relative motion of the centers of buoyancy and gravity, but did not consider nonlinear changes to the shape of the water-plane area [9]. Complete nonlinear hydrostatic restoring forces and moments are developed as part of this work and included as modifications to Loose to correctly account for large-angle hydrostatics.

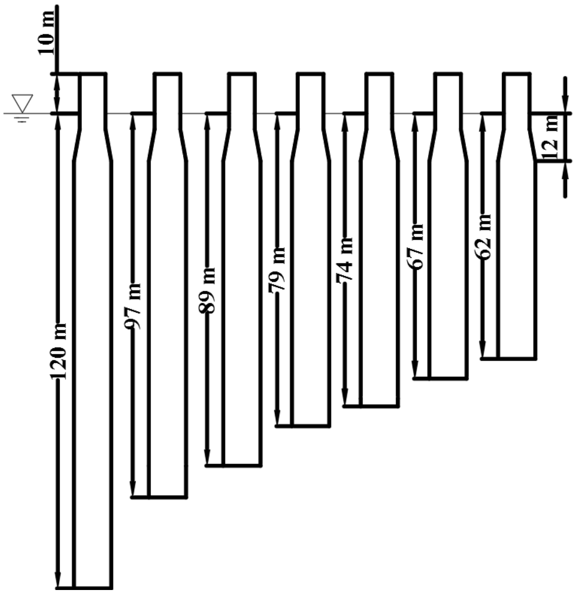

Figure 2.1: General view of seven new floaters. Reprinted with permission from Springer [10].

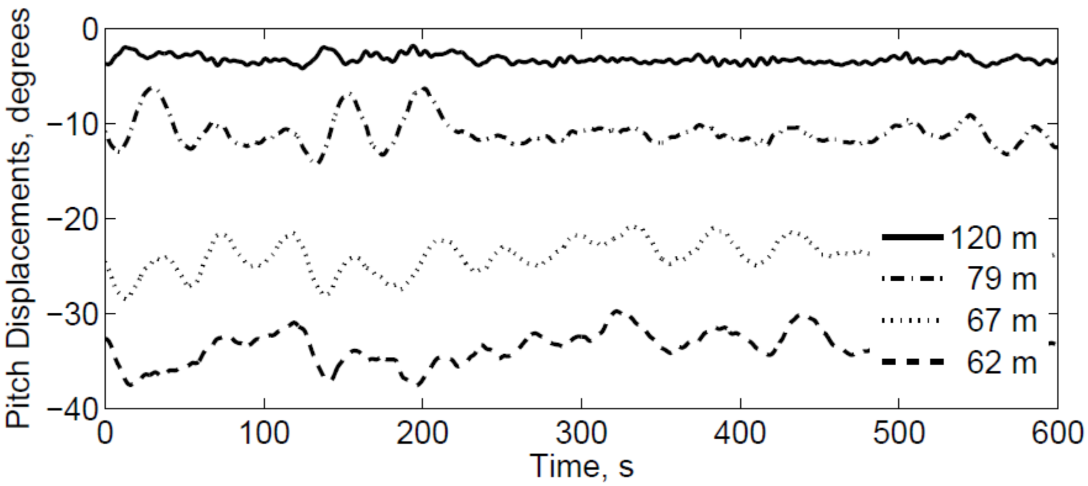

Figure 2.2: Comparison of hull pitch displacements at rated wind speed. Reprinted with permission from Springer [10].

2.3 Nonlinear Hydrostatics

Nonlinear hydrostatic restoring forces and moments are derived for cylindrical hull shapes subject to large angles of inclination. The derivation is for the pitch-roll-yaw Euler angle sequence, which is compatible with the existing 1-2-3 Euler sequence used throughout the Loose software. The derivation is based on that of AI-Solihat and Nahon [11] for restoring forces and moments using the yaw-pitch-roll Euler sequence. Following the logic of AI-Solihat and Nahon, but applied to the pitch-roll-yaw Euler sequence, two coordinate systems (CS's) are used: a body-fixed system (x_s, y_s, z_s), with origin at the instantaneous center of mass of the complete floating system, and an earth-fixed inertial system (X, Y, Z) that coincides with the body-fixed system when the floater is at its equilibrium position (Figure 2.3). The translational and rotational displacements of the floating cylinder are expressed as matrix X:

$$\boldsymbol{X} = [X_1 \quad X_2 \quad X_3 \quad X_4 \quad X_5 \quad X_6]^T \tag{2.2}$$

where X_1, X_2, and X_3 are the three components of $\boldsymbol{r}$ in Figure 2.3 representing surge, sway, and heave motions, and X_4, X_5, X_6 indicate rotations in the pitch, roll, and yaw directions. Equa-

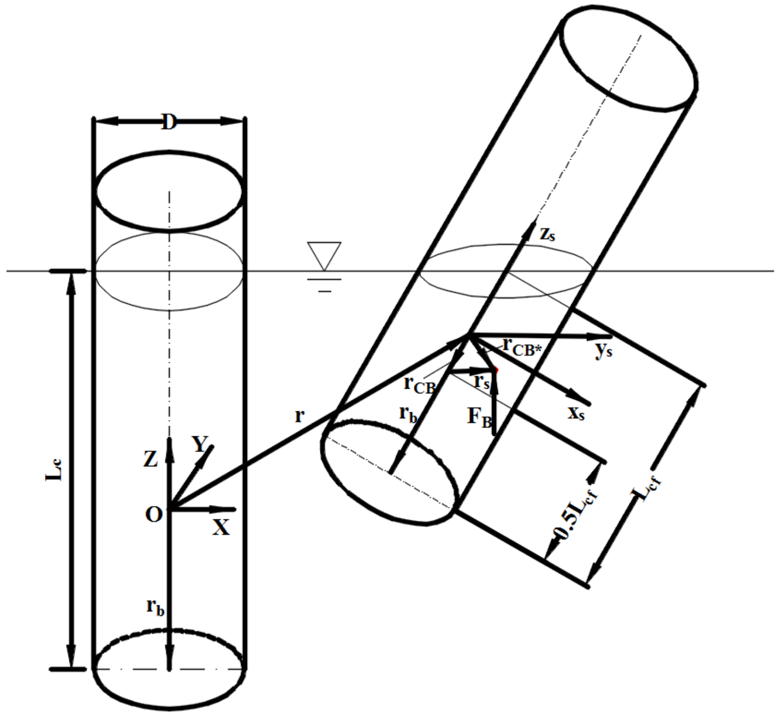

Figure 2.3: Inertial and body-fixed coordinate systems in Loose. Reprinted with permission from Springer [10].

tion 2.3 gives the transformation matrix between the (x_s, y_s, z_s) and (X, Y, Z) systems conforming to the 1-2-3 Euler angle sequence [9].

$$\begin{aligned} T_{s\to I} &= T_x(X_4)T_y(X_5)T_z(X_6) \\ &= \begin{bmatrix} cX_5cX_6 & -cX_5sX_6 & sX_5 \\ cX_4sX_6 + sX_4sX_5cX_6 & cX_4cX_6 - sX_4sX_5sX_6 & -sX_4cX_5 \\ sX_4sX_6 - cX_4sX_5cX_6 & sX_4cX_6 + cX_4sX_5sX_6 & cX_4cX_5 \end{bmatrix} \end{aligned} \tag{2.3}$$

where cX_i and sX_i indicate $\cos X_i$ and $\sin X_i$ respectively. Transformation matrices $T_x(X_4)$, $T_y(X_5)$, and $T_z(X_6)$ are the principal rotation matrices:

$$T_x(X_4) = \begin{bmatrix} 1 & 0 & 0 \\ 0 & cX_4 & -sX_4 \\ 0 & sX_4 & cX_4 \end{bmatrix} T_y(X_5) = \begin{bmatrix} cX_5 & 0 & sX_5 \\ 0 & 1 & 0 \\ -sX_5 & 0 & cX_5 \end{bmatrix} T_z(X_6) = \begin{bmatrix} cX_6 & -sX_6 & 0 \\ sX_6 & cX_6 & 0 \\ 0 & 0 & 1 \end{bmatrix} \tag{2.4}$$

Buoyancy acts along the positive Z-axis with magnitude equal to the weight density of water times the submerged volume:

$$F_B = \rho g A L_{cf} \tag{2.5}$$

where ρ is the density of sea water; g is the gravitational acceleration; A is the cross-sectional area of the floater; L_{cf} is the submerged length (Figure 2.3).

$$L_{cf} = \frac{L_c - (T_{s\to I} r_b - r_b)_Z - X_3}{cos\psi} \tag{2.6}$$

in which L_c is the submerged length of the cylinder in its equilibrium position; r_b is the distance from the origin of the body-fixed CS to the base center of the cylinder; the subscript Z denotes the Z component; X_3 is the Z component of the displacement of the body-fixed CS; ψ is the angle between z-axis and Z-axis so that $cos\psi = T_{33}$, where T_{33} is the element of $T_{s\to I}$ in the third row and third column.

The resulting hydrostatic restoring moment is resolved into the inertial CS (Figure 2.3):

$$\boldsymbol{M}_B^I = \boldsymbol{T}_{s\to I}\boldsymbol{r}_{CB*} \times \boldsymbol{F}_B = \boldsymbol{T}_{s\to I}\boldsymbol{r}_{CB} \times \boldsymbol{F}_B + \boldsymbol{T}_{s\to I}\boldsymbol{r}_s \times \boldsymbol{F}_B = \boldsymbol{M}_{ZB}^I + \boldsymbol{M}_{wp}^I \tag{2.7}$$

where the superscript I indicates the parameter is resolved in the inertial CS. The components of $\boldsymbol{M}_{ZB}^I$ represent the coupling effects between heave, roll, and pitch:

$$\boldsymbol{M}_{ZB}^I = [Y_F F_B \quad - X_F F_B \quad 0]^T \tag{2.8}$$

where X_F and Y_F are the X and Y components of the vector from the center of the body-fixed CS to the midpoint of the submerged length, L_{cf}. The expression for the restoring moment resulting from the water plane area in the inertial CS is [11] :

$$\boldsymbol{M}_{wp}^{I} = [M_{wp}^{X} \quad M_{wp}^{Y} \quad M_{wp}^{Z}]^T = \boldsymbol{T}_{s\to I}\rho g I[-T_{32} - \frac{T_{32}^3 + T_{32}T_{31}^2}{2T_{33}^2} \quad T_{31} + \frac{T_{31}^3 + T_{31}T_{32}^2}{2T_{33}^2} \quad 0]^T \tag{2.9}$$

where M_{wp}^{X} and M_{wp}^{Y} represent the coupling effects between roll and pitch displacements of the cylinder. The hydrostatic restoring forces and moments are represented as matrix, M:

$$\boldsymbol{M} = [0 \quad 0 \quad F_B \quad M_B^X \quad M_B^Y \quad M_B^Z]^T = [0 \quad 0 \quad F_B \quad Y_F F_B + M_{wp}^X \quad -X_F F_B + M_{wp}^Y \quad 0]^T \tag{2.10}$$

Derivation of each non-zero term in the stiffness matrix is shown in Appendix A. The complete stiffness matrix expressed in the inertial coordinate system is:

$$\boldsymbol{K} = -\frac{\partial \boldsymbol{M}}{\partial \boldsymbol{X}} = \begin{bmatrix} 0 & 0 & 0 & 0 & 0 & 0 \\ 0 & 0 & 0 & 0 & 0 & 0 \\ 0 & 0 & K_{33} & K_{34} & K_{35} & K_{36} \\ 0 & 0 & K_{43} & K_{44} & K_{45} & K_{46} \\ 0 & 0 & K_{53} & K_{54} & K_{55} & K_{56} \\ 0 & 0 & 0 & 0 & 0 & 0 \end{bmatrix} \tag{2.11}$$

in which each non-zero $K_{i,j}$ can be expressed as:

$$
\begin{aligned}
K_{33} &= \frac{\rho g A_c}{cX_4 cX_5} \\
K_{34} &= -\rho g A_c \frac{\partial L_{cf}}{\partial X_4} \\
K_{35} &= -\rho g A_c \frac{\partial L_{cf}}{\partial X_5} \\
K_{36} &= -\rho g A_c \frac{\partial L_{cf}}{\partial X_6} \\
K_{43} &= -F_B \frac{\partial Y_F}{\partial X_3} + Y_F K_{33} \\
K_{44} &= -cX_5 cX_6 \frac{\partial M_{wp}^x}{\partial X_4} + cX_5 sX_6 \frac{\partial M_{wp}^y}{\partial X_4} - sX_5 \frac{\partial M_{wp}^z}{\partial X_4} - F_B \frac{\partial Y_F}{\partial X_4} - Y_F \rho g A_c \frac{\partial L_{cf}}{\partial X_4}
\end{aligned}
$$

$$
\begin{aligned}
K_{45} &= sX_5cX_6M_{wp}^x - cX_5cX_6\frac{\partial M_{wp}^x}{\partial X_5} - sX_5sX_6M_{wp}^y + cX_5sX_6\frac{\partial M_{wp}^y}{\partial X_5} - cX_5M_{wp}^z \\
&\quad -sX_5\frac{\partial M_{wp}^z}{\partial X_5} - F_B\frac{\partial Y_F}{\partial X_5} - Y_F\rho gA_c\frac{\partial L_{cf}}{\partial X_5} \\
K_{46} &= cX_5sX_6M_{wp}^x - cX_5cX_6\frac{\partial M_{wp}^x}{\partial X_6} + cX_5cX_6M_{wp}^y + cX_5sX_6\frac{\partial M_{wp}^y}{\partial X_6} - sX_5\frac{\partial M_{wp}^z}{\partial X_6} \\
&\quad -F_B\frac{\partial Y_F}{\partial X_6} - Y_F\rho gA_c\frac{\partial L_{cf}}{\partial X_6} \\
K_{53} &= F_B\frac{\partial X_F}{\partial X_3} + X_F\rho gA_c\frac{\partial L_{cf}}{\partial X_3} \\
K_{54} &= (sX_4sX_6 - cX_4sX_5cX_6)M_{wp}^x - (cX_4sX_6 + sX_4sX_5cX_6)\frac{\partial M_{wp}^x}{\partial X_4} \\
&\quad +(sX_4cX_6 + cX_4sX_5sX_6)M_{wp}^y - (cX_4cX_6 - sX_4sX_5sX_6)\frac{\partial M_{wp}^y}{\partial X_4} \\
&\quad +cX_4cX_5M_{wp}^z + sX_4cX_5\frac{\partial M_{wp}^z}{\partial X_4} + F_B\frac{\partial X_F}{\partial X_4} + X_F\rho gA_c\frac{\partial L_{cf}}{\partial X_4} \\
K_{55} &= -sX_4cX_5cX_6M_{wp}^x - (cX_4sX_6 + sX_4sX_5cX_6)\frac{\partial M_{wp}^x}{\partial X_5} + sX_4cX_5sX_6M_{wp}^y \\
&\quad -(cX_4cX_6 - sX_4sX_5sX_6)\frac{\partial M_{wp}^y}{\partial X_5} - sX_4sX_5M_{wp}^z + sX_4cX_5\frac{\partial M_{wp}^z}{\partial X_5} + F_B\frac{\partial X_F}{\partial X_5} \\
&\quad +X_F\rho gA_c\frac{\partial L_{cf}}{\partial X_5} \\
K_{56} &= (-cX_4cX_6 + sX_4sX_5sX_6)M_{wp}^x - (cX_4sX_6 + sX_4sX_5cX_6)\frac{\partial M_{wp}^x}{\partial X_6} \\
&\quad +(cX_4sX_6 + sX_4sX_5cX_6)M_{wp}^y - (cX_4cX_6 - sX_4sX_5sX_6)\frac{\partial M_{wp}^y}{\partial X_6} \\
&\quad +sX_4cX_5\frac{\partial M_{wp}^z}{\partial X_6} + F_B\frac{\partial X_F}{\partial X_6} + X_F\rho gA_c\frac{\partial L_{cf}}{\partial X_6}
\end{aligned}
$$

2.4 Individual Pitch Control

A simple idealized concept for individual pitch control is investigated to determine the potential for increasing generating efficiency. The idea is to subtract out geometric changes to the angle of attack caused by the rotational motion of tower, such that each blade maintains the ideal angle of attack relative to its apparent wind. The existing AeroDyn subroutine is used to compute an ideal angle of attack for a wind turbine on a vertical support structure. The difference between this ideal angle and the instantaneous angle of attack is computed for a single representative blade segment located at a constant radius r from the hub. The entire blade is rotated in pitch relative the hub to optimize the angle for that segment. The location r is selected for optimization because the segment at that location generates the highest average spin moment at the hub, as computed over numerous simulations at a variety of wind speeds. Computed sectional inflow velocities are then applied at each blade segment to calculate the induction factor and the lift and drag coefficients. Figure 2.4 shows the blade geometry and angle of attack and Figure 2.5 shows the side view and the front view of a wind turbine with the tower inclined.

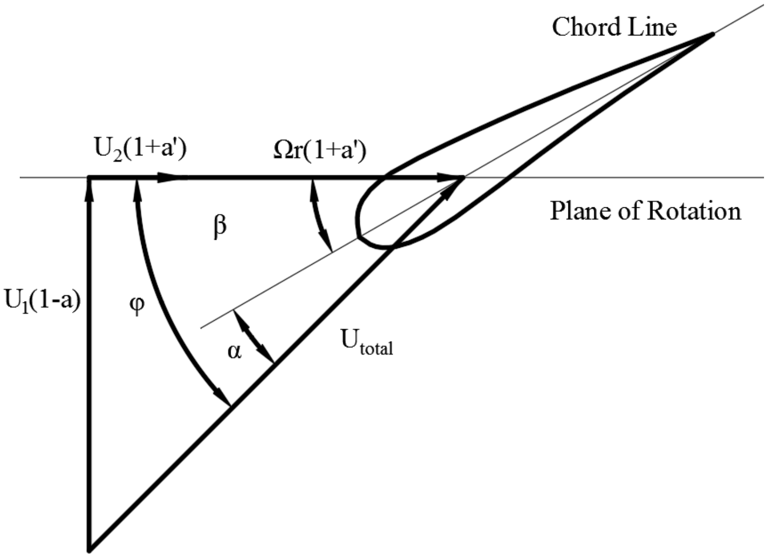

Figure 2.4: Blade geometry for analysis of a horizontal axis wind turbine. Reprinted with permission from Springer [10].

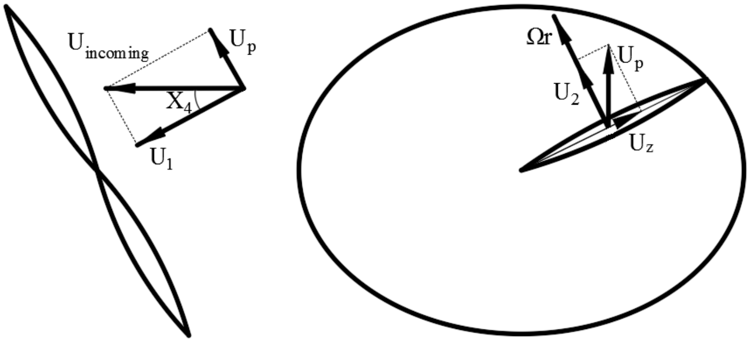

Figure 2.5: Incoming wind acting on wind turbine. Reprinted with permission from Springer [10].

A vector decomposition of the velocity at the blade element is shown in Figure 2.4. Vector U_1 is the normal wind speed, which is perpendicular to the plane of rotation; vector $U_1(1-a)$ is the total normal velocity including the effect of the normal wake, where a is the axial induction factor. The tangential component in the plane of rotation of the total velocity at the blade element is $\Omega r + U_2$, where Ω is the angular velocity of the blade element, r is the distance from the blade element to the hub center, and U_2 is the wind velocity component resolving into a coordinate system coincident with the direction of the tangential velocity component Ωr. The total tangential velocity including the wake effect is $(\Omega r + U_2) * (1 + a')$, where a' is the tangential induction factor. The angle of the apparent wind relative to the blade, ϕ in Figure 2.4, can be calculated after computing the normal and tangential velocity components U_1 and U_2. It can be represented as the sum of two parts: the angle of attack α that varies continuously with U_2 as it changes as the blade rotates about the hub, plus the section pitch angle β which is constant for any one time step. The effect $\triangle\alpha$ from U_2 on the angle of attack α can be obtained from Equation 2.12. A new angle of attack is computed for each time step in Loose by computing a new ideal angle for a vertical turbine in DISCON and then updating that blade pitch angle computed by $\triangle\alpha$. The result is that the updated angle of attack for the single representative blade element rotating about the spin axis remains close to the ideal value computed by AeroDyn for a wind turbine with a nearly rigid supporting structure that does not lean in response to the wind loading. All translational and rotational motions are fully considered in AeroDyn and Loose in the calculation of the relative wind at every time-step; the induction factors

a and a' are recomputed in Aerodyn for each time-step, and the updating angle $\triangle\alpha$ is directly computed for each time-step as:

$$\triangle\,\alpha = \alpha - \alpha' = \phi - \phi' = \arctan\frac{U_1(1-a)}{(\Omega r + U_2)(1+a')} - \arctan\frac{U_1(1-a)}{\Omega r(1+a')} \tag{2.12}$$

The concept underlying the decomposition can be most clearly explained for a simple case considering only the pitch angle of the tower and only horizontal incoming wind velocities. The incoming wind velocity $U_{incoming}$ in Figure 2.5 can be decomposed into two components: U_1 perpendicular to the plane of rotation, and U_p parallel to the plane of rotation. Component U_p is further decomposed into two parts: U_2 in the same direction as the tangential velocity component Ωr in Figure 2.4, and U_z along the blade's pitch axis. The component of the incident wind U_2 is zero for any blade position if the tower is vertical such that the plane of rotation is perpendicular to the SWL. Component U_2 is non-zero for a leaning tower and is maximum when the tower is leaning away from the wind, the rotor is turning clockwise looking down wind, and the blade tip is pointing to the right and traveling downward in Figure 2.5; component U_2 is at a minimum when the blade tip is pointing to the left and traveling upward, and is zero when the blade is vertical.

2.5 Simulation Methodology

2.5.1 Momentum Cloud Method

A time-domain numerical simulation methodology called the MCM is used to perform the dynamic simulations of the FOWT's with truncated floaters. This method must be used in place of industry-standard software because the angular motions of these novel designs exceed conventional small-angle assumptions. The method includes modeling each major component of the FOWT as a rigid body: the tower (including the supporting platform), the nacelle, the hub, and each of the three blades. Each of these bodies has six degrees of freedom. Three EOM's for translational motion of the coupled system are developed using Newton's second law, and three EOM's for rotational motion of the system are developed using conservation of angular momentum.

All of the EOM's are set up about mass center of the whole system, such that translational and rotational EOM's are decoupled [9]:

$$\sum \vec{F} = m\vec{a}_{G_s} \tag{2.13}$$

$$\sum \vec{M} = (\dot{\vec{H}}^s_{G_s})_{C_s} + \vec{\omega}_s \times \vec{H}^s_{G_s} \tag{2.14}$$

in which $\sum \vec{F}$ includes all external forces applied to the wind turbine system: gravity, restoring forces from hydrostatics and mooring lines, wind forces on the blades, and wave forces; m is the total mass of the system; $\vec{a}_{G_s}$ is the acceleration vector of the system at the mass center including three components of three directions (surge, sway, and heave); $\sum \vec{M}$ includes all external moments: restoring moments from hydrostatics and mooring lines, wind moments on the blades, and hydrodynamic moments; $\vec{H}^s_{G_s}$ is the angular momentum of the entire system in the system-fixed CS; $\vec{\omega}_s$ is the angular velocity vector with respect to the global CS. The method used to calculate hydrostatic restoring forces and moments has been presented in detail in Section 3. The large-angle wind simulator Loose has been extensively benchmarked against the industry-standard FAST software and found to be in general agreement. A systematic comparison of displacements and computed output power between the Loose and Fast simulations is provided by Sweetman and Wilder [12].

2.5.2 Restoring Loads from Mooring Lines

A simplified mooring system is assumed to consist of four radial taut lines for convenience. The change in tension in each line can easily be expressed as a function or cable stretch. Each fairlead position is calculated by summing translations and Euler angle rotations. The contribution of each mooring line is calculated consecutively and then summed. The combined restoring force in the (X, Y, Z) system and the combined restoring moment calculated about the origin G_s of the (x_s, y_s, z_s) system in this body-fixed system are needed in the application of equations of motion of the system.

Compliance along each straight line is due to elasticity of the materials only. The radius position of any one fairlead (point A) in the inertial coordinate system (X, Y, Z) is $\vec{\rho}_{A/O} =$

$\vec{\rho}_{G_s/O} + T_{s\to I}\vec{\rho}_{A/G_s}$, where the radius vector $\vec{\rho}_{G_s/O}$ is the position of G_s measured from the (X, Y, Z) system, $\vec{\rho}_{G_s/O} = (X_1, X_2, X_3)$ and $\vec{\rho}_{A/G_s}$ is the radius position of point A in the (x_s, y_s, z_s) system. The position of the fixed end (point E) of this mooring line on the sea bottom, $\vec{\rho}_{E/O}$, is constant in the (X, Y, Z) system. Combining the radius position from point A to point E in the (X, Y, Z) system is $\vec{\rho}_{E/A} = \vec{\rho}_{E/O} - \vec{\rho}_{A/O}$. The tension along a neutrally buoyant taut line in the (X, Y, Z) system can be obtained by the nature of elasticity material [51]:

$$\vec{F}^I_{line} \quad = \quad [T_0 + \frac{ES}{L}(\rho_{E/A} - L)]\frac{\vec{\rho}_{E/A}}{\rho_{E/A}} \tag{2.15}$$

where T_0 is the pretension of one mooring line; E is Young's Modulus; S is the cross sectional area of the line; L is the initial length of the line; $\rho_{E/A}$ is the norm of the vector $\vec{\rho}_{E/A}$, i.e. the instantaneous length of the line. The restoring force of the mooring system, $\vec{F}^I_{mooring}$, is obtained by summing the force from each line.

The restoring moment from each line in the (x_s, y_s, z_s) system is obtained by decomposing the restoring force into the (x_s, y_s, z_s) system first and then multiplied by the radius vector of the fairlead, i.e. $\vec{F}^s_{line} = T_{I\to s}\vec{F}^I_{line}$ and $\vec{M}^s_{line} = \vec{\rho}_{A/G_s} \times \vec{F}^s_{line}$. The result from each line can be further summed to obtain the restoring moment from mooring system, $\vec{M}^s_{mooring}$.

2.5.3 Wind Loads

The aerodynamic lift, drag, and pitching moments of a series of airfoil sections along each wind turbine blade are calculated in AeroDyn for the full-field wind and then passed to Loose. AeroDyn applies two wake model theories, the blade element momentum (BEM) theory and the generalized dynamic wake (GDW) theory (e.g., [52]). BEM theory is used when the wind speed below 8 m/s and GDW theory is used when the wind speed above 8 m/s.

2.5.4 Wave Loads

The well-known Morison equation is used throughout this work to compute the hydrodynamic loads on the spar structure. The hydrodynamic loads are computed for finite slices along the length of the cylinder and summed over the length of the hull:

$$\vec{f_n} = C_m \rho \frac{\pi}{4} D^2 \dot{\vec{V}}_n - C_a \rho \frac{\pi}{4} D^2 \dot{\vec{V}}_t + \frac{1}{2} C_d \rho D \vec{V}_{rt} |\vec{V}_{rt}| \tag{2.16}$$

in which $\vec{f_n}$ is the wave force per unit length normal to the axis of the cylindrical hull; C_m, C_a, and C_d are the inertia coefficient, added mass coefficient, and drag coefficient, respectively; ρ is the mass density of sea water; D is the hull diameter; $\dot{\vec{V}}_n$ is the wave acceleration in the direction normal to the hull at each hull section; $\dot{\vec{V}}_t$ is the structural acceleration of the section in the same direction as $\dot{\vec{V}}_n$; $\vec{V}_{rt}$ is the normal velocity of water particles relative to the hull section. The stretching effect of sea surface movement is not considered in the calculation of wave velocity and acceleration.

The Morison equation is generally applicable to cylinders having a ratio of cylindrical diameter to wave length less than 0.2 (e.g., [53]). Morison coefficients of C_m = 2.0, C_a = 1.0, and C_d = 0.6 are chosen to be consistent with a previous study of the OC3-Hywind spar [4]. These coefficients are reasonable for application to this approximate scale of structure [53].

2.6 Performance of the Seven New Designs

Each of the seven new designs is evaluated by computing the electrical generation in each of nine simulated environmental conditions. Results are plotted to identify trends in the relationship between floater length and generation performance. Each design is subject to each of the nine simulated environments shown in Table 2.3. Each wind speed is associated with a wave condition conforming a fully-arisen Pierson-Moskowitz sea state [54]:

$$T_P = \frac{7.14 u_{19.5}}{g} \quad H_s = \frac{0.21 u_{19.5}^2}{g} \tag{2.17}$$

in which T_P is the peak period; g is the acceleration due to gravity; $u_{19.5}$ is the wind speed at 19.5 m above the sea surface, which can be computed using a power law, and H_s is the significant wave height. Current and swell are not considered in the simulation.

Wind speeds vary from 5 to 21 m/s, each of which refers to the mean of the full-field wind. Wind and waves are assumed to be in the same direction. Wind speeds above 21 m/s are not investigated because turbines would normally be shut down and parked in these conditions, and because the numerical simulator performs poorly in extreme wind conditions. The CPC is used when the wind speed is greater than the rated wind speed for all the simulations. The International Electrotechnical Commission (IEC) design standard [55] recommends a 10-min simulation length for fixed-bottom offshore wind turbine. Haid et al. [56] demonstrates that a 10 minute simulation is adequate to capture time-domain behavior of FOWT, and recommends disregarding the first 60 seconds to eliminate start-up transients. In this study, each simulation was performed for 1,000 seconds to verify longer-term behavior, with the first 400 seconds disregarded to eliminate a potential longer-period transients in the vessel motions.

Table 2.3: Significant wave heights and peak periods relevant to hub-height wind speeds. Reprinted with permission from Springer [10].

V_{hub} [m/s]	T_p [s]	$H_{1/3}$ [m]
5.0	2.88	0.33
7.0	4.03	0.66
9.0	5.18	1.08
11.4	6.56	1.74
13.0	7.48	2.26
15.0	8.63	3.01
17.0	9.79	3.87
19.0	10.94	4.84
21.0	12.10	5.91

Figure 2.6 and Figure 2.7 show the averaged electric power generated versus the floater draft and versus mean floater pitch displacement for a variety of wind speeds. Individual data points represent floater designs from longest in the left to shortest in the right. A significant decrease in electrical generation in moderate wind speeds is found for drafts shorter than 80 meters; total electrical output is found to be near constant for drafts increasing from 90 to 120 m for every wind speed. The very short floaters show little decrease in electrical generation at high wind speeds (15 to 21 m/s) because there is so much wind that generation efficiency is unimportant; the CPC is

able to adjust the blade angles to maintain the output power at the generator rating value regardless of tower angle. These floaters also show good electricity harvest at very low wind speeds (5 m/s) because there is not enough wind to meaningfully lean even the shortest spars. Regardless of spar draft, there is very little change to the power generation if the angle of tower pitch remains less than about 10 degrees. Most of the power decrease is believed to be due to the angle between the wind and the spin axis, such that the 10 degree limit probably applies to other floater types, such as tension leg platforms, semi-submersibles or barges.

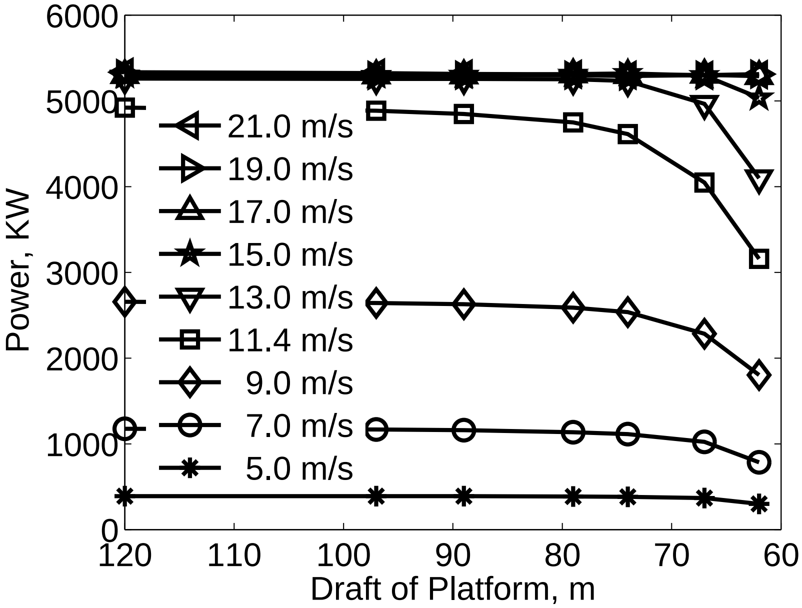

Figure 2.6: Floater draft VS power. Reprinted with permission from Springer [10].

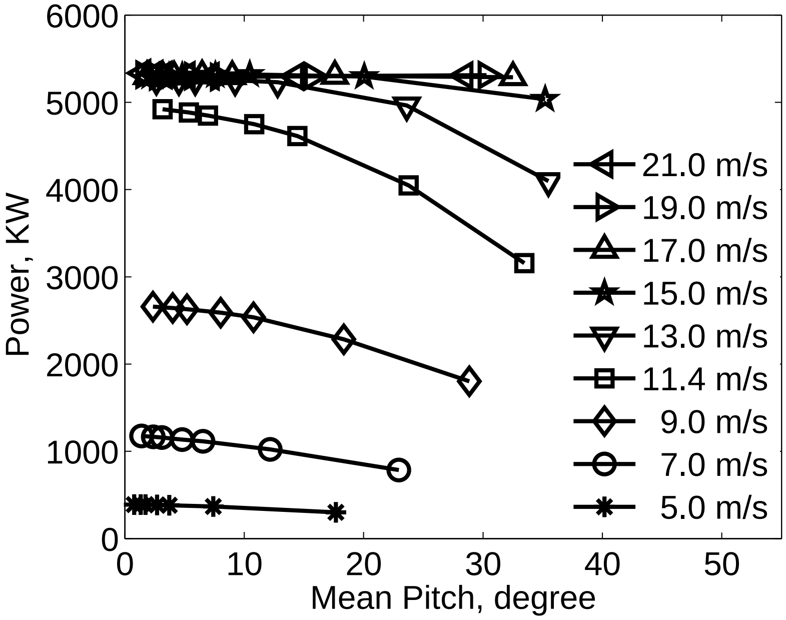

Figure 2.7: Pitch displacements of platforms VS power. Reprinted with permission from Springer [10].

Figure 2.2, Figure 2.8, Figure 2.9, and Figure 2.10 show brief time-histories of system performance at the rated wind speed of 11.4 m/s. Three FOWT's with different floater drafts, 120 m, 67 m, and 62 m, are selected to show the effect of floater length. Shorter floaters are observed to have increased tower pitch and decreased rotor speed and output power. Pitch control remains inactive (zero pitch angle) for the 67 and 62 m floaters for most of the time because the component of the wind speed normal to the plane of the rotor disk is below the 11.4 m/s threshold for active blade pitch control. The simulated irregular wind speed varies above and below the rated wind speed. Figure 2.9 shows the effect of the controller shifting between blade pitch control vs generator torque control.

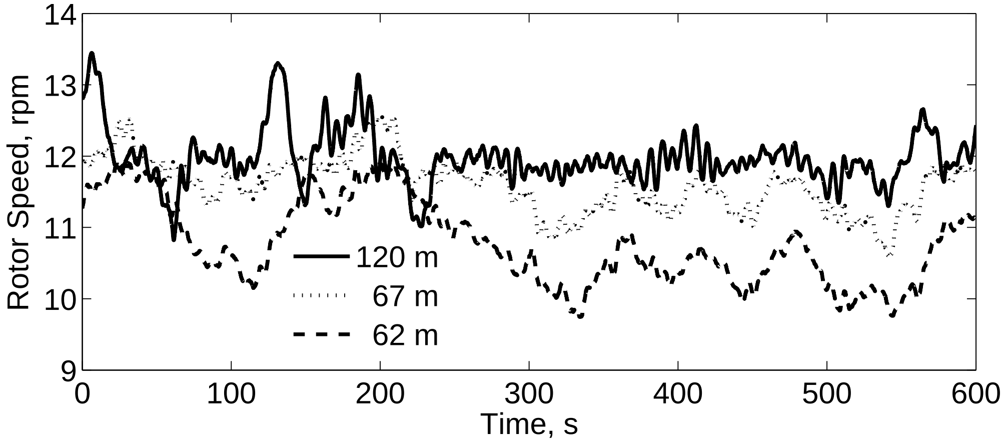

Figure 2.8: Comparison of rotor speed at rated wind speed. Reprinted with permission from Springer [10].

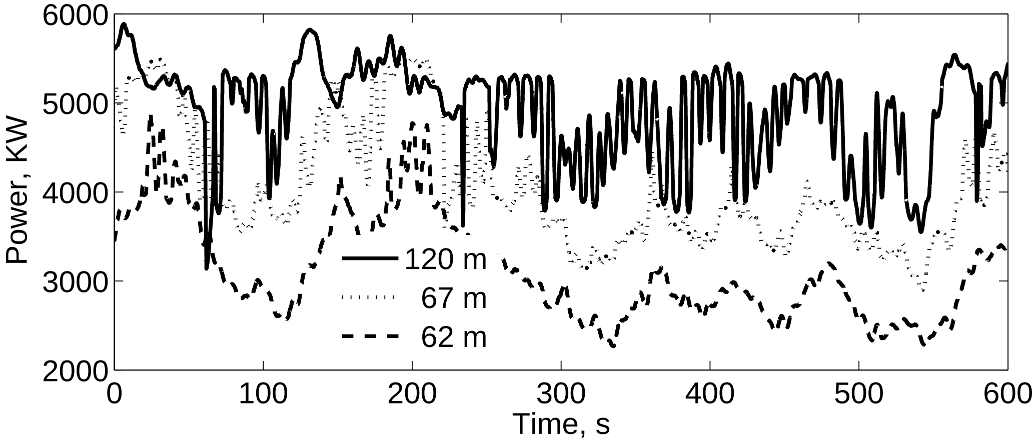

Figure 2.9: Comparison of output power at rated wind speed. Reprinted with permission from Springer [10].

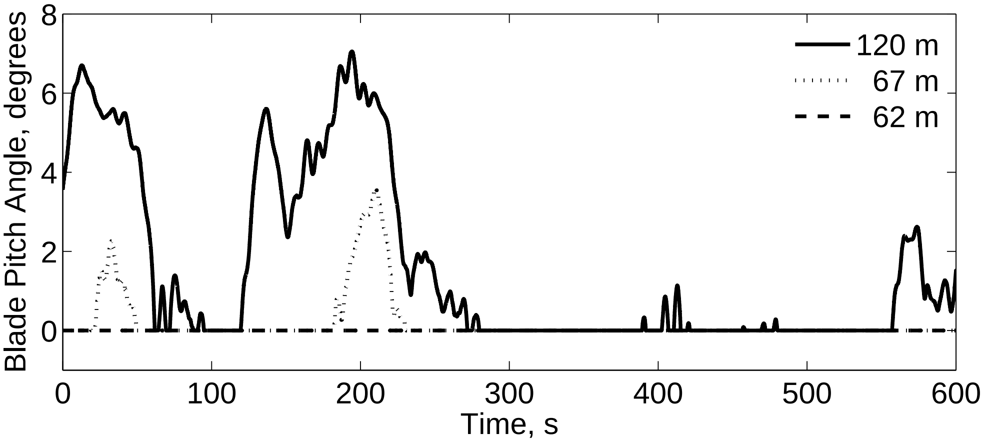

Figure 2.10: Comparison of blade pitch angle at rated wind speed. Reprinted with permission from Springer [10].

Relative cost is important to the evaluation of the new designs. The total cost of each floating wind turbine system is represented as an equivalent tonnage of steel structure. The “weight-cost”, W_t, is defined as the weight of steel costing the same as the complete wind turbine system, and equal to the sum of the actual weight of the hull structural steel, W_h, plus an equivalent weight of steel costing the same as all non-structural components, W_{ob}, so $W_t = W_h + W_{ob}$. The FOWT with the 120 m long floater is chosen as the base case. The cost of its support structure is assumed to be 18$\%$ of the total cost of this FOWT, conforming with data presented by Tegen et al. [3]. The costs of all other components are held constant for the alternate six new designs, so the only change of the total cost is the change in hull cost. The calculation of the weight-cost of all other components is:

$$W_{ob} = \frac{82\%}{18\%} * W_{hb} \tag{2.18}$$

in which W_{hb} is the weight-cost of the hull structure of the base case. The ratio, R, between the total weight-cost and the output power, P, is a measure of relative efficiency between competing designs.

$$R = \frac{W_t}{P} = \frac{W_h + W_{ob}}{P} \tag{2.19}$$

The ratio of weight-cost to power output, R, for seven platforms at nine wind speeds are summarized in Figure 2.11. The electricity generation and floater cost both decrease with reduced cylinder length, and both of these reductions are non-linear. The minimum of each curve indicates the optimum design for that condition. A draft of about 74 m has the best trade-off between cost and electricity harvest in Figure 2.11 a). The ratio decreases when the wind speed increases for the same draft since more electricity is generated when the wind speed increases and the generator-torque controller works to attain maximum power. Figure 2.11 b) indicates the best draft to be about 79 m for the rated wind speed. The ratio is almost same for wind turbines with same draft when the mean wind component perpendicular to the rotor plane is higher than the rated wind speed.

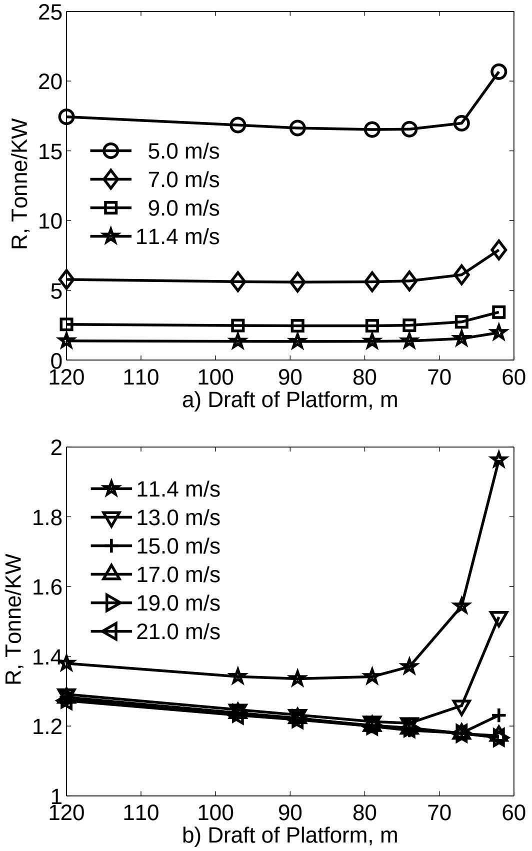

Figure 2.11: Total weight-cost per unit power output for nine wind speeds. Reprinted with permission from Springer [10].

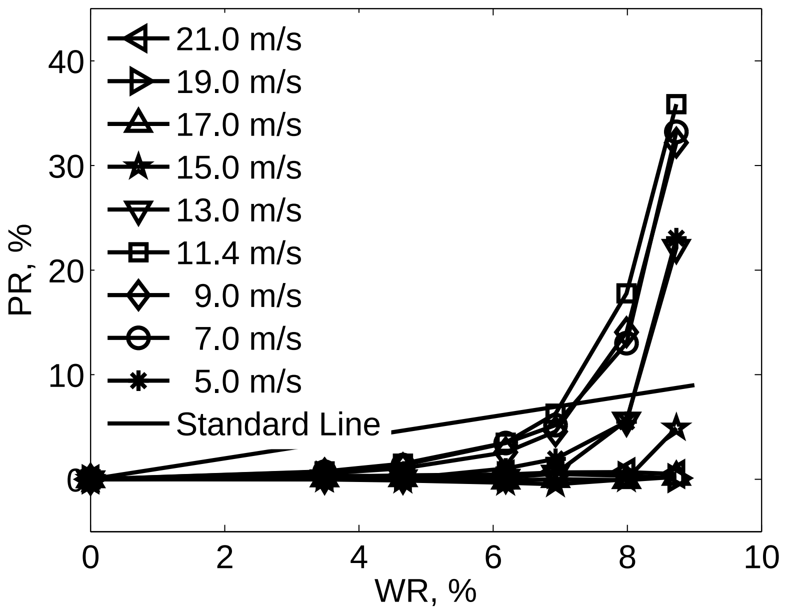

Figure 2.12: Percentage reduction in weight-cost (WR) VS percentage reduction in electricity harvest (PR). Reprinted with permission from Springer [10].

Figure 2.12 offers an alternative presentation of the trade-off between minimal structural weight and maximum power generation. It presents the percentage reduction in weight-cost, WR, vs the percentage reduction in electricity harvest, PR. The quantity WR can be computed by dividing the decrease of hull structural weight by the total weight-cost of the base case, $WR = (W_{hb} - W_h)/(W_{hb} + W_{ob})$. The reduction in electrical harvest, PR, equals the reduction of electricity harvest divided by the total power, $PR = (P_b - P)/P$. The Standard Line indicates the cost savings equal the decreased power generation, i.e., the total cost is reduced by 10% and the electricity harvest is also reduced by 10%. Design cases below and to the right of this line are more cost-effective than the base case. The new models with drafts of 97 m, 89 m, 79 m, and 74 m correspond to weight-cost savings of 3.5%, 4.7%, 6.2%, and 6.9%, and show better design efficiency than the base case at every wind speed.

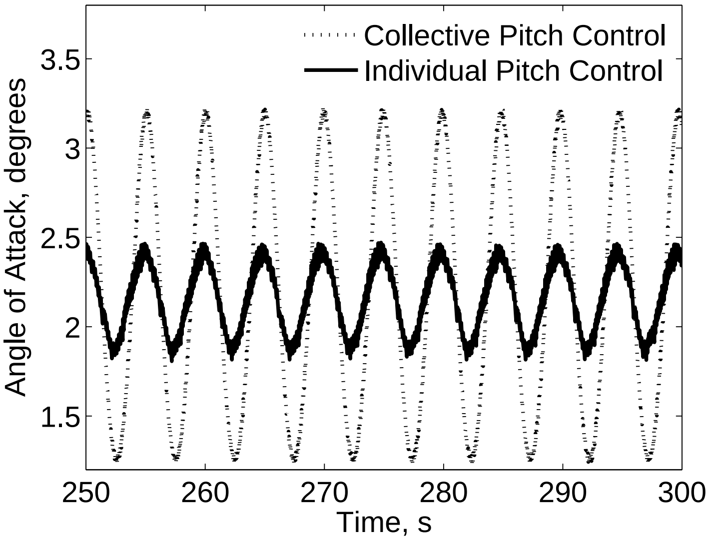

Figure 2.13: Attack angle comparison between CPC and IPC for model with 74 m draft at 13 m/s constant wind speed with constant platform pitch angle. Reprinted with permission from Springer [10].

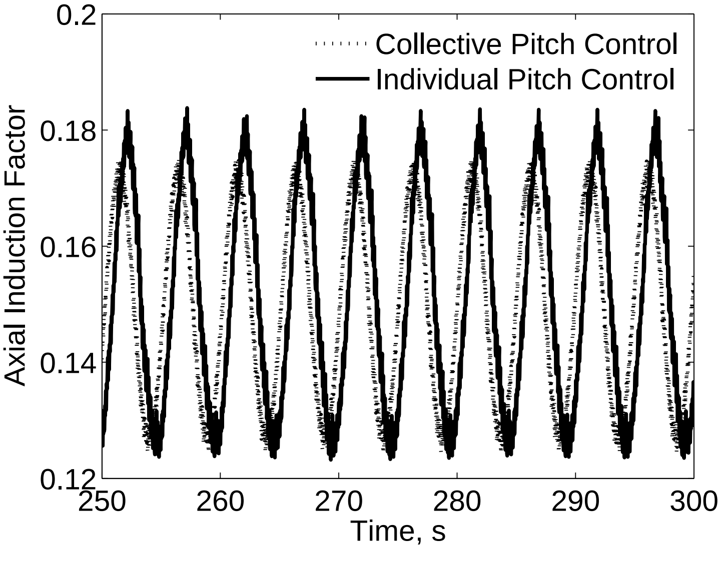

Figure 2.14: Axial induction factor comparison between CPC and IPC for model with 74 m draft at 13 m/s constant wind speed with constant platform pitch angle. Reprinted with permission from Springer [10].

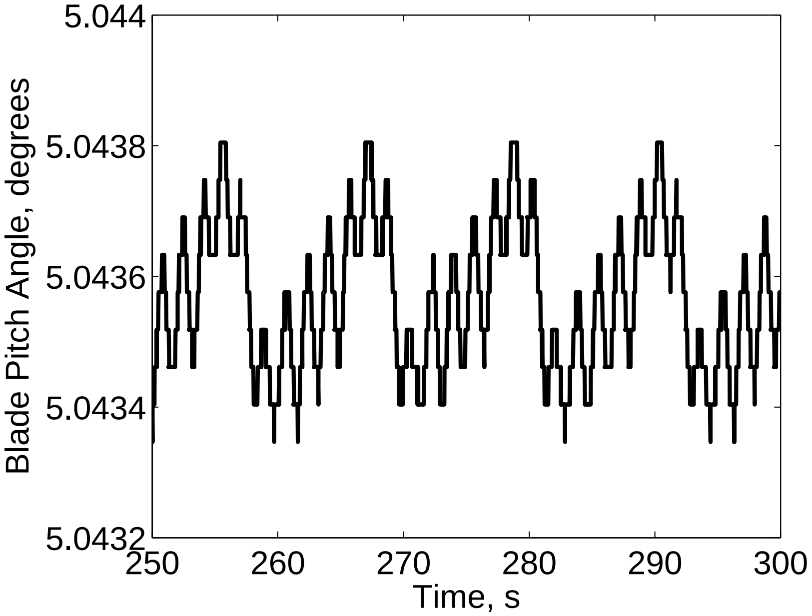

Figure 2.15: Blade Pitch Angle of CPC for model with 74 m draft at 13 m/s constant wind speed with constant platform pitch angle. Reprinted with permission from Springer [10].

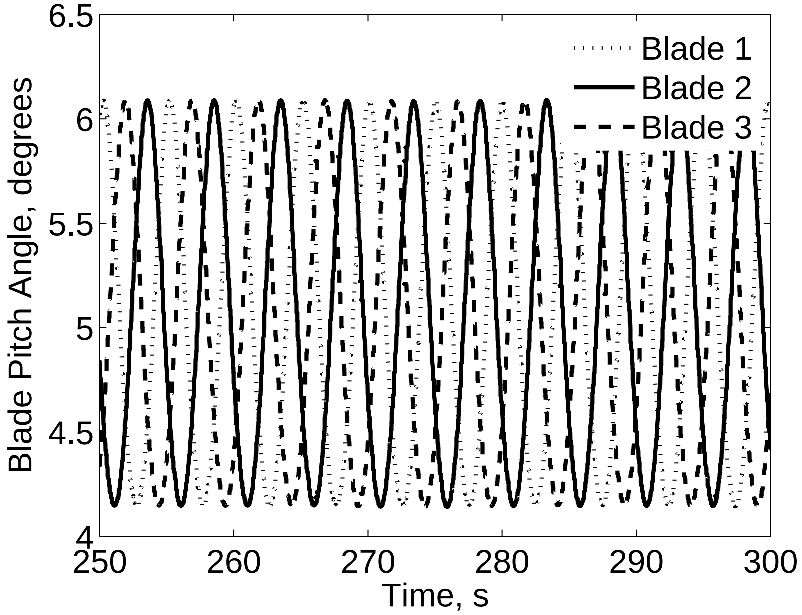

Figure 2.16: Blade Pitch Angle of IPC for model with 74 m draft at 13 m/s constant wind speed with constant platform pitch angle. Reprinted with permission from Springer [10].

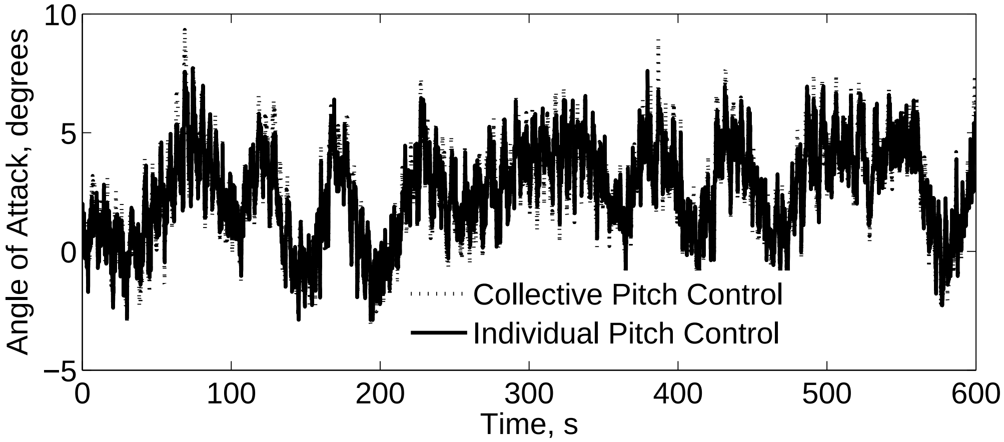

Figure 2.17: Attack angle comparison between CPC and IPC for model with 74 m draft at 13 m/s mean wind speed. Reprinted with permission from Springer [10].

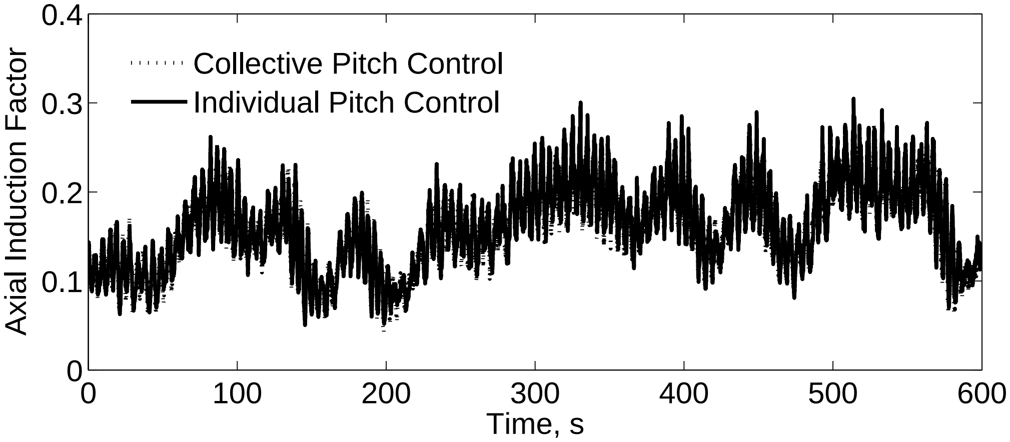

Figure 2.18: Axial induction factor comparison between CPC and IPC for model with 74 m draft at 13 m/s mean wind speed. Reprinted with permission from Springer [10].

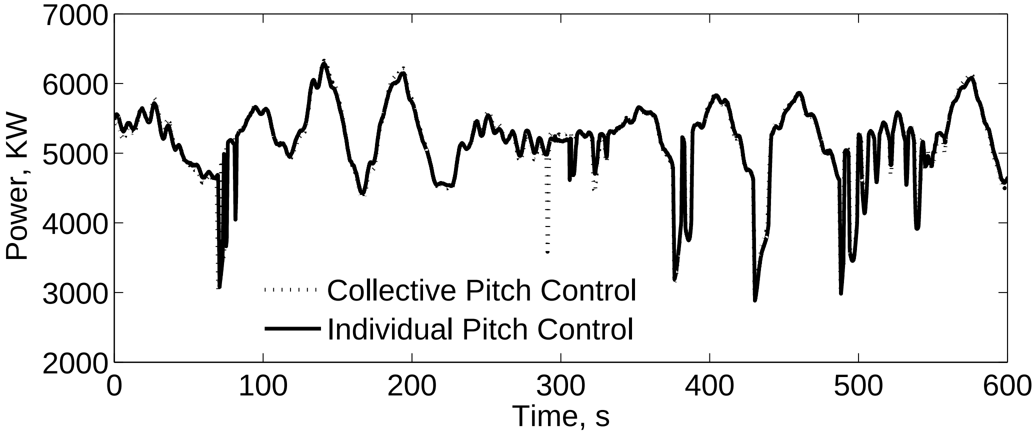

Figure 2.19: Power comparison between CPC and IPC for model with 74 m draft at 13 m/s mean wind speed. Reprinted with permission from Springer [10].

Time-domain simulations are also used to investigate the performance of individual pitch control. Figure 2.13 and Figure 2.14 display comparisons of the angle of attack and axial induction factor for collective pitch control and individual pitch control for condition with 13 m/s constant wind speed, 15 degree constant platform inclining angle, and no waves. The near-sinusoidal changes to the angle of attack and the axial induction factor result from the changing angle of the incoming wind relative to the blade as the blade rotates in the inclined plane of the rotor. Figure 2.13 shows that IPC maintains the angle of attack near a constant ideal value of about 2.2 degrees for this wind speed. Surprisingly, Figure 2.14 shows that the computed axial induction factor is only slightly improved despite significant improvement to the angle of attack. Figure 2.15 and Figure 2.16 display the blade pitch angles of CPC and IPC for the same condition respectively. The blade pitch angle of CPC is same for three blades and kept a value around 5.04 degrees, while the blade pitch angle of IPC is different for three blades and adjusted between 4.15 degrees and 6 degrees which maintains each blade at a better angle of attack.

Figure 2.17 and Figure 2.18 display comparisons of the angle of attack and axial induction factor for CPC and IPC for a wind turbine model with 74 m draft at 13 m/s wind speed. This case uses the wind speeds and wave conditions outlined in section 6. The same random seed is used for

CPC and IPC simulations. Figure 2.17 shows that IPC maintains the angle of attack to have lower peak and higher trough for each time step, keeping each blade close to an ideal angle. Figure 2.19 shows that there is only slight difference in power output associated with IPC: computed mean power output is enhanced by only about 0.8% compared with conventional CPC. The change is so slight even for these idealized conditions that this implementation of IPC is found not to be a viable way to enhance output power. The surprisingly good relative performance of CPC may result from blade design intended to accommodate horizontal misalignment between the spin axis and incoming wind caused by changing wind direction. Application of AeroDyn to this numerical experiment was well-beyond the intended use of that software; it may be that more advanced aerodynamic computation would yield a different overall conclusion, but these preliminary results are not promising.

2.7 Conclusions

It has been shown that lower-cost, more flexible foundation structures are more cost-effective than the very stiff designs represented by the OC3-Hywind concept. A family of seven truncated spar-type platforms have been designed in conformance with API Bulletin 2U, each of which is based on the OC3-Hywind concept. The MCM in Euler space is used to evaluate the large angle dynamics of the new designs because rotational motions of some of the truncated floaters are large enough to violate the small angle assumptions commonly applied in industry-standard simulation codes. AeroDyn is used to compute the aero-elastic loads on the blades and the DISCON subroutine is used to apply torque control and blade pitch control for wind speeds below and above the rated wind speed, respectively.

Moderate reductions in platform length have been shown to save on foundation cost without significantly decreasing electricity generation. The optimal floater draft is found to be around 74 m; even shorter designs have been found to be cost-effective in very high wind locations. All designs with lengths greater than 80 m have nearly the same power generation as the existing 120 m OC3-Hywind design. The overall conclusion is that the optimal hull size for spar-based FOWT's, from a cost-effectiveness point of view, is much smaller than conventional designs. An idealized individual blade pitch control strategy has been proposed and implemented in this work. Results indicate that IPC is not an effective way to increase power generation.

3. A SEMI-EMPIRICAL WAKE MODEL FOR YAWED OR TILTED WIND TURBINES BASED ON THE JOUKOWSKI TRANSFORMATION

3.1 Introduction

Wind is a fast-growing source of renewable energy. The largest wind farm is the massive Gansu Wind Farm in China, with a total of 7,000 wind turbines generating 7,965 MW electricity [57], the largest offshore wind farm is the Walney Extension, with 87 wind turbines and a capacity of 659 MW off the coast of Cumbria, England [58]. The wake of a wind turbine can impact both the efficiency of energy generation and the fatigue life of blades of downstream turbines. Wake effects can be mitigated by placing the turbines further apart, at the price of having fewer wind turbines within the boundary of a wind farm. The wake of a turbine can also be altered or redirected by tilting or yawing the rotor relative to the wind. The effect of tilting and yawing rotors takes on new importance in light of a new class of floating offshore wind turbine support structures that allows relatively large angles of inclination of the supporting tower. Analytical wake models enable estimation of wake effects with considerably lower computational intensity than numerically modeling the wake field. The new wake model proposed here enables efficient prediction of the far wakes of wind turbines whose rotors are not perpendicular to the incident wind.

Analytical methods are commonly used to describe wake velocity deficits and wake boundaries using simple geometric shapes because these methods require little or no simulation expense. The wake of an axisymmetric jet in a co-flowing uniform stream can be divided into three regions: an initial region, a transition region, and a fully developed region [59]. This characterization is applied to wind turbines to describe the self-similar wake velocity profile by Lissaman [60] and Voutsinas et al. [37]. Jensen [14] and Katic et al. [15] propose a simple wake model that describes the wake velocity deficit as a top-hat shape. The derivation is theoretically based on conservation of momentum, assuming that the wake velocity deficit is constant inside the wake, and that the wake expands linearly. The top-hat wake model can be represented as [15]:

$$\frac{\triangle U}{U} = \frac{1 - \sqrt{1 - C_T}}{(1 + 2kx/D)^2} \tag{3.1}$$

in which $\triangle U$ is the wake velocity deficit, U is the free stream velocity, C_T is the thrust coefficient, k is the wake growth rate, x is the downstream distance, and D is the turbine diameter. This simple top-hat wake model is commonly used in commercial software such as the DTU Wind Energy wind resource program WAsP [61], OpenWind [62], and GH Windfarmer [63]. Frandsen et al. [16] propose an enhancement to the top-hat model applicable to both single and multiple turbines with constant wake and nonlinear wake expansion.

Several alternate wake models have been proposed that more closely match the observed wake velocity deficit for rotors perpendicular to the wind. The wake deficit has been observed to be distributed approximately as a Gaussian shape in the far wake in numerous wind-tunnel experiments and numerical simulations (e.g., [38] and [39]). An alternate Gaussian-shaped model is proposed to describe the far wake profile by Bastankhah and Porté-Agel [17]. The derivation of each of these Gaussian models is based on conservation of mass and momentum. The conventional top-hat and Gaussian-shaped wake models describe the far wake profile for horizontal axis wind turbines with incoming winds perpendicular to the rotation plane.

Jiménez et al. [40] propose a more advanced wake model that accounts for rotors that are yawed relative to the incoming wind. The wake center and wake profile are affected by the angle between the wind and the rotation plane, such that this model is applicable to both yawed and tilted rotors (Figure 3.1). Jiménez's model is based on conservation of momentum and mass with the same underlying assumptions as the top-hat model: the wake expands linearly and the wake velocity deficit is constant inside the wake. The wake velocity deficit and the wake center shift angle α of a turbine with yaw angle θ predicted by Jiménez et al. are:

$$\frac{\triangle U}{U} \approx \frac{cos^3\theta C_T/2}{(1 + 2kx/D)^2} \tag{3.2}$$

$$\alpha \approx \frac{cos^2\theta sin\theta C_T/2}{(1+2kx/D)^2} \tag{3.3}$$

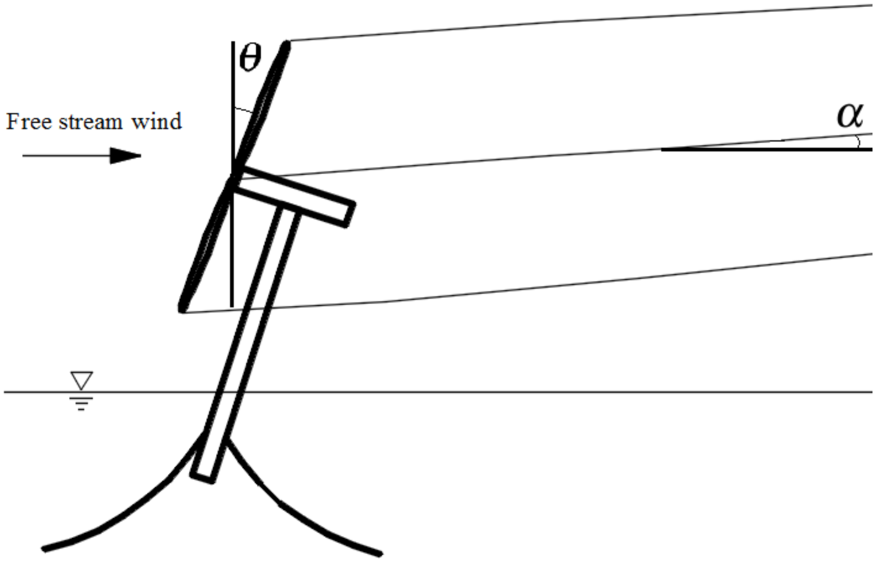

Figure 3.1: Wake flow of a turbine with an inclining tower.

More recently, the shape of the far wake of a yawed turbine has been observed to have an asymmetric kidney shape; there is no existing analytical model that describes this phenomenon. The kidney shape is first reported by Howland et al. [18], who study the wake under uniform inflow conditions for yawed turbines both experimentally and numerically. Bastankhah and Porté-Agel [19] apply conservation of mass to qualitatively explain that the formation of the kidney shape results from the counter-rotating vortex pair (CVP). They derive a wake profile based on the governing equations of the fluid field for a yawed turbine without considering the kidney shape of the wake. A new Gaussian-based wake model for a yawed turbine has recently been developed analytically by Qian and Ishihara [20], but this model also does not describe the kidney shape.

The wake growth rate is an important factor to estimate the influence of the wake on downstream turbines. The wake boundary is commonly defined as being the position at which the mean wake velocity is equal to 95% of the free-stream velocity at the hub height of the upstream turbine, but application of this definition requires the velocity distribution of the wake flow field to be available ([64], [40], and [20]). Analytical models with assumed wake expansion profiles are commonly used when detailed flow fields are not known. The wake is assumed to expand linearly, as in both the top-hat and the Gaussian wake models. Jensen [14] recommends a constant value of 0.1 for the wake growth rate, k, in his top-hat model, in which the wake diameter is described as $D_x = 2kx + D$. Katic et al. [15] comment that a constant k=0.11 fits their experimental measurements. WAsP [61] suggests that the values for k are 0.025 and 0.0375 for offshore and onshore conditions respectively, which are commonly used ([65], [66]). Bastankhah and Porté-Agel [17] adjust the value of k from 0.023 to 0.031 to fit different numerical simulation cases.

The main advantage of analytical wake models is that the wake can be predicted with minimal computational expense, while the main disadvantage is the lack of accurate detail in the wake velocity field. Computational fluid dynamic (CFD) methods have the opposite characteristics: the main advantage is the ability to compute details of the wake flow fields; the main disadvantage is the complexity required to create wind turbine models and the extremely large computational intensity necessary to model a large wind domain. Advanced CFD methods based on solving the Navier-Stokes equations are broadly used to model the wake domain, and simulation results can be used to assess the effectiveness of various wake models. The Open Source Field Operation and Manipulation (OpenFOAM) [24] is an open source code developed to perform CFD simulations. The transient pisoFoam solver in OpenFOAM is designed to solve incompressible turbulent flow. The "piso" refers to the PISO algorithm (Pressure-Implicit with Splitting of Operators). It reduces computational expense by enabling use of larger time steps. This solver includes the large eddy simulation (LES) turbulence model that is generally applied to compute the flow field of the turbine wakes. The Simulator for Wind Farm Applications (SOWFA) [25] is used to solve the wake field and inflow turbulence. SOWFA is developed at the National Renewable Energy Laboratory (NREL) with a computational core based on OpenFOAM. The pisoFoamTurbine solver in SOWFA is based on the OpenFOAM pisoFoam solver. This solver applies actuator line models (ALM's) to represent the effect the turbine has on the wind. Both OpenFOAM and SOWFA are commonly used to study the flow field of wind turbines. Tossas and Leonardi [67] apply actuator disk models (ADM's) and ALM's to represent turbines in OpenFOAM and compare turbine wakes and the wake-turbine interaction between the two turbine models. Churchfield et al. [68] improve SOWFA to enable any subgrid-scale model and simulate flow over hilly terrain. Fleming et al. [69] optimize the wind-plant performance with yaw and tilt controls based on simulation results from SOWFA by using ALM's. Bhaganagar and Debnath [26] study the interactions between the wake flow of turbines and the atmospheric boundary layer by using ALM's to represent turbines in OpenFOAM. Gebraad et al. [27] demonstrate the potential to maximize energy production using yaw control to decrease the wake effects to the downstream turbines using SOWFA.

The NREL 5-MW turbine [4] is a numerical model of a wind turbine that is used extensively for both onshore and offshore studies and is used in this work as a base-case structure. The cut-in, rated, and cut-out wind speeds of this turbine are 3 m/s, 11.4 m/s, and 25 m/s respectively, the start-up and rated rotor speeds are 6.9 rpm and 12.1 rpm respectively, the blade run-pitch value is 0 degrees, and the rated generator torque is 43,094 Nm. The OC3-Hywind model is a combination of this 5-MW turbine and a spar-type floating support structure [4], which is commonly used as a baseline floating offshore wind turbine (FOWT) model in numerical studies. Several truncated spar-type floaters have been newly designed based on the OC3-Hywind model [10]. These new designs are applied as numerical models in this work to assess the effects of large rotational motion in the pitch direction.

The new analytical wake model developed here overcomes many of the limitations of existing models. Most theoretical wake models are derived by treating the turbine as a circular disk, neglecting important effects associated with three individual blades. This work divides each blade into several segments. Each segment has its own airfoil properties including angle of attack for computation of lift and drag coefficients. The thrust coefficient is computed from these physical properties of each segment along the blade. The wake velocity deficit is commonly expressed as a function of the thrust coefficient as shown in Equations 3.1 and 3.2. The proposed new semi-empirical wake model shares the theoretical basis of Jiménez's wake model for a yawed turbine, but extends that prior work to account for the change of thrust coefficient along the length of blade.

The analytical model developed here is also the first to describe the kidney shape of the wake of a yawed turbine. The development makes use of a conformal mapping technique developed by Joukowski [70]. The mapping can be used to convert a circular cylinder into a family of teardrop or oval shapes, and has been broadly used in fluid dynamics to solve the potential flow around airfoils. The Joukowski transformation is used here to describe the wake transformation from a circular shape into the deformed kidney-shaped or oval wake.

The development of the new semi-empirical Joukowski-transformation-based far wake model for a yawed or tilted turbine is presented in Section 3.2; details of the numerical simulation models in SOWFA and the comparison between the newly developed Joukowski-transformation-based wake model and the simulation results are presented and analyzed in Section 3.3; conclusions are presented in Section 3.4.

3.2 Derivation, Calibration, and Application of the Wake Model for a Yawed or Tilted Turbine

The wake of a yawed or tilted wind turbine develops into a kidney shape in the far wake if the yaw or tilt angle is greater than 10 degrees and the incoming wind component perpendicular to the rotational plane is smaller than the rated wind speed; the wake has an oval shape for other conditions. The derivation of the new wake model in Section 3.2.1 is applicable to both kidney-shaped and oval wake velocity profiles. Details of the Joukowski-transformation parameters are discussed in Section 3.2.2. Detailed steps to apply the new wake model are described in Section 3.2.3.

3.2.1 Derivation of the Joukowski-transformation-based Wake Model

There are four main steps to the development of the Joukowski-transformation-based wake model: 1) predicting the wake shape based on the yaw or tilt angle and the incoming wind speed; 2) computing the velocity deficit for a circular wake cross section; 3) mapping the circular shape to a kidney or oval shape; 4) rescaling the kidney-shaped or oval wake to conserve momentum.

The second step in the derivation relies on the same assumptions as the existing Jiménez's wake model, but conservation of momentum and mass is applied over a series of concentric rings instead of a single control volume. The third step is based on tuning a small number of free parameters in the Joukowski conformal mapping such that the transformed wake field matches local velocities computed using CFD.

The wake model of a tilted turbine is shown in Figure 3.2. The derivation of the profile of the new wake model is based on conservation of momentum inside several annular control volumes inside the area surrounded by the dashed lines. The upstream inlet of these control volumes is a vertical plane just ahead of the turbine rotor and the downstream outlets are at some distance downstream, perpendicular to the wake velocity. Turbine blades are divided into several segments along the length of the blade such that each segment generates a circular band in the plane of rotation, which is shown in the front view. Each circular band develops into an oval annulus as it moves downstream in the wake. Conservation of momentum is applied to each smaller control volume. The mass flow entering the control volume at the inlet is m_1, the mass flow entering the control volume through the wake boundary by crossing the outermost annulus is m_2, and the mass flow exiting the downstream boundary of the control volume is m_3. The centerline in this figure represents the shifted wake center. The angle θ is the tilt angle of the turbine and α is the shift angle of the wake center.

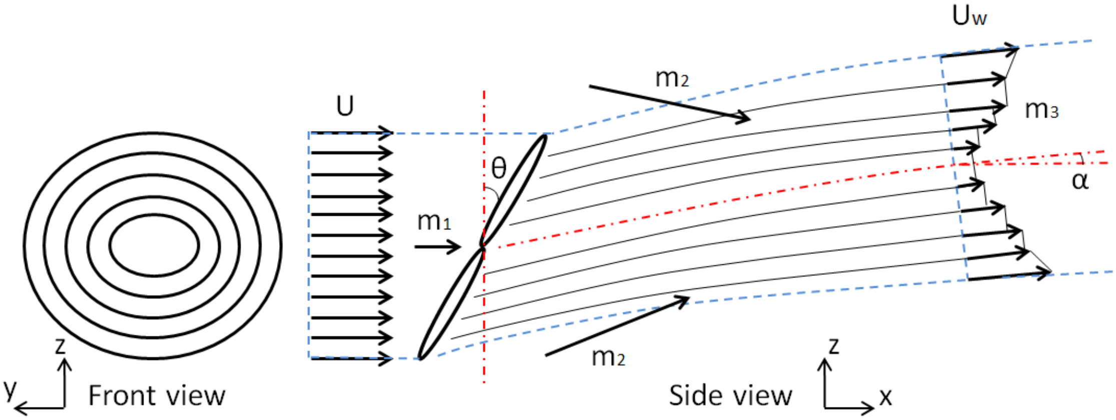

Figure 3.2: Control volume of wake flow of a tilted turbine.

The initial cross section of the wake is assumed to be a circle immediately downstream of and parallel to the turbine rotational plane. The wake velocity deficit at any downstream distance x within a concentric annulus relates to the corresponding circular path of a single element along the blade within the rotational plane. The wake velocity within each annulus is assumed to be constant at any location x, and the momentum of each annulus is conserved:

$$\vec{F_i} = m_{3i}\vec{U_{wi}} - m_{1i}\vec{U_{1i}} - m_{2i}\vec{U_{2i}} \tag{3.4}$$

in which parameters with arrows represent vectors, $\vec{F_i}$ is the thrust force acting on the ith control volume, m_{3i} is the mass flow exiting the ith control volume, $\vec{U_{wi}} = \vec{U} - \triangle\vec{U}_{wi}$, m_{1i} is the mass flow entering the ith control volume at the inlet, $\vec{U_{1i}}$ is the velocity at the upstream entrance of the ith control volume and is equal to the free-stream velocity $\vec{U}$, m_{2i} is the mass flow entering the side of the ith control volume, and $\vec{U_{2i}}$ is the velocity of the mass flow and is assumed equal to $\vec{U}$ in conformance with the assumptions of small wake velocity deficit and small wake shift angle. Conservation of mass is applied to each annulus:

$$m_{1i} + m_{2i} = m_{3i} \tag{3.5}$$

in which $m_{3i} = \rho A_{wi} U_{wi} \approx \rho A_{wi} U_i$ for small $\triangle\vec{U}_{wi}$, ρ is the air density, and A_{wi} is the wake area corresponding to the ith annulus, which is the difference between the areas of the (i+1)th and the ith circles. The radius of the ith circle at any downstream distance x is computed by multiplying the wake expansion factor by the radius of the corresponding circle at the inlet. The wake expansion factor used in this work is computed from the wake boundary where the mean wake velocity equals 95% of the free-stream velocity. Combing Equations 3.4 and 3.5, decomposing into the x and z directions (Figure 3.2), and then assuming the wake shift angle α and the wake velocity deficit $\triangle\vec{U}_{wi}$ are both small, the x-component of Equation 3.4 is expressed as:

$$F_{xi} = m_{3i}[(U_i - \triangle U_{wi})cos\alpha - U_i] \approx -m_{3i} \triangle U_{wi} \approx -\rho A_{wi} U_i \triangle U_{wi} \tag{3.6}$$

Application of conservation of mass and momentum to each annulus effectively applies these conservation laws to the total wake. The thrust force acting on the ith control volume is equal to $(C_{Ti}/2)\rho A_i(U_i cos\theta)^2$, in which $U_i cos\theta$ is the wind velocity component perpendicular to the rotational plane, and A_i is the frontal area of the rotational plane corresponding to the ith annulus. The thrust is decomposed into its x and z components and the component in the x direction is:

$$F_{xi} = -F_i cos\theta = -\frac{C_{Ti}}{2}\rho A_i(U_i cos\theta)^2 cos\theta \tag{3.7}$$

The wake velocity deficit ratio is computed by substituting Equation 3.7 into Equation 3.6, which completes the second step in the development of the new wake model:

$$\frac{\triangle U_{wi}}{U_i} \approx \frac{C_{Ti}}{2}\frac{A_i}{A_{wi}}cos^3\theta \tag{3.8}$$

The third step of the derivation is to develop a mathematical transformation to map each circular annular area into either a kidney or oval shape. The wake annuli are oval in the near-wake, and deform as they travel downstream. Each annulus will either evolve into a kidney shape or remain oval, depending on the magnitude and direction of the incoming wind relative to the rotational plane. The downstream shape is predicted using Joukowski parameter λ. Analytical representations of λ and related parameters η_m and η_n have been developed from CFD simulation results. The coordinates of a circle of radius r centered at (η_m, η_n) on a complex plane mapped to another complex plane using the Joukowski transformation are given by:

$$\zeta(\eta) = \frac{1}{2}\left(\eta + \frac{\lambda}{\eta}\right) \tag{3.9}$$

$$\eta = r\cos\beta + ir\sin\beta + (\eta_m + i\eta_n) \tag{3.10}$$

$$\lambda = \left(-\eta_m + \sqrt{r^2 - \eta_n^2}\right)^2 \quad for \quad a \quad kidney \quad shape \tag{3.11a}$$

$$\lambda = 0.05 \quad for \quad an \quad oval \tag{3.11b}$$

in which η represents a circle in a complex plane before transformation, and β is an angle ranging from 0 to 2π measured counterclockwise from the horizontal. The circular area is mapped to a kidney shape if η_m and η_n are non-zero and λ is a function of η_m and η_n (Equation 3.11a), and mapped to an oval if η_m and η_n are both zero and λ is equal to a constant value of 0.05 (Equation 3.11b). Figure 3.3 and Figure 3.4 show the effect of mathematical parameters (η_m, η_n) on the transformation. These parameters are used for adjusting the transformed shape only, and have no relationship with the physical location in the xyz coordinate system. The physical location of the center of the circle is at the center of the cross-section of the wake at downstream distance x.

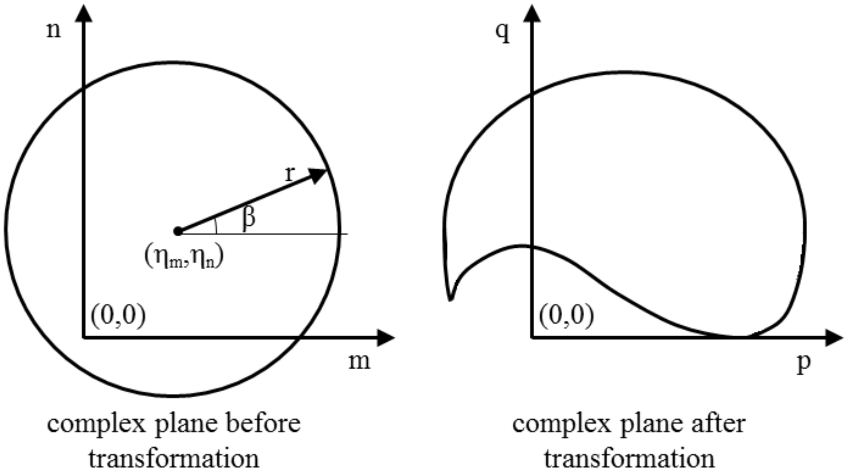

Figure 3.3: Circle to kidney shape.

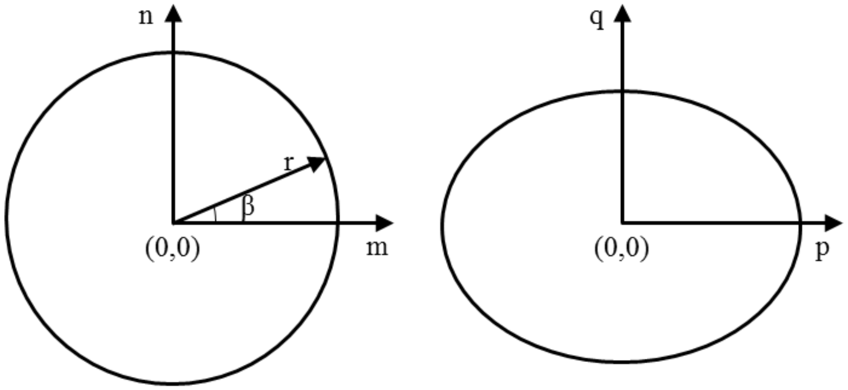

complex plane before transformation

complex plane after transformation

Figure 3.4: Circle to oval.

The last step of the derivation is application of conservation of momentum across the Joukowski transformation. Regardless of whether Equation 3.9 results in a kidney shape or an oval, the area is not generally preserved through the transformation. The derivation for the kidney-shaped wake is presented in detail. The momentum of the ith annulus in the circular wake is:

$$M_{wi} = m_{wi}U_{wi} = \rho A_{wi}U_{wi}^2 \tag{3.12}$$

which is set equal to the momentum of the wind after the geometric transformation. The momentum of corresponding kidney-shaped ring is:

$$M_{wi} = M_{ki} = \rho A_{ki}U_{ki}^2 \tag{3.13}$$

in which M_{ki}, A_{ki}, and U_{ki} are the momentum, area, and wake velocity of the ith kidney-shaped ring. The area A_{ki} is straightforward to compute numerically as the area bounded by the two transformed kidney shapes corresponding to the (i+1)th and ith circles. Combining Equations 3.12 and 3.13 results in the velocity of the ith kidney-shaped ring in the wake field:

$$U_{ki} = U_{wi}\sqrt{\frac{A_{wi}}{A_{ki}}} = (U_i - \triangle U_{wi})\sqrt{\frac{A_{wi}}{A_{ki}}} \tag{3.14}$$

in which the wake velocity is scaled by $\sqrt{A_{wi}/A_{ki}}$ to maintain constant wake area through the mapping. The wake velocity deficit ratio of the ith kidney-shaped ring is expressed by combining Equations 3.8 and 3.14 and substituting $U_i - \triangle U_{ki}$ for U_{ki}:

$$\frac{\triangle U_{ki}}{U_i} = \frac{C_{Ti}}{2}\frac{A_i}{A_{wi}} cos^3\theta\sqrt{\frac{A_{wi}}{A_{ki}}} - \left(\sqrt{\frac{A_{wi}}{A_{ki}}} - 1\right) \tag{3.15}$$

An equivalent derivation has been developed for the oval wake annuli. The resulting wake velocity deficit ratio can also be expressed as Equation 3.15, but replacing every incidence of ki in the equation with oi to represent oval rather than kidney-shaped wakes.

The imperfection of this derivation is the assumption for the mass flow entering the side of each control volume. The velocity of this mass flow is set to be equal to the free stream velocity based on the assumptions of small wake velocity deficit and small wake shift angle, however, this velocity should be equal to the wake velocity at the side of each control volume. The accuracy of this assumption decreases from the outer control volume to the inner control volume and the error accumulates, such that the innermost control volume relating to the blade root and turbine hub experiences the maximum error and the mass flow m_{2i} is overestimated, which results in overestimation of the mass flow m_{3i} based on conservation of mass and finally leads to underestimation of the wake velocity deficit. Another defect of the wake model is the calculation of the thrust coefficient of the innermost control volume. The blade root and turbine hub do not generate thrust and the thrust coefficient of the blade element close to the blade root is applied as an approximation to the innermost control volume to compute the wake velocity deficit. These two imperfections result in inaccurate prediction of wake velocity deficit of the innermost control volume.

3.2.2 Calibration of the Parameters of the Joukowski Transformation

Functional representations of parameters η_m, η_n, and λ are presented for both kidney-shaped and oval wake deficits based on fitting data to a CFD model of a 5-MW wind turbine rotor. The effectiveness of these parameterizations is later demonstrated by benchmarking against CFD simulation results. The wake model is used by first determining if a kidney or an oval shape is expected, then computing the wake parameters. A kidney-shaped far wake develops for large angles of yaw or tilt combined with wind speeds below the rated speed of the turbine; an oval far wake develops for all other conditions.

3.2.2.1 Parameters for a Kidney Shape

The wake progresses to a kidney shape if the wind turbine is yawed or tilted more than 10 degrees from the incident wind direction and the incoming wind component perpendicular to the rotational plane is smaller than the rated speed. The wake cross section is divided into a series of concentric circles immediately of downstream of the rotor disk. These circles are mapped to kidney shapes by first mapping a unit circle centered at location (η_m, η_n) in a complex plane to a kidney shape, and scaling the resulting kidney shape by the radius of each circle. The unit circle is expressed as Equation 3.10 with $r = 1$, which is rewritten as $\eta = \cos\beta + i\sin\beta + (\eta_m + i\eta_n)$. The center of the unit circle in the complex plane varies as the wake travels downstream and evolves into a kidney shape. Parameters η_m and η_n have been determined from CFD results to vary linearly with the downstream distance x:

$$\eta_m = a_1 x + b_1 \tag{3.16}$$

$$\eta_n = a_2 x + b_2 \tag{3.17}$$

in which parameters a_1, b_1, a_2, and b_2 have been calibrated from numerical simulation results and found to be $-0.027/D$, 0.527, $0.027/D$, and 0.473, respectively. Parameter λ is computed from η_m and η_n using Equation 3.11a. The kidney shape is mapped from the unit circle using Equation 3.9 and scaled by the radius of the corresponding circle.

3.2.2.2 Parameters for an Oval Shape

The wake retains an oval shape if the wind turbine is yawed or tilted less than 10 degrees, or if the incoming wind component perpendicular to the rotation plane is greater than the rated speed. The assumed circular area of the wake cross section is divided into a series of concentric circles, each of which is mapped into an oval. A circle with radius r is mapped into an oval following two steps: an oval is first mapped from a unit circle centered at the origin of a complex plane, $\eta = \cos\beta + i\sin\beta$ (Equation 3.10), using Equation 3.9 with parameter λ set to the constant real value of 0.05 (Equation 3.11b); then the oval is scaled by the radius of the corresponding circle.

3.2.3 Application of the Joukowski-transformation-based Wake Model

The numerical values presented with the analytical representations of model parameters a_1, b_1, a_2, b_2, and λ are appropriate for the 5-MW turbine for which they are developed. Application of this model to predict the wake of a similar turbine includes four steps: The first step is to predict the Joukowski parameter λ based on the wake shape. A kidney-shaped far wake is expected if the yaw or tilt angle exceeds 10 degrees and the wind component perpendicular to the rotor disk is below the rated speed of the turbine; an oval wake exists for other conditions. Parameter λ is computed using Equation 3.11a for a kidney-shaped wake, and is set equal to the constant value of 0.05 for an oval wake (Equation 3.11b). The second step is to subdivide the circular wake area immediately downstream of the rotor disk into a series of concentric circles, which can be set equal to the number of discrete elements along the blade length. The ith annular ring has the area A_{wi} and the thrust coefficient C_{Ti} computed using blade element method with tools such as AeroDyn [52]. The radius of the wake at any downstream distance x can be found from Figure 3.10 directly, or computed using $R_x = kx + R$, in which the wake expansion factor k is assumed to be a reasonable value such as 0.025 recommended by WAsP for offshore conditions [61]. The third step is to apply the Joukowski transformation (Equation 3.9). The transformed wake area A_{ki} of the ith kidney-shaped band or A_{oi} of the ith oval band is computed numerically as the difference between the outer and inner kidney shapes or ovals. The fourth step is to compute the wake velocity deficit for each kidney-shaped or oval band using Equation 3.15.

Application of the new wake model to other wind turbines requires recalibration of transformation parameters a_1, b_1, a_2, b_2, and λ from CFD simulation results as well as simulation of a few cases near the criteria for prediction of a kidney-shaped or oval wake to confirm the general wake behavior. At least one case for kidney-shaped wakes and at least one case for oval wakes would need to be computed to calibrate the model.

3.3 Validation of the Joukowski-transformation-based Wake Model Using Simulation Results

The transformation parameters η_m, η_n, and λ have been developed to calibrate the new wake model to match CFD-based simulation results. Numerous numerical simulations are performed for FOWT models with varying hull drafts and subject to different free stream wind conditions to quantitatively describe the wake flow field. The pisoFoamTurbine solver in SOWFA is used to compute the flow field. Simulation results are then used to calibrate the new wake model including explicitly accounting for large angles of inclination.

3.3.1 Simulation Models

A set of numerical simulations are performed for a series of three floating platform designs using pisoFoamTurbine solver to compute the wake flow field of each FOWT. Each time-domain simulation is for a steady wind and constant rotational displacement in the pitch direction. The wake is computed in a 3-D rectangular flow field domain in a Cartesian coordinate system, with the x-axis along the free stream direction, the z-axis pointing upward, and the y-axis in accordance with the right hand rule. The dimension of the flow field is $13D$ by $6D$ by $3D$ in x, y, and z directions, respectively, where D is the 126 m diameter of the NREL 5-MW turbine. The distance from the flow field inlet to the turbine inlet is $3D$; the wake flow is observed up to $10D$ away from the turbine as shown in Figure 3.5. The grid size around the wind turbine and wake flow is smaller than 2 m and the time step is set to 0.05 s, which satisfies the Courant-Friedrichs-Lewy (CFL) condition [43]. The effects of ocean waves and of environmental turbulence are neglected. The vertical distribution of horizontal mean wind speeds at the inlet boundary condition is assumed to be logarithmic, as is typical for a neutral stability condition [35]:

$$u(z) = u(z_{ref}) \frac{ln(z/z_0)}{ln(z_{ref}/z_0)} \tag{3.18}$$

in which $u(z)$ is the wind speed at height z, z_{ref} is the reference height, which is the hub height and is equal to 90 m, z_0 is the roughness length, which is assumed to be 0.0002 m for the sea surface in accordance with the European Wind Atlas [36]. The boundary of the sea surface is considered a no-slip condition, implicitly assuming the wind speed at the sea surface is zero, which is compatible with the logarithmic wind profile. The ALM is used to model the wind turbine. The turbine blades are treated as straight lines and the loads along the lines are treated as the body forces in the Navier-Stokes equation.

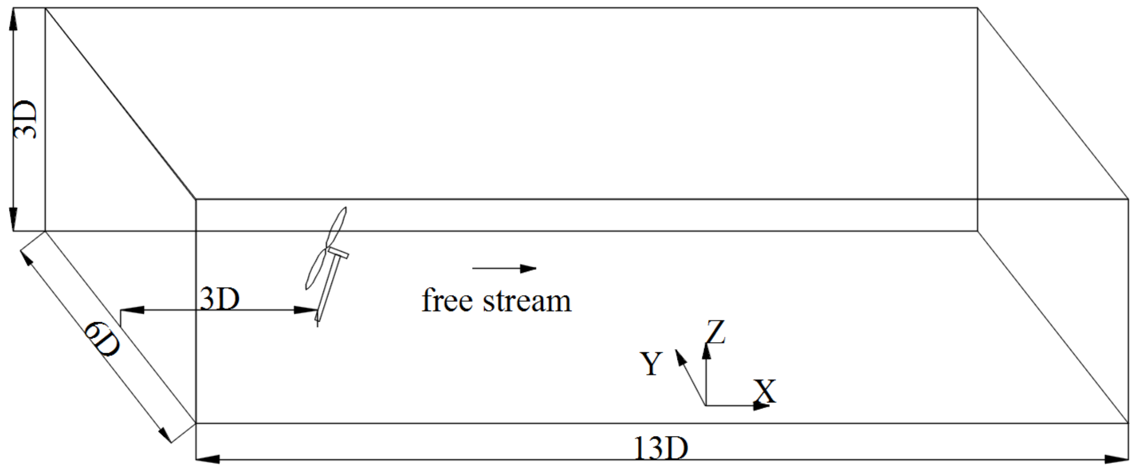

Figure 3.5: Simulation flow domain.

The wake flows are numerically simulated for three FOWT designs with drafts of 120 m, 74 m, and 67 m [10]. The model with 120 m draft is selected as the base case because it has the smallest rotational motion and is very similar to the well-known OC3-Hywind numerical model; the model with 74 m draft is the optimal design for power generation vs structural cost; the model with 67 m draft is realistic but not optimal, and is included to investigate the wake effects associated with large overall angles of rotor inclination. Table 3.1 shows the mean platform pitch angles for hub-height wind speeds varying from 9 to 15 m/s. Each of these constant pitch angles is computed by performing a 600 second fully dynamic simulation using the in-house large-angle time-domain wind turbine simulator, Loose [9], and then computing the mean of the angular displacements after all transients have passed. Significant wave heights and wave periods associated with the hub-height wind speeds are computed using Equation 2.17, and current and surface stretching effect are not considered in Loose.

Table 3.1: Mean platform pitch angles relevant to hub-height wind speeds for three FOWT designs

Case No.	Wind Speed [m/s]	Draft [m]	Pitch [°]
1	9.0	67	18.8
2	9.0	74	11.0
3	9.0	120	2.4
4	11.0	67	23.4
5	11.0	74	13.8
6	11.0	120	2.9
7	13.0	67	22.4
8	13.0	74	12.0
9	13.0	120	2.5
10	15.0	67	19.4
11	15.0	74	10.3
12	15.0	120	2.1

3.3.2 Comparison between the Joukowski-transformation-based Wake Model and Simulation Results

Wakes predicted by the Joukowski-transformation-based wake model are qualitatively compared with those resulting from numerical simulations. The incoming wind speed for each of twelve cases is assumed to be steady in time but to vary with altitude. All twelve cases used in the calibrations are included in the comparison: four incoming free-stream wind speeds from 9 to 15 m/s in 2 m/s increments for each of the three floater designs. Wakes predicted by the calibrated analytical model are shown to have similar shapes and velocity distributions as computed CFD results.

Figure 3.6 shows the change of the normalized streamwise wake velocity in the Y-Z plane at various distances downstream of a turbine. The simulation is of a turbine with a 74 m draft subject to 11 m/s wind speed, which is Case 5 in Table 3.1. The origin of the coordinate system for these simulation results is fixed at $(x, y, z) = (0, 0, 90)$, with x, y, and z defined in Figure 3.5. Each of the three dimensions is normalized by the turbine diameter. The dashed ovals represent the rotational areas of the upstream turbines. The solid curved lines represent the boundaries of the turbine wake at different distances downstream predicted using the Joukowski-transformation-based wake model. The predicted kidney-shaped wake boundaries and internal velocity distributions generally agree with the simulation results.

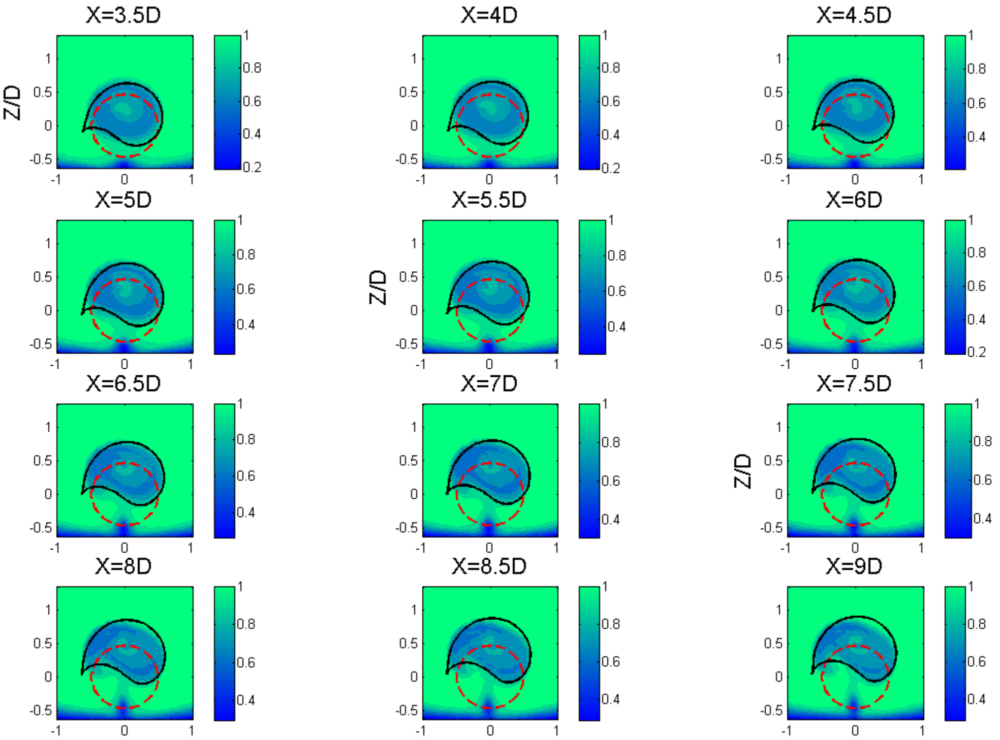

Figure 3.6: Normalized streamwise velocity on the Y-Z plane at various distances downstream for FOWT with 74 m draft subject to 11 m/s wind speed.

Figure 3.7 shows the normalized streamwise velocity on the Y-Z plane at $7D$ downstream for all twelve cases in Table 3.1, (case numbers are shown in leading brackets and organized from left to right and then top to bottom). The wake develops a kidney shape in cases having wind component perpendicular to the rotational plane less than the rated speed, combined with large tilted angles, i.e. Cases 1, 2, 4, 5, and 7. The wake does not develop a kidney shape in cases having tilt angle less than 10 degrees (Cases 3, 6, 9, and 12), and cases having wind component perpendicular to the rotational plane greater than the rated speed (Cases 8 to 12). Both the kidney and oval shapes match the shape of the wake expansion well. The wake deficit ratio decreases as the free-stream wind speed increases above the rated speed (Cases 4, 7, and 10); this wake behavior is reasonable because the controller feathers the blade to reduce aerodynamic loads. The wake centers of turbines with smaller tower pitch angles at the same wind speed have a smaller upward shift, e.g. comparing Cases 1 and 3, Cases 4 and 6, Cases 7 and 9, and Cases 10 and 12.

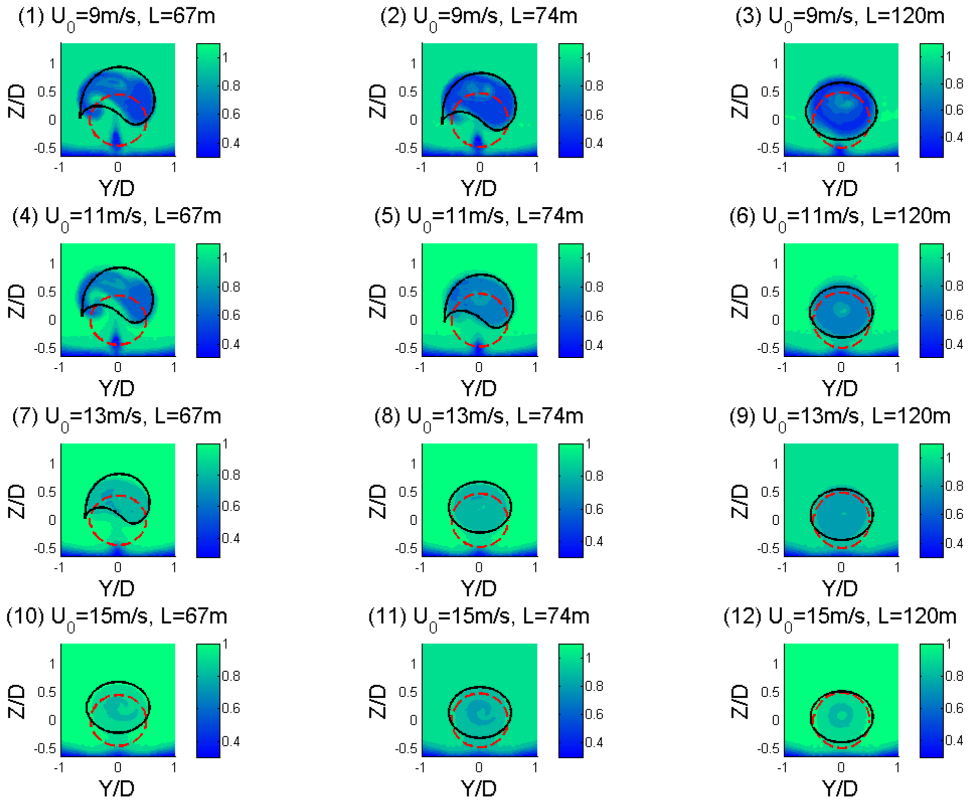
(1) U_0=9m/s, L=67m
(2) U_0=9m/s, L=74m
(3) U_0=9m/s, L=120m
(4) U_0=11m/s, L=67m
(5) U_0=11m/s, L=74m
(6) U_0=11m/s, L=120m
(7) U_0=13m/s, L=67m
(8) U_0=13m/s, L=74m
(9) U_0=13m/s, L=120m
(10) U_0=15m/s, L=67m
(11) U_0=15m/s, L=74m
(12) U_0=15m/s, L=120m

Figure 3.7: Normalized streamwise velocity at X=$7D$.

Figure 3.8 shows the normalized wake velocity deficit ratios computed using Equation 3.15 compared with CFD simulation results. The wake velocity deficits shown are along the spanwise direction for the right half of the downstream rotor, vertically aligned with the wake center, and $7D$ downstream for all twelve cases shown in Table 3.1. The velocity deficit ratios computed using the new wake model agree well with the simulation results for most cases. The wake velocity deficit ratios of the simulation results for cases with smaller wind components (Cases 1, 2, 4) are greater than the ratios computed from the new wake model for the area close to the turbine center, while the ratios of simulation results for cases with greater wind components (Cases 6, 8, 9, 11, 12) are smaller than the ratios computed from the new wake model. This trend in prediction is believed to be caused by two completely separate sources. The new wake model does not handle the hub wake vigorously, and the errors implied by the assumption of constant velocity U_{2i} of the mass flow m_{2i} accumulate in the hub annulus. Additionally, the detailed numerical model used in the comparison case based on CFD simulation does not include accurate representation of the hub, and subsequently does not predict the wake close to the hub center well.

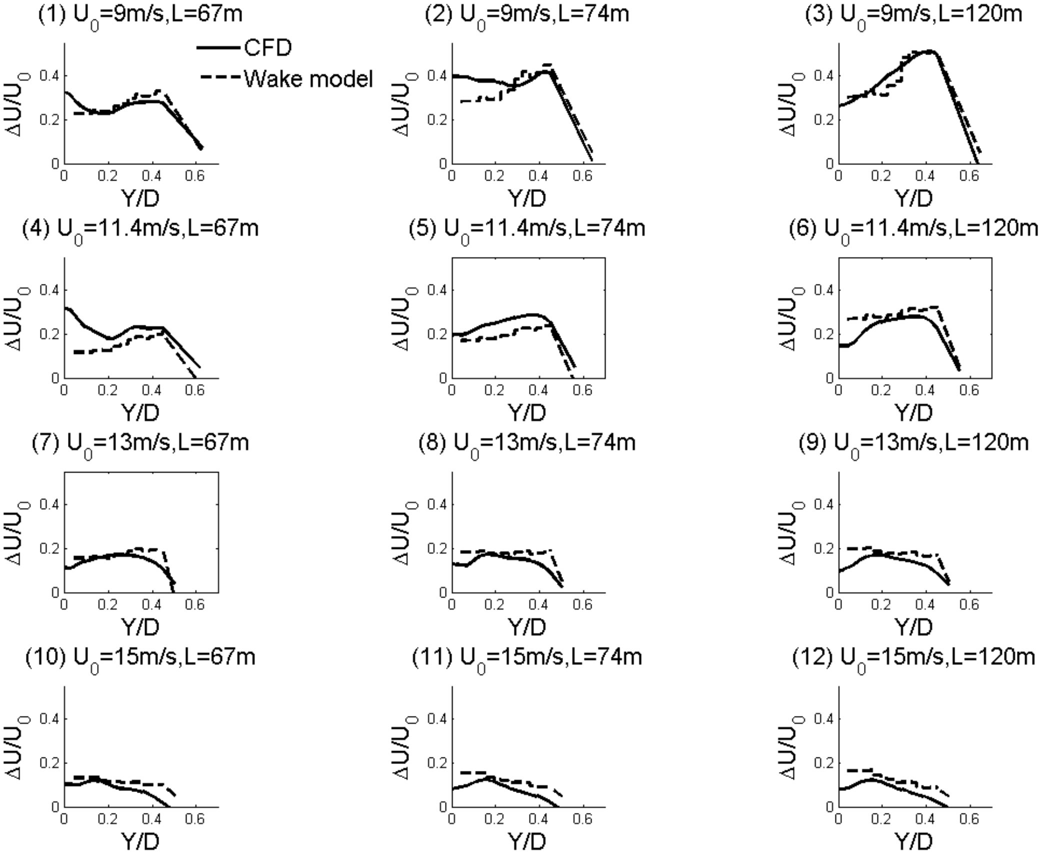

Figure 3.8: Normalized streamwise velocity profile along spanwise direction at X=$7D$, Z=Wake Center.

Figure 3.9 shows the comparison between the new wake model and CFD results for the normalized average wake velocity inside wake boundary at $7D$ downstream. The difference between these two methods is less than 5% for all twelve cases, except Case 4. The Case 4 difference is still within 10% and it appears that imperfect hub wake modeling may be having a relatively large effect on this case.

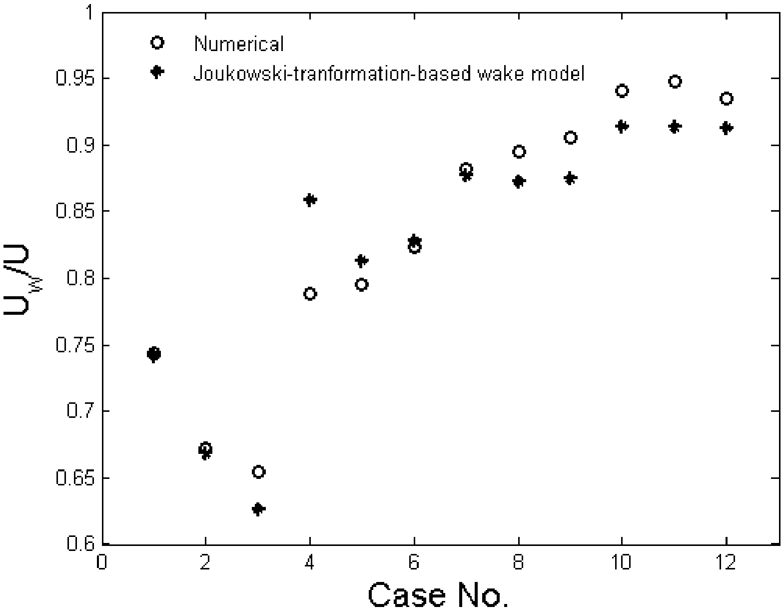

Figure 3.9: Normalized average wake velocity inside wake boundary at X=7D.

The complete set of values used in the calibration of all twelve cases is presented in Table 3.2. Parameter C_{Tmean} is the mean thrust coefficient computed using AeroDyn, k is the wake expansion factor at $7D$ downstream computed from the CFD simulation results, and Z/D is the normalized distance that wake center shifts.

Table 3.2: Mean thrust coefficient, wake expansion factor, and wake center shift distance

Case No.	C_{Tmean} [-]	k [-]	Z/D [-]
1	0.770	0.018	0.45
2	0.765	0.019	0.34
3	0.760	0.020	0.21
4	0.714	0.016	0.47
5	0.672	0.008	0.30
6	0.624	0.007	0.19
7	0.591	0.005	0.30
8	0.505	0.005	0.24
9	0.461	0.005	0.10
10	0.391	0.005	0.23
11	0.333	0.005	0.14
12	0.309	0.005	0.07

3.3.3 Wake Expansion and Shift

The area of reduced velocities impacting on downstream turbines is primarily determined by the wake expansion factor and the vertical distance the wake center shifts. The normalized wake radii of the twelve cases are shown in Figure 3.10. The wake boundary is defined as the border at which the mean wake velocity of the boundary is 95% of the free-stream velocity at the hub height of the upstream turbine defined by the CFD results. The wake radii of Cases 1 to 4 grow to over 120% of the rotor radius at the far wake; the wake radii of Cases 7 to 12 exhibit a wake expansion growing to about 110% of the rotor radius. The wake is observed to expand more for cases in which the free-stream wind speed is below the rated speed.

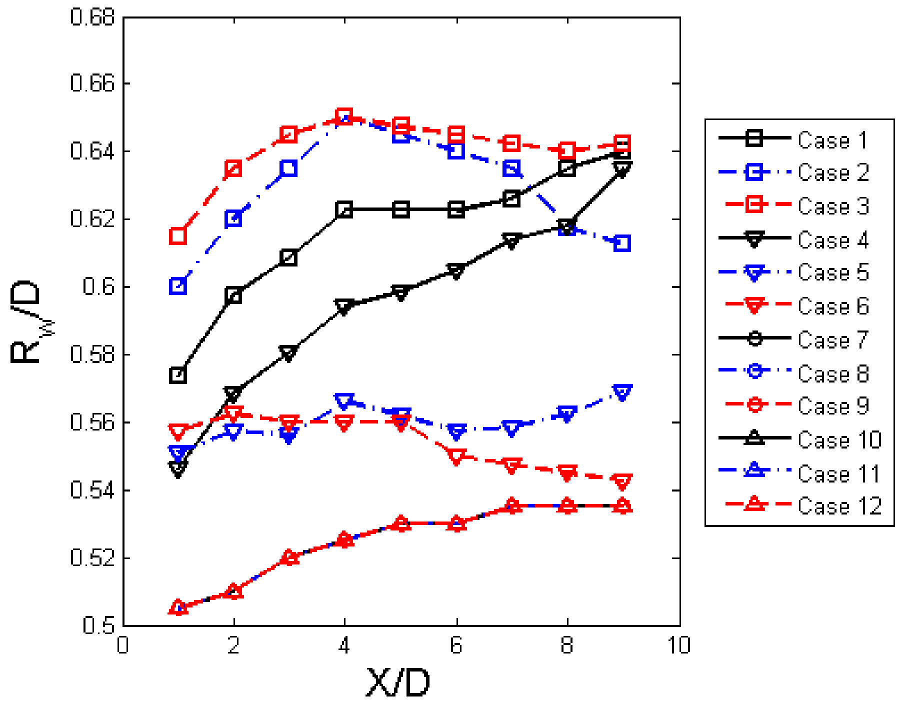

Figure 3.10: Comparison of wake radii.

Figure 3.11 shows the normalized distance the wake center shifts upward versus the normalized distance downstream for all twelve cases, computed using CFD. The wake center for Case 1 shifts upward by about $0.5D$ at $7D$ downstream, such that the lower half of a downstream turbine at $7D$ would be mostly below the wake boundary; greater power generation is expected in these relatively higher winds. The vertical distance the wake center shifts decreases with decreasing tower pitch, for the same incoming wind condition, e.g. comparing Cases 1 and 3, Cases 4 and 6, Cases 7 and 9, and Cases 10 and 12. The vertical distance the wake center shifts decreases as the incoming wind speed increases for the same turbine model, e.g. Cases 1, 4, 7, and 10, Cases 2, 5, 8, and 11, and Cases 3, 6, 9, and 12.

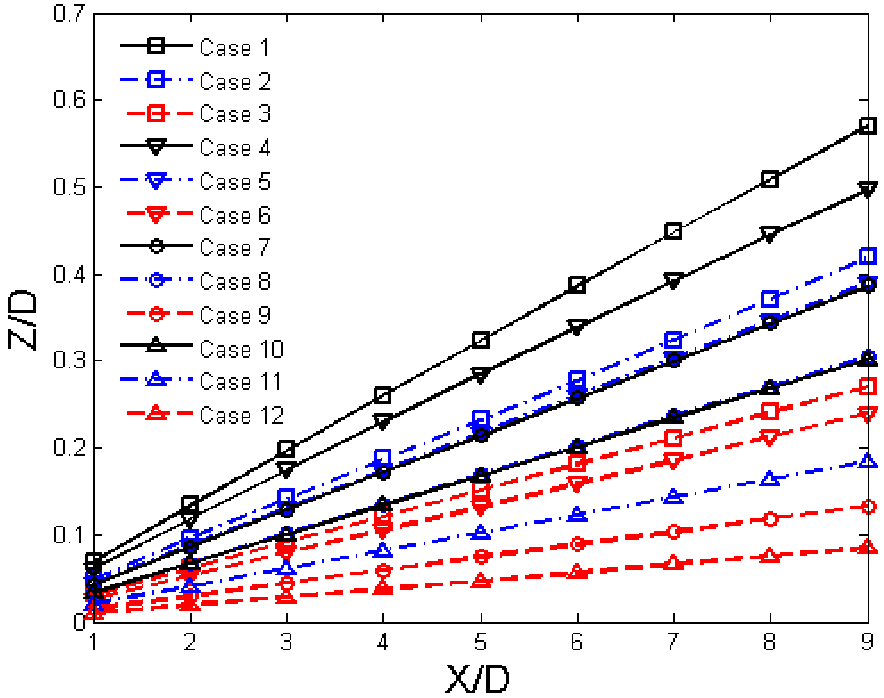

Figure 3.11: Comparison of wake center trajectories for twelve cases.

3.3.4 Vertical and Spanwise Wake Profiles

Wake velocity distributions within a wind farm could impact the performance of downstream turbines, including power generation and blade fatigue. Figure 3.12 shows the wake profiles computed using CFD simulation. A vertical section through the wake center at $7D$ downstream is shown for all twelve cases. The dot-dashed lines represent the logarithmic horizontal free-stream wind speeds. The wake shifts upward more for a turbine with larger angle of inclination at the same wind speed. The shift distance becomes less sensitive to tower pitch and the wake velocity deficit decreases for higher wind speeds. The reduction in wake effect is probably because the active pitch control makes the rotor more transparent to the wind.

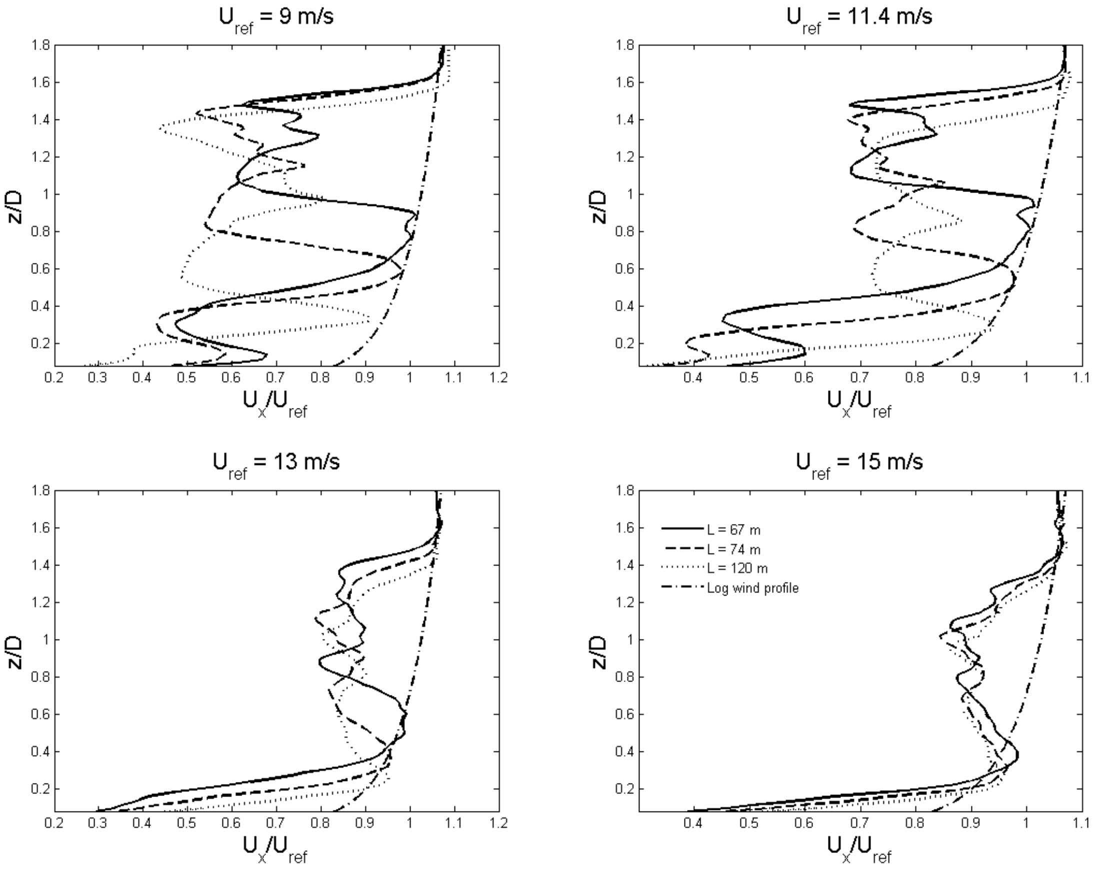

Figure 3.12: Vertical profiles of normalized streamwise velocity at X=7D, Y=0D.

Kidney-shaped wakes have a different effect on downstream turbines than oval wakes. The normalized velocity profiles along the spanwise direction at $7D$ downstream and at the hub height for all twelve cases are shown in Figure 3.13. The kidney shape is not apparent for cases with relatively higher incoming winds or lower tower pitch angles. The kidney-shaped wake causes the side of the downstream rotor in the negative Y direction to experience higher wind speeds than the side in the positive Y direction, which may lead to greater fatigue loading on the blades. Figure 3.14 shows the change of the normalized streamwise velocity along the spanwise direction at $7D$ downstream, and at the height that is $0.5D$ higher than the hub center. Comparing Figure 3.13 and Figure 3.14, the wake velocities are distributed more evenly in the upper half of the turbine rotational plane than at the hub height location.

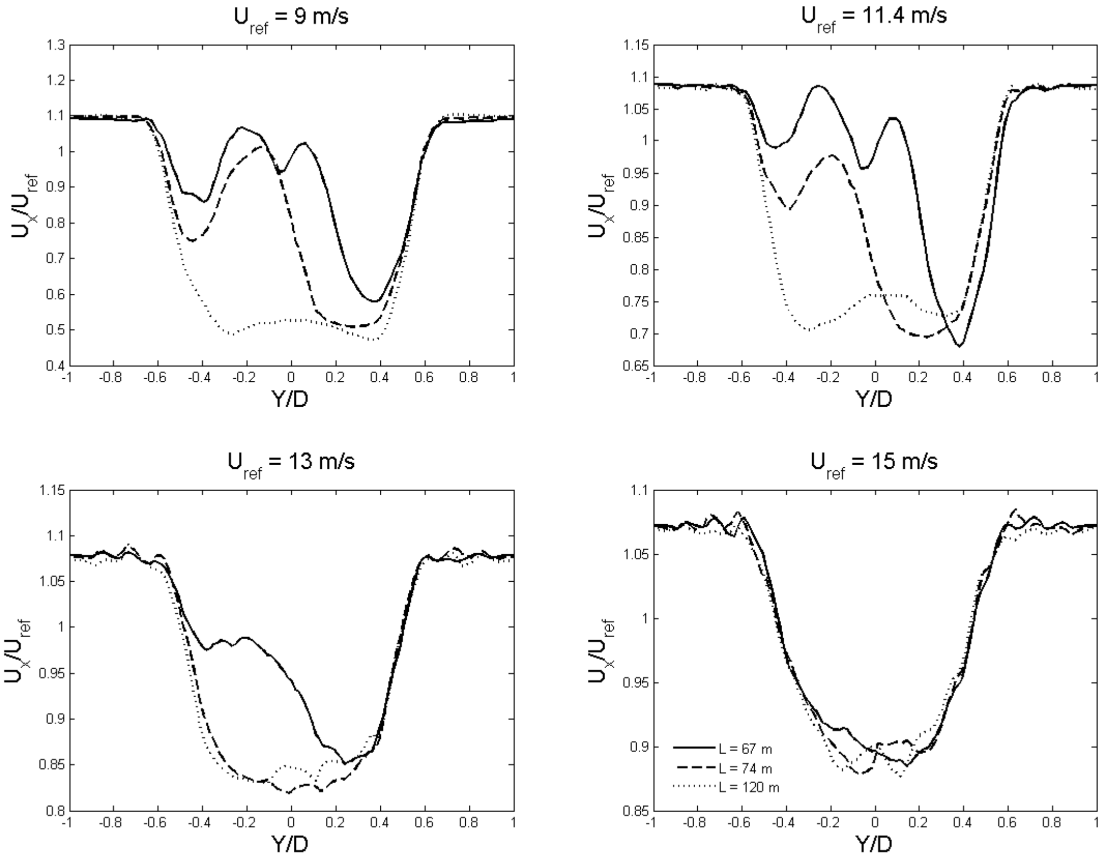

Figure 3.13: Normalized streamwise velocity profile along the spanwise direction at X=7D, Z=Hub Height.

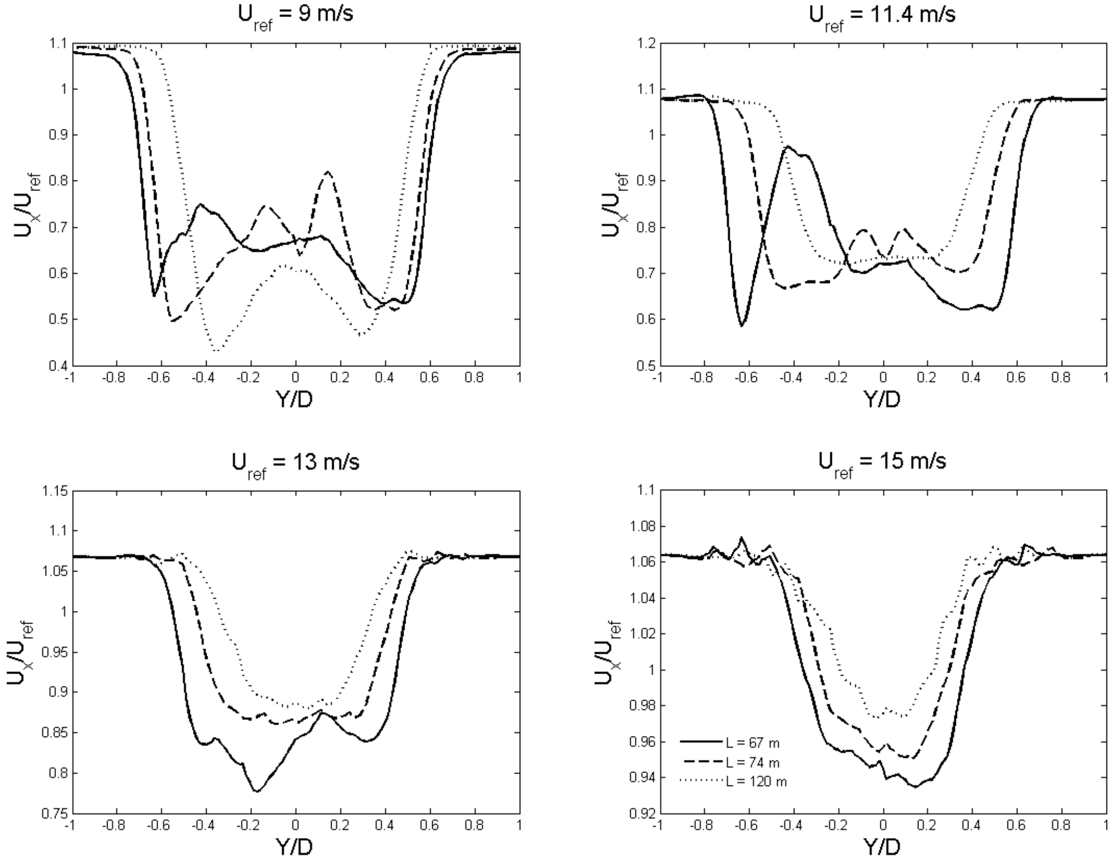

Figure 3.14: Normalized streamwise velocity profile along the spanwise direction at X=7D, Z=153 m.

3.3.5 Application of the Wake Model to Calculate Power Generation and Fatigue Loading

The effectiveness of the new wake model is quantified by comparing the power generation and fatigue loading on a downstream turbine. The wake is predicted using direct CFD simulation, the Jiménez's wake model, the top-hat wake model, and the new model; power and fatigue are predicted using the same time-domain simulation software for all cases (Loose [9] and [31]). The wake velocity predicted by the Jiménez's wake model is computed using Equation 3.2, but the wake center shift distance is taken the same as that of the new wake model computed using CFD to make the results directly comparable because the Jiménez's wake model overestimates the wake center shift as shown in Figure 3.15. The wake velocity predicted by the top-hat wake model is computed using Equation 3.1 with no wake center shift. Two turbine models are used for comparison: the towers with drafts of 74 m and 120 m, which are Cases 5 and 6 in Table 3.1, respectively. The distance between the upstream and downstream turbines is $7D$, and the upstream and downstream turbine models are the same. The free-stream wind speed acting on the upstream turbine is 11 m/s; wind acting on the downstream turbine is predicted by the new wake model, the other two wake models, or direct CFD simulation. The wake of Case 5 develops into a kidney shape while that of Case 6 remains oval (Figure 3.7).

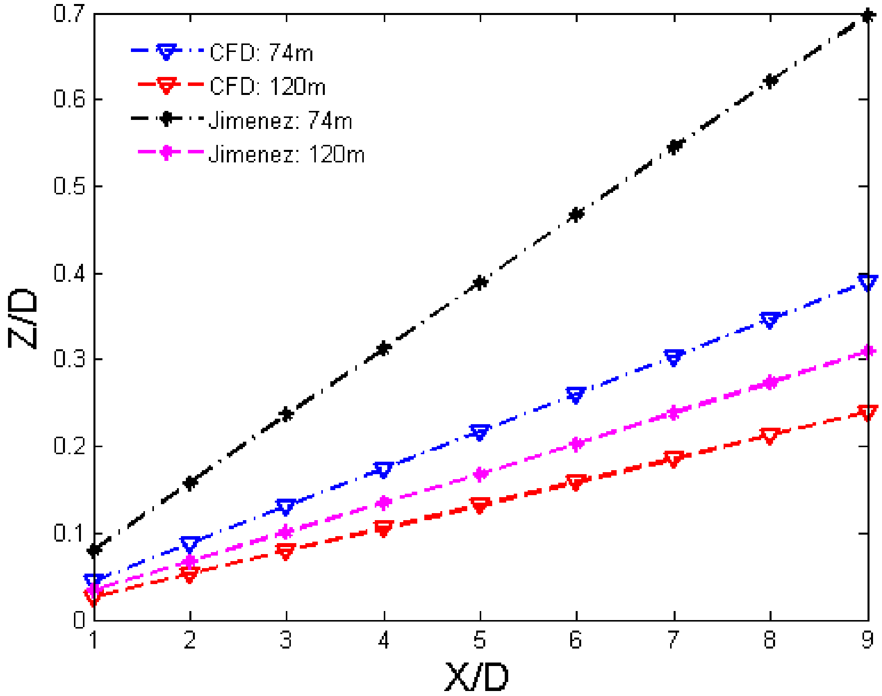

Figure 3.15: Comparison of wake center shift using CFD and Jiménez's wake model.

Figure 3.16 shows the comparison of rotor speeds computed in the wake resulting from each of the four methods for each of the two turbine models at 11 m/s wind. Rotor speeds associated with the new wake model for the turbine model with 74 m draft are slightly greater than those associated with CFD results because the wake velocity deficit computed by the new wake model is less than that computed by CFD (Figure 3.8); rotor speeds associated with the Jiménez's model are slightly less than those associated with CFD results; rotor speeds associated with the top-hat model are much less than those associated with CFD results because there is no wake center shift, such that the rotational plane of the downstream turbine is totally inside the wake. Rotor speeds associated with the new wake model, CFD results, and the Jiménez's model for the turbine model with 120 m draft are very close, with the new wake model showing the best agreement with CFD results. Figure 3.17 shows power output predictions to have similar trends as the rotor speeds. Table 3.3 shows the mean rotor speed and power predicted. The mean rotor speeds computed for the wakes predicted using the new wake model, the Jiménez's model, and the top-hat model are 3.5% greater, 4.3% and 21.0% less than that associated with CFD results for turbine model with 74 m draft, and 1.0%, 2.7%, and 14.3% less than that associated with CFD results for turbine model with 120 m draft. The new wake model yields better estimates of rotor speeds and power outputs than the other two wake models.

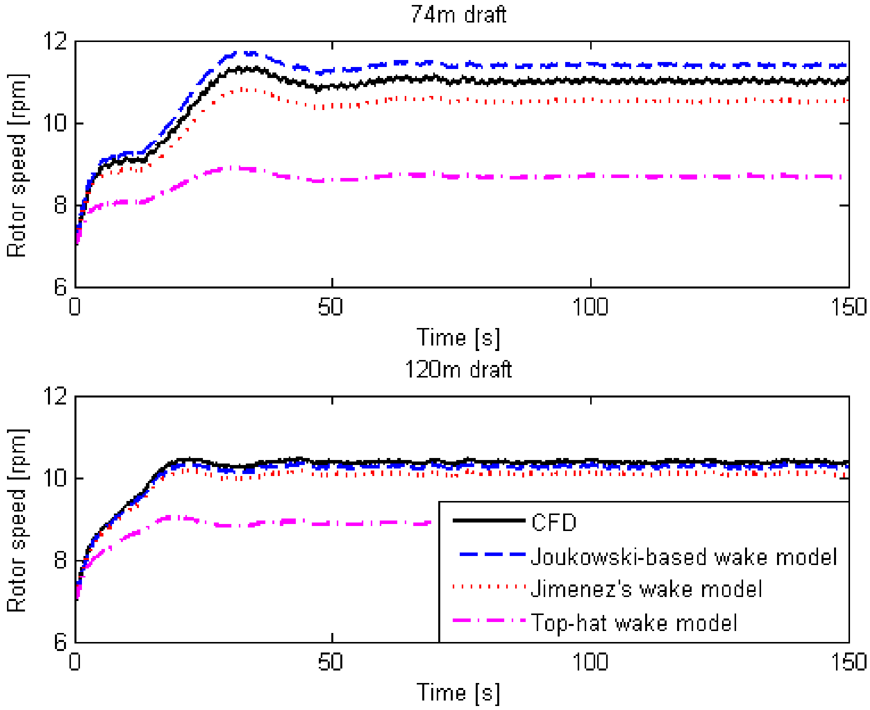

Figure 3.16: Rotor speeds computed in the wake of four methods.

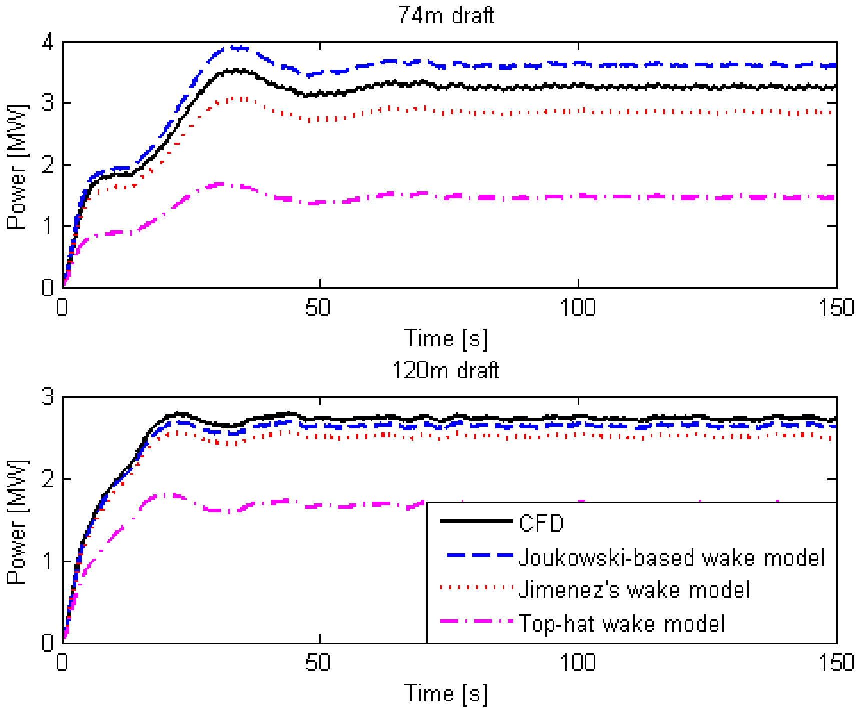

Figure 3.17: Power generation computed in the wake of four methods.

The maximum principal strains of turbine blades are commonly used for fatigue damage. Figure 3.18 presents the maximum principal strains computed using a nonlinear beam model [31]. Strains are presented for a representative location on the tension side of a blade located at one forth of the distance from the blade root to the blade tip. The trends of the strains associated with the new wake model and the CFD simulation are similar for Case 5 (kidney-shaped wake), although the strains computed for the new wake model have a lower amplitude than those computed for the CFD simulation. The strains associated with the Jiménez's and the top-hat models show more sinusoidal trends and have lower means and amplitudes than those associated with the CFD simulation. The trends computed for wakes resulting from each of the four methods are similar for Case 6 (oval wake), but the mean strain associated with the new wake model is greater than that of the CFD wakes and the mean strains of the other two wake models are less than that of the CFD wakes.

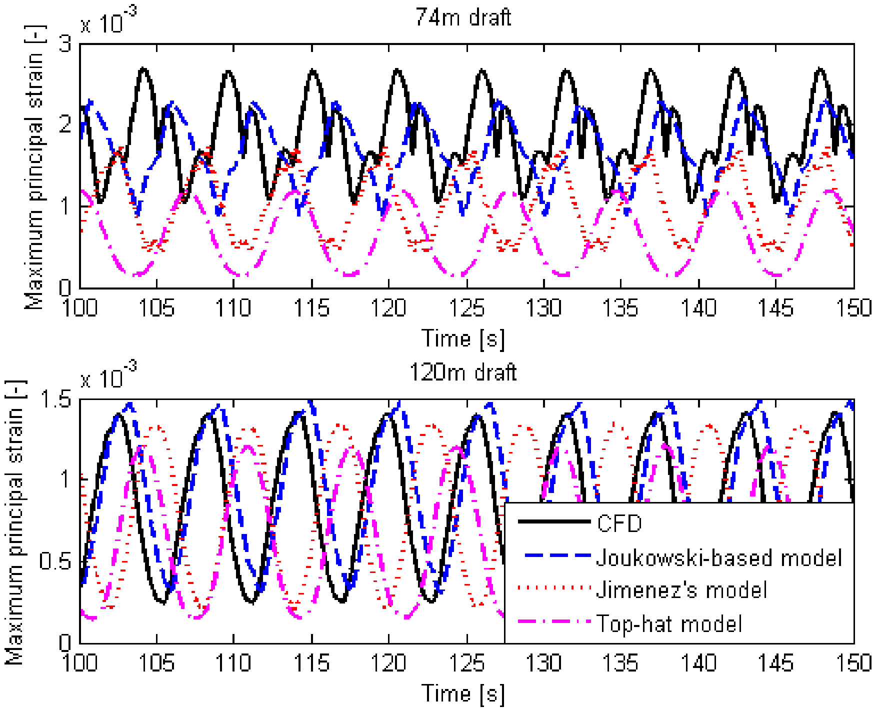

Figure 3.18: Maximum principal strains computed in the wake of four methods.

Table 3.3 shows the 1-day fatigue damage rates computed for turbines operating in wakes predicted using each of the four methods. Fatigue is predicted using the same nonlinear beam solver and the Rainflow counting [46] of the maximum principal strains for application of the Miner's rule [47]. A constant life diagram for the blade material S1 is used for the fatigue analysis [1]. The fatigue damage rate is computed for only one representative wind condition (Figure 3.18). Fatigue damage is predicted for wakes resulting from the new wake model, the Jiménez's model, and the top-hat model. Results for the 74 m floater show an underprediction of about 66%, 87%, and 98%, indicating the Jiménez's and the top-hat models should not be used for fatigue prediction in kidney-shaped wakes. The 120 m case retains an oval wake, and the new wake model and the Jiménez's model perform comparably, with the new wake model slightly overpredicting. Overall, the wakes predicted using the new model are better for estimation of fatigue damage.

Table 3.3: Mean rotor speed, mean power generation, and 1-day fatigue damage

Draft [m]	74			
Method	CFD	Joukowski-based	Jimenez’s	Top-hat
Mean rotor speed [rpm]	10.99	11.38	10.52	8.68
Mean power [MW]	3.25	3.61	2.84	1.46
1-day fatigue damage [-]	2.89e-4	9.87e-5	3.85e-5	5.48e-6
Draft [m]	120			
Method	CFD	Joukowski-based	Jimenez’s	Top-hat
Mean rotor speed [rpm]	10.37	10.26	10.09	8.89
Mean power [MW]	2.73	2.64	2.51	1.67
1-day fatigue damage [-]	1.64e-5	1.91e-5	1.31e-5	6.49e-6

3.4 Conclusions

A new far wake model based on the Joukowski transformation has been developed for a yawed or tilted wind turbine. The model can be used to predict the wake expansion shape and the spatial configuration of the wake velocity deficit. This is the first application of the Joukowski transformation to wind turbine wakes, and the first analytical method to predict a kidney-shaped wake. The derivation follows four main steps: 1) determining the wake shape based on the yaw or tilt angle and the incoming wind speed; 2) calculating the wake velocity deficit according to the Jiménez’s wake model for a series of concentric annuli; 3) mapping each of the circles to a kidney or oval shape using the Joukowski transformation, and then 4) rescaling the wake velocity deficit for the kidney-shaped or oval wake to conform to conservation of momentum. The Joukowski transformation could be applied to any turbine by calibrating parameters λ, η_m, and η_n using CFD simulation results. Representative parameters for a 5-MW turbine have been developed, which are directly applicable to similar turbines.

The new wake model has been verified by direct comparison with wakes predicted using CFD simulation, and found to agree well in both the wake velocity distribution and the expansion shape. Predictions of power generation and fatigue loading have been compared for wakes resulting from CFD simulation and two commonly used wake models. The comparison has demonstrated that the new wake model is effective for power prediction; fatigue performance of downstream turbines is far better than existing models for kidney-shaped wakes, but the new wake model still underpredicts fatigue damage than CFD simulation.

4. MULTIAXIAL FATIGUE ASSESSMENT OF FLOATING OFFSHORE WIND TURBINE BLADES OPERATING ON COMPLIANT FLOATING PLATFORMS

4.1 Introduction and Background

4.1.1 Introduction

Floating offshore wind turbines (FOWT's) are an increasingly viable option for energy harvest in very deep waters. Performance of FOWT's is influenced by the winds, waves, currents, and wakes from other wind turbines in the same wind farm. The design life of a wind turbine is typically 20 years or more, making accurate assessment of fatigue damage an important component of system design. A broad array of floater types have been proposed for offshore wind turbines, including the spar buoy, the tension leg platform, and the barge. The rotational stiffness is an important parameter to the floater design, with floater cost directly correlated with rotational stiffness. A series of truncated spar-type floaters previously have been developed spanning a range of rotational stiffness, seeking to optimize the trade-off between electricity generation and structural cost [10]. The shorter spars have lower rotational stiffness, and therefore allow large rotational motions away from the incoming winds. The differing aerodynamic and gravitational loads on the blades impact fatigue performance. Computing fatigue damage to the blades is challenging because of both the complex aerodynamic and inertial loading and the composite materials used to fabricate the irregular blade shapes.

Blades of FOWT's are subject to complex cyclic non-proportional loading. Extensive documentation exists on fatigue life and ultimate strength testing of composite materials for wind turbine blades [71, 72, 73, 74, 75, 76, 77, 78]. An S-N curve is commonly generated from fatigue testing, which represents the magnitude of a cyclic stress against the cycles to failure in a logarithmic scale. Mean stress effects are important for composite materials with a different S-N curve corresponding to each stress ratio R, where R equals to the minimum stress σ_{min} over the maximum stress σ_{max} of each cycle. A range of R values needs to be used for accurate fatigue life prediction of composite materials. Fatigue life of turbine blades is commonly assessed using constant life diagram (CLD) constructed from fatigue testing of a composite material over a range of mean R values [71, 79, 80, 1]. Stress-based and strain-based methods are both broadly used to compute fatigue life, which method is chosen depending on that the fatigue testing of materials is stress-based or strain-based. Fossum et al. [1] perform fatigue analyses using strain-based methods for an entire blade surface of a 10 MW NOWITECH wind turbine for several different composite materials and recommend hybrid and glass fiber material GG2 for spar caps of blades, and glass fiber material S1 for the shell material. Kulkarni et al. [81] apply a stress-based method to predict fatigue damage for various blade skin materials obtained from SNL/MSU/DOE Composite Material Fatigue Database [78]. Identification of the most likely location of the fatigue failure is difficult because of the extremely complex loading environment acting on the blades of floating wind turbines. Fossum et al. [1] find the location of the maximum fatigue damage to be near one third of the distance from the blade root to the blade tip. Kulkarni et al. [81] find that the joint connecting the hub and the blade is the critical part of fatigue failure.

Accurate calculation of fatigue loading requires quantification of the floater response to the irregular wind-wave loading environment and the inertial, gravitational, and aeroelastic loading on the blades. FAST [8] is a commonly used tool to compute floater response and blade loading. FAST includes a nonlinear beam solver BeamDyn [30], which computes nonlinear beam response to irregular loading, (FAST developed by the National Renewable Energy Lab (NREL)), but detailed stress or strain time-histories at arbitrary locations along a blade are not available.

Many investigators use fatigue at the blade root as a proxy for the fatigue life of a blade, implicitly assuming that the blade root is a representative of the blade response to cyclic loads. Lee et al. [28] calculate the damage-equivalent loads (DELs) at blade roots to estimate fatigue lives of turbines using FAST and BeamDyn. Fatigue damage can be estimated using only the normal stresses or strains caused by bending and axial extension [82, 1]. These methods disregard the important contribution of shear stress or strain to fatigue damage. Philippidis and Vassilopoulos [83] investigate the fatigue life of composite glass/polyester laminates from both theoretical and experimental results and conclude that neglecting shear stresses overestimates fatigue life. An important conclusion of their work is the recommendation of multiaxial fatigue strength criterion for fatigue analysis of composite materials.

The finite element method (FEM) is commonly used to compute multiaxial stress or strain of turbine blades. The resulting multiaxial stress or strain case is then reduced to an equivalent uniaxial case for multiaxial fatigue analysis. Grujicic et al. [84] use FEM to calculate von Mises equivalent stresses for fatigue-life prediction for wind turbine blades. Caous et al. [85] apply FEM to study multiaxial stress states of composite materials for wind turbine blades using the Puck criterion to take into account shear stress influence. Castelos and Balzani [86] study both the ultimate strength and fatigue life prediction of the trailing edge bondlines of turbine blades using both the Drucker-Prager equivalent stress and the Tresca equivalent shear stress; they find the fatigue life of bondlines to be on the order of several months, which is much less than the required life of 20 years. Kulkarni et al. [81] compare the fatigue lives predicted by the maximum principal stress and the von Mises stress criteria, and find the fatigue life predicted using the maximum principal stress criterion is shorter than the life predicted using the von Mises stress criterion. The overall conclusion is that predicting fatigue life using only the normal stress or strain neglects the influence from the important shear stress or strain at some locations along a blade. FEM can be used to account for all the stress or strain components at any location along a blade, but fully-coupled analysis of the complete blade-floater system is extremely complicated, time-consuming, and computationally demanding.

The fatigue performance of blades is assessed on three FOWT models with truncated spar-type floaters [10]. The drafts of the three floaters are 67 m, 74 m, and 120 m, respectively. Identical blades, generators, and control systems are assumed to be applicable to each of the three hull designs. The strain-based methods for fatigue analysis are selected because composite materials of blades generally have low strain damage failure under high cyclic loading and the fatigue testing of composite materials is often represented with strain. Turbine blades are modeled as non-linear elastic beams. Strains at any location on a cross section along a blade are derived based on the angular and linear strains at the elastic center of the same cross section. The computed multiaxial strains are reduced to an equivalent uniaxial principal strain and a normal strain. Fatigue performance of three turbine models with both multiaxial and uniaxial fatigue analysis methods are critically compared and the influence from the truncated floaters on the fatigue damage of turbine blades is assessed.

The method of computation of blade non-linear strains and the usage of multiaxial fatigue method are presented in Section 4.2; description of simulation models, environmental loads, and simulation results are presented in Section 4.3, including the comparison of fatigue prediction between the maximum principal strain and the normal strain methods; conclusions are presented in Section 4.4.

4.1.2 Background

FOWT's are subject to time-varying wind and wave loading simultaneously as well as constant gravitational loading. Wave loading on a floating structure induces motions of the floater that impose inertial loading on blades as an acceleration of the hub and also affect the relative motion between the blades and the wind. Strains at a point on a blade result from the combined effects of aerodynamic loading, gravitational loading, and inertial loading. The aerodynamic loading from the incoming wind mainly generates flapwise bending, the frequency of which is dominated by wind shear and turbulence. Gravitational loading on the rotor leads to sinusoidal loading at the rotational frequency, predominantly in edgewise bending. The inertial loading predominantly results from base-excitation of the blade root and includes the centrifugal force in the spanwise direction along the blades. All these kinds of cyclic loading result in multiaxial strain state in the blades, which requires multiaxial fatigue analysis.

Simulation of floater motions and the irregular wind and wave loading for fatigue assessment are introduced in Section 4.1.2.1; the non-linear beam theory used to model turbine blades is briefly introduced in Section 4.1.2.2; methods commonly used to parameterize multiaxial strain to an equivalent uniaxial strain is presented in Section 4.1.2.3; the general fatigue life prediction method is introduced in Section 4.1.2.4.

4.1.2.1 Simulation of FOWT System

The International Electrotechnical Commission (IEC) [87] specifies that the environmental conditions for fatigue analysis of turbine blades must include at least six 10-min stochastic realizations or a continuous 1-hour simulation period for each hub-height mean wind speed and associated sea state. The code further specifies that the wind speed at hub height spans the interval between the cut-in wind speed and the cut-out wind speed in steps of 2 m/s or less. Currents need not be considered in the fatigue assessment.

A multi-body solver, Loose, is applied to compute the translational and rotational motions of FOWT's under the combined wind-waving loading based on the momentum cloud method (MCM), which is fundamentally based on the conservation of momentum [9]; Loose directly applies Newton's second law to set up equations of motion (EOM's) in terms of pitch-roll-yaw sequenced Euler angles, which are solved in the time domain independent of any small-angle assumptions. The pre-existing DISCON control routine [4] has been coupled with Loose [12]. A variable-speed generator-torque controller in DISCON varies the generator torque to maximize output power when the wind speed is lower than the rated speed. A proportional integral blade pitch controller in DISCON varies the pitch angle of each blade to maintain constant rated generator torque when the wind speed is above the rated speed. The instantaneous blade pitch angles found by the controller are passed to AeroDyn [52] to calculate the wind loads on each of the blades.

4.1.2.2 Momentum-based Beam Theory

A turbine blade subject to large angular and translational motions and irregular loading along its length can be treated as an elastic slender beam. The nonlinear momentum-based beam theory (MBBT) [31] can be applied to compute displacements and strains at the elastic centers of cross sections varying along the length of a blade. The theory implicitly assumes small strains and elastic behavior at each cross section. MBBT has been coupled with the in-house code Loose to solve strains of non-linear blades in the numerical simulation.

Coordinate systems used for MBBT are presented in Figure 4.1. An earth-fixed, inertial, Carte-

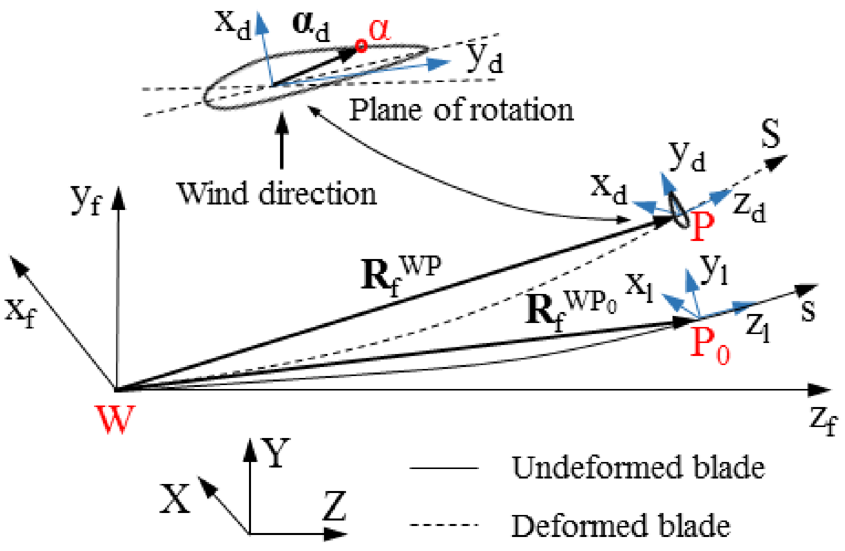

Figure 4.1: Coordinate systems.

sian coordinate system, XYZ, is denoted as global coordinate g. A non-inertial Cartesian coordinate, $x_f y_f z_f$, is fixed to the undeformed blade at the root point W, and is defined as floating coordinate f. Translations and rotations of f relative to g represent global rigid body motions of an undeformed blade. Curvilinear coordinate s is attached to the elastic axis of an undeformed, unstressed blade; another curvilinear coordinate S is similarly attached to the elastic axis of the deformed blade. Two sets of local coordinates are defined at each point along s and S. The non-inertial local undeformed coordinate l is fixed to elastic center P_0, and includes Cartesian coordinates $x_l y_l z_l$ with z_l tangent to the undeformed elastic axis s at P_0, y_l pointing toward the trailing edge and rotating counterclockwise with the twist angle if looking from blade root to blade tip, and x_l pointing toward the suction side and orthogonal with y_l and z_l such that they form a right-handed coordinate system; both x_l and y_l are on the cross-sectional plane. Correspondingly, deformed local coordinate d includes Cartesian coordinates $x_d y_d z_d$, with origin P fixed to the elastic center of the displaced cross-section. Deformed local coordinate d rotates with the cross-section such that x_d and y_d remain on the cross-sectional plane but z_d is not generally tangent to the deformed elastic axis S at P.

Angular strain at an elastic center P_0 of a cross section of a beam representing a blade is computed from the difference between the curvature vector $\boldsymbol{k}_d$ of the deformed coordinate S and $\boldsymbol{k}_l$ of the undeformed coordinate s, which describes the change in direction of a curvilinear coordinate per unit length in different local coordinates [31]:

$$\boldsymbol{\kappa} = \boldsymbol{k}_d - \boldsymbol{k}_l = \text{axial}(\boldsymbol{T}_{dl}\tilde{\boldsymbol{k}}_l\boldsymbol{T}_{ld} + \boldsymbol{T}_{dl}\boldsymbol{T}'_{ld} - \tilde{\boldsymbol{k}}_l) \tag{4.1}$$

in which $\tilde{()}$ denotes the skew-symmetric matrix used to represent cross products as matrix multiplications; $()'$ indicates the spatial derivative with respect to the curvilinear axis; axial$()$ denotes the axial vector computed from a skew-symmetric matrix; $\boldsymbol{T}_{dl}$ is a transformation matrix that transfers a vector from Coordinate d into Coordinate l and $\boldsymbol{T}_{ld}$ does the opposite.

Linear strain at an elastic center P_0 including axial and shear strains and excluding the rigid element rotation is computed from the difference between two differential position vectors: $\boldsymbol{r}'_d$ of deformed coordinate S and $\boldsymbol{r}'_l$ of the undeformed coordinate s:

$$\begin{aligned} \boldsymbol{\gamma} &= \boldsymbol{r}'_d - \boldsymbol{r}'_l \\ &= \boldsymbol{T}_{df}(\boldsymbol{R}_f^{WP})' - \boldsymbol{T}_{lf}(\boldsymbol{R}_f^{WP_0})' \\ &= \boldsymbol{T}_{dl}(\boldsymbol{e}_1 + \tilde{\boldsymbol{k}}_l\boldsymbol{u}_l + \boldsymbol{u}'_l) - \boldsymbol{e}_1 \end{aligned} \tag{4.2}$$

in which $\boldsymbol{T}_{lf}$ is a transformation matrix that transfers a vector in Coordinate l into Coordinate f; $\boldsymbol{R}_f^{WP}$ and $\boldsymbol{R}_f^{WP_0}$ are two position vectors from the origin of Coordinate f to the origins of Coordinates d and l and expressed in Coordinate f; $\boldsymbol{e}_1 = [0, 0, 1]^T$ is a unit vector; $\boldsymbol{u}_l$ is the displacement of the elastic center in Coordinate l.

Both the angular and linear strains at an elastic center of a cross section can be further applied to compute strains at any location on the same cross section.

4.1.2.3 Parameterization of Multiaxial Loading

Computed multiaxial loading on the blades is typically reduced to a single-dimension parameter that is used to predict fatigue performance. Commonly used methods to parameterize multiaxial strain for fatigue analysis include the von Mises effective strain amplitude, the maximum principal strain amplitude, and the maximum shear strain amplitude [88, 44]. The von Mises strain method is commonly applied with finite element simulation. A significant shortcoming of the von Mises approach is that the combined strain is always positive, such that it cannot differentiate between tension and compression of the material. A signed von Mises strain can be applied to overcome this disadvantage. The maximum principal strain method can be expressed as:

$$\triangle\ \epsilon_{eq} = \triangle\epsilon_1 \tag{4.3}$$

in which $\triangle\epsilon_{eq}$ is the equivalent strain range, and $\triangle\epsilon_1$is the range of the maximum principal strain. The maximum principal strain method is more conservative than the von Mises strain method because the amplitude of the first principal strain is generally greater than the von Mises strain. The maximum shear strain method can be expressed as:

$$\frac{\triangle\gamma_{eq}}{2} = \frac{\triangle\epsilon_1 - \triangle\epsilon_3}{2} \tag{4.4}$$

in which $\triangle\epsilon_3$ is the range of the third principal strain. The maximum shear strain method is only suitable for materials and applications in which cracks grow along the maximum shear planes. Time-histories of multiaxial strains of turbine blades computed in the specified environmental conditions can be reduced to an equivalent uniaxial strain time-history using any of these methods.

4.1.2.4 Fatigue Life Prediction

The resulting time-history of an equivalent uniaxial strain can be further reduced to cycles of varying strain reversals using the well-established method of rainflow counting [46], which is commonly used in fatigue analysis. The rainflow-counting method is a peak-counting method that identifies varying peaks and valleys of the time-varying strain data and reduce them to a series of simple strain reversals with different means, amplitudes, and periods. The standard practices for cycle counting in fatigue analysis [89] introduces the detailed procedure of the rainflow-counting method.

Miner's rule can then be used to accumulate all the linear damages caused by the varying strain reversals:

$$D = \sum \frac{n_i}{N_i} \leq D_{cr} \tag{4.5}$$

in which n_i is the number of cycles of different maximum principal strain amplitudes, N_i is the number of cycles to failure, and D_{cr} is the total damage, where summing to 1 indicates failure.

4.2 Methodology

The strain-based methods are applied to both multiaxial and uniaxial fatigue analysis based on the results of fatigue testing of composite materials, and thus accurate computation of strains is crucial to assess fatigue damage on blades.

4.2.1 Strain Calculation at a Point

Strains at any point on a cross section of a 3-dimensional blade can be computed geometrically from the angular and linear strains at the elastic center of that cross section assuming reaction of that plane section is undeformed. The existing MBBT is extended to compute strains at a point on a beam using the position of the point and the same assumptions as in MBBT. The local position of an arbitrary point $\alpha_0(x_l, y_l, s)$ in an undeformed beam is represented by local position vector $\boldsymbol{\alpha}_l = [x_l, y_l, 0]^T$, measured in the local undeformed coordinate l, on the cross-section at s (Figure 4.1). The planar deformation of each cross-section is assumed to be negligibly small such that for the deformed configuration the local position vector $\boldsymbol{\alpha}_d$ of α in the local deformed coordinate d remains the same when α_0 is displaced to α: $\boldsymbol{\alpha}_d = \boldsymbol{\alpha}_l = \boldsymbol{\alpha} = [x_l, y_l, 0]^T$. The strains on cross-sections ($x_d y_d$-planes) accordingly are assumed to be zero: $\epsilon_{x_d x_d} = \epsilon_{y_d y_d} = \gamma_{x_d y_d} = 0$. The resulting strains at point α can be calculated in the same manner as Equation 4.2:

$$\begin{aligned}
[\epsilon_{z_d z_d}, \gamma_{x_d z_d}, \gamma_{y_d z_d}]^T &= \boldsymbol{T}_{df}(\boldsymbol{R}_f^{W\alpha})' - \boldsymbol{T}_{lf}(\boldsymbol{R}_f^{W\alpha_0})' \\
&= \boldsymbol{T}_{dl}(\boldsymbol{e}_1 + \tilde{\boldsymbol{k}}_l \boldsymbol{u}_l + \boldsymbol{u}_l') - \boldsymbol{e}_1 + \boldsymbol{T}_{df}\boldsymbol{T}'_{fd}\boldsymbol{\alpha}_d \\
&\quad - \boldsymbol{T}_{lf}\boldsymbol{T}'_{fl}\boldsymbol{\alpha}_l + \boldsymbol{\alpha}'_d - \boldsymbol{\alpha}'_l \\
&= \boldsymbol{\gamma} + \tilde{\boldsymbol{\kappa}}\boldsymbol{\alpha} \qquad (4.6)
\end{aligned}$$

in which the beam angular strain, $\tilde{\boldsymbol{\kappa}}$, is substituted for $\boldsymbol{T}_{df}\boldsymbol{T}'_{fd} - \boldsymbol{T}_{lf}\boldsymbol{T}'_{fl}$. Equation 4.6 shows that the strain reconstructed from MBBT beam models to be the sum of two parts: the strain related to linear strain at the elastic center, $\boldsymbol{\gamma}$, plus the strain associated with angular deformation, which is computed using angular strain, $\boldsymbol{\kappa}$, and local position vector, $\boldsymbol{\alpha}$.

Principal strains are computed as the three eigenvalues of the strain tensor matrix constructed from strains (Equation 4.6) at any point:

$$\epsilon = \begin{bmatrix} \epsilon_{x_d x_d} & \epsilon_{x_d y_d} & \epsilon_{x_d z_d} \\ \epsilon_{x_d y_d} & \epsilon_{y_d y_d} & \epsilon_{y_d z_d} \\ \epsilon_{x_d z_d} & \epsilon_{y_d z_d} & \epsilon_{z_d z_d} \end{bmatrix} = \begin{bmatrix} \epsilon_{x_d x_d} & \frac{1}{2}\gamma_{x_d y_d} & \frac{1}{2}\gamma_{x_d z_d} \\ \frac{1}{2}\gamma_{y_d x_d} & \epsilon_{y_d y_d} & \frac{1}{2}\gamma_{y_d z_d} \\ \frac{1}{2}\gamma_{z_d x_d} & \frac{1}{2}\gamma_{z_d y_d} & \epsilon_{z_d z_d} \end{bmatrix} \qquad (4.7)$$

The normal strain $\epsilon_{z_d z_d}$ at any point can be computed from Equation 4.6 or equivalently computed from Equation 4.8:

$$\epsilon_{z_d z_d}(x_d, y_d) = -\frac{M_y}{EI_{yy}} x_d + \frac{M_x}{EI_{xx}} y_d + \frac{N_z}{EA} \qquad (4.8)$$

in which M_x, M_y, and N_z are bending moments and normal force at the cross section that passes through the point α; EI_{xx}, EI_{yy}, and EA are stiffnesses about local axes and the axial stiffness.

4.2.2 Computation of Fatigue Damage

One turbine blade is treated as a non-linear elastic beam based on the MBBT method and divided into 23 elements; 23 cross sections are selected to pass through the elastic center of each element; a series of 80 points is selected around the surface of each section; the 23 cross sections times the 80 points result in 1,840 points on the blade for each environmental condition.

Numbers of strain reversals of the maximum principal strain or the normal strain at each point are rainflow-counted for one 10-min time-history at each environmental condition. Miner's rule (Equation 4.5) is used to accumulate the 10-min linear damage acting at each point. The resulting 10-min fatigue damage can be scaled to estimate fatigue damage that would occur if this precise condition were to persist for an extended period of time. The equivalent 1-year fatigue damage for each environmental condition is computed for each of the 1,840 points on the blade to determine the location of fatigue failure.

4.3 Fatigue Analysis

Fatigue damages of blades of three FOWT models are assessed using both the maximum principal strain method and the normal strain method at various environmental conditions.

4.3.1 Numerical Simulation Models

4.3.1.1 FOWT Models

The NREL 5-MW turbine introduced by NREL [4] is an extensively used turbine model for both onshore and offshore studies. The cut-in, rated, and cut-out wind speeds of this turbine are 3 m/s, 11.4 m/s, and 25 m/s respectively, the start-up and rated rotor speeds are 6.9 rpm and 12.1 rpm respectively, the run-pitch value is 0 degrees, and the rated generator torque is 43,094 Nm. The FOWT models using truncated spar-type floaters with drafts of 120 m, 74 m, and 67 m [10] to support the NREL 5-MW turbines are used for fatigue analysis. The model with 120 m draft is selected as the base case because it has the smallest rotational motion and is very similar to the well-known OC3-Hywind numerical model [4]; the model with 74 m draft is the design optimized for power generation vs structural cost; the model with 67 m draft is realistic but not optimal, and is included to investigate the fatigue effects from large overall angles of rotor inclination. Each blade of the 5-MW turbine is divided into 23 elements. Locations of the elastic centers of the cross sections of the 23 elements from the blade root to the blade tip are shown in

Table 4.1. Section 1 is closest to the hub.

Table 4.1: Locations of 23 cross sections

Section number	Location [m]	Section number	Location [m]	Section number	Location [m]
1	1.2	9	18.2	17	50.2
2	3.2	10	22.2	18	54.2
3	5.2	11	26.2	19	56.2
4	7.2	12	30.2	20	57.2
5	9.2	13	34.2	21	59.2
6	11.2	14	38.2	22	60.5
7	13.2	15	42.2	23	61.2
8	15.2	16	46.2		

4.3.1.2 Material of Blade Shells

The NREL 5-MW baseline blades [90] are based on the LM Glasfiber blades used in the DOWEC study [91]. Details of the material properties of both the NREL 5-MW baseline blades and LM Glasfiber blades are not publicly available; however, the beam structural properties and detailed geometry are available [90]. The material S1 is typical of the external shells of utility-scale wind turbine blades and is assumed to be the shell material of the NREL 5-MW baseline blades in this work as was previously assumed by Fossum et al. [1] for a 68 m long blade in a separate fatigue study. Figure 4.2 shows the constant life diagram (CLD) of this material including fatigue data for three strain ratios: -1, 0.1, and 10. The strain ratio $R = -1$ represents fully reserved compressive and tensile loading, $R = 0.1$ represents pure tensile loading, and $R = 10$ represents pure compressive loading. This CLD is taken from the work of Fossum et al. [1]; the test data used to construct this CLD are originally from the study of Sandia National Laboratories [92]. S-N curves used for constructing this CLD are expressed as:

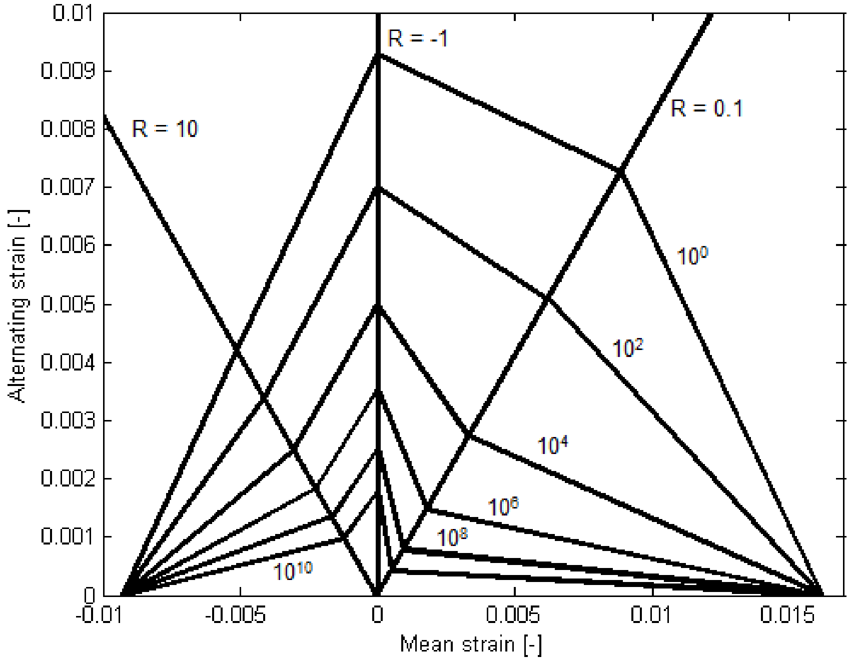

Figure 4.2: CLD of S1 with R=10, R=-1, R=0.1. Reprinted from [1].

$$\epsilon_a = \frac{\epsilon_0 K N_f^{-1/m}}{\gamma_m \gamma_n} \tag{4.9}$$

in which ϵ_a is the strain amplitude, ϵ_0 is the single-cycle static ultimate strain, N_f is the number of cycles to failure, K and m are parameters for fitting the ϵ-N curves shown in Table 4.2, γ_m is the partial material safety factor, and γ_n is the consequence of failure factor. The factors γ_m and γ_n are equal to 1.45 and 1.15, respectively, according to DNV-DS-J102 [93]. The strain ϵ_0 is equal to $UCS/(1-r)$, UCS, and $UTS/(1+r)$ for $R = 10$, $R = -1$, and $R = 0.1$, respectively, in which UCS is the ultimate compressive strain, UTS is the ultimate tensile strain, and $r = (1+R)/(1-R)$.

Table 4.2: Properties of material S1. Reprinted from [1].

UTS [-]	UCS [-]	E [GPa]	K, m (R=10) [-]	K, m (R=-1) [-]	K, m (R=0.1) [-]
0.027	0.015	24.2	1.10, 15.0	1.06, 13.5	1.30, 7.4

4.3.1.3 Environmental Loading

Environmental loading is assumed to be exclusively from winds and waves. Wind speeds vary from 9 to 15 m/s with 1 m/s increments, each of which refers to the mean wind speed of the full-field wind at hub height. Each simulation is performed for 660 seconds to verify longer-term behavior, with the first 60 seconds disregarded to eliminate transients in the vessel motions in accordance with Haid et al. [56].

The logarithmic profile of the vertical distribution of horizontal mean wind speeds is recommended by IEC [87] as:

$$V(z) = V(z_{ref}) \frac{ln(z/z_0)}{ln(z_{ref}/z_0)} \tag{4.10}$$

in which $V(z)$ is the wind speed at height z, z_{ref} is the reference height, which is the hub height and equal to 90 m, z_0 is the roughness length, which is typically taken as 0.0002 m for sea surface in accordance with the European Wind Atlas [36].

The Weibull distribution is used to describe the distribution of wind speeds [35]:

$$P(V) = 1 - exp[-(V/C)^k] \tag{4.11}$$

in which C and k are the scale and shape parameters of the Weibull distribution, and equal to 9.32 m/s and 2.47, as representative of the North sea at $(-20°, 45°)$ [94]. The full Weibull distribution is shown in Figure 4.3 along with bars representing the wind speeds included in the fatigue analysis. Wind speeds greater than 15 m/s are excluded because the relatively low probabilities. Wind speeds less than 9 m/s impose sufficiently small aerodynamic loading that fatigue damage is trivial. All wind speeds for which there are meaningful fatigue damages have been included in the analysis.

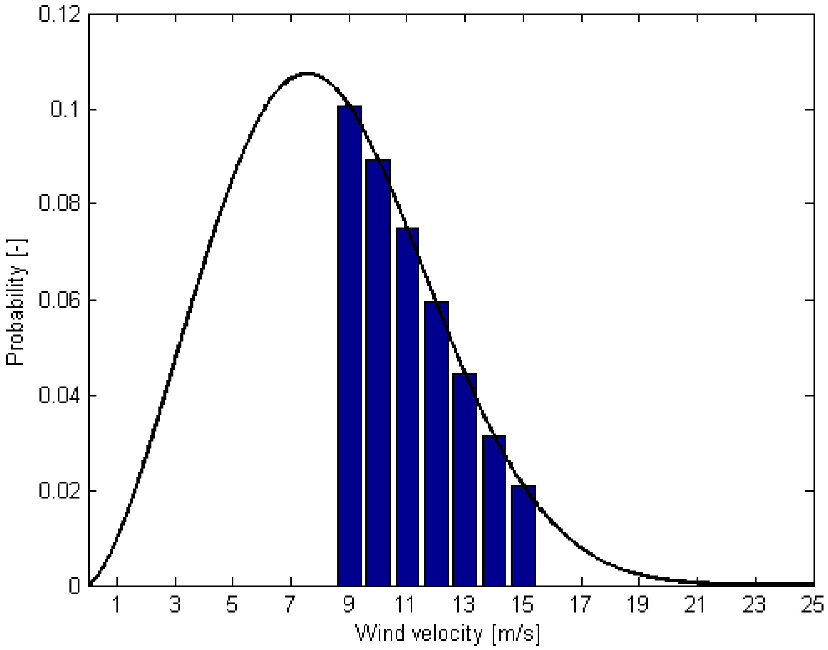

Figure 4.3: Weibull distribution of wind speeds at $(-20°, 45°)$.

Waves are assumed to be collinear with winds. A fully-arisen Pierson-Moskowitz sea state [54] is associated with each wind speed, as specified by IEC design standard for offshore wind turbines [87].

$$T_P = \frac{7.14V_{19.5}}{g} \quad H_s = \frac{0.21V_{19.5}^2}{g} \tag{4.12}$$

where T_P is the peak period; g is the acceleration due to gravity; $V_{19.5}$ is the wind speed at 19.5 m above the sea surface, and H_s is the significant wave height.

Strains of blades of the three FOWT models are computed subject to each of seven simulated environmental conditions shown in Table 4.3.

Table 4.3: Probabilities, peak periods, and significant wave heights associated with hub-height wind speeds

V_{hub} $[m/s]$	Probability [-]	T_p $[s]$	$H_{1/3}$ $[m]$
9.0	0.100	5.18	1.08
10.0	0.089	5.76	1.34
11.0	0.075	6.34	1.62
12.0	0.059	6.91	1.93
13.0	0.045	7.48	2.26
14.0	0.031	8.06	2.63
15.0	0.021	8.63	3.01

4.3.2 Results of Fatigue Analysis

4.3.2.1 Fatigue Damage

Turbine blades are subject to high cyclic loading leading to multiaxial states of strains. Multiaxial fatigue analysis methods are commonly used to reduce the multiaxial case to an equivalent uniaxial case. The maximum principal strain method is popularly applied to assess multiaxial fatigue damages conservatively. The normal strain method is often used for simplification or when shear strains are not available. The maximum principal strain method and the normal strain method are both applied and compared for fatigue assessment of blades of three FOWT's.

Table 4.4 shows the maximum fatigue damages of blade shells computed using both methods for three FOWT's. Parameters D_M and D_N are 1-year fatigue damages at one incoming wind condition computed based on the maximum principal strain method and the normal strain method, respectively. Section number indicates the number of the cross section (Table 4.1) at which the maximum fatigue damage is found; point number indicates the location on that section experiencing maximum fatigue damage.

Table 4.4: Maximum fatigue damage of each FOWT at each wind speed

Wind Speed [m/s]	Draft [m]	Maximum principal strain method			Normal strain method		
		Section number	Point number	D_M [-]	Section number	Point number	D_N [-]
9	67	15	1	0.045	8	60	0.008
9	74	15	1	0.058	8	60	0.017
9	120	15	1	0.054	8	59	0.024
10	67	15	1	0.123	8	57	0.017
10	74	15	1	0.164	8	59	0.029
10	120	15	1	0.135	8	60	0.028
11	67	15	1	0.266	8	57	0.039
11	74	15	1	0.303	8	57	0.036
11	120	15	1	0.229	8	59	0.047
12	67	15	1	0.451	8	57	0.051
12	74	15	1	0.473	8	57	0.081
12	120	15	1	0.306	8	59	0.056
13	67	15	1	0.651	8	57	0.104
13	74	15	1	0.720	8	58	0.135
13	120	15	1	0.277	8	58	0.061
14	67	15	1	0.893	8	57	0.183
14	74	15	1	0.624	8	58	0.105
14	120	15	1	0.285	8	58	0.055
15	67	15	1	0.946	8	56	0.183
15	74	15	1	0.683	8	57	0.069
15	120	15	1	0.295	8	58	0.039

The fatigue analysis method results in the significantly change of the location experiencing maximum fatigue damage, while incoming wind speeds and floater drafts lead to little change of the location. The maximum principal strain method predicts that the location of maximum fatigue damage happens at the trailing edge of section 15 or 16 that is about two thirds of the distance from the blade root to the blade tip, while the normal strain method estimates that the location of maximum fatigue damage happens at the pressure side of section 8 that is about one forth of the distance from the blade root. Figure 4.4 and Figure 4.5 show locations of the maximum fatigue damages computed based on the maximum principal strain method and the normal strain method, respectively.

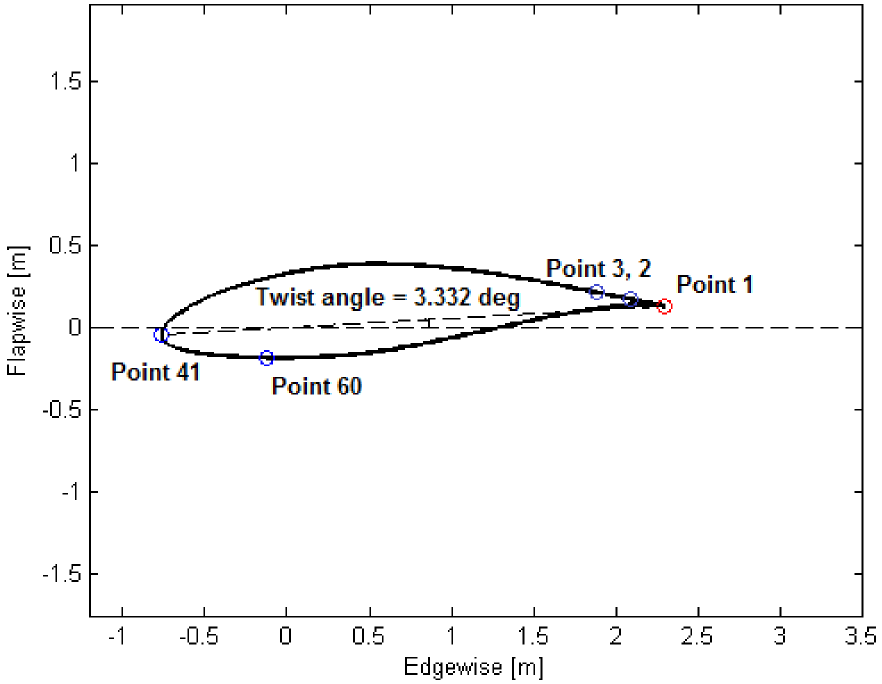

Figure 4.4: Point experiencing maximum fatigue damage at section 15 based on the maximum principal strain method.

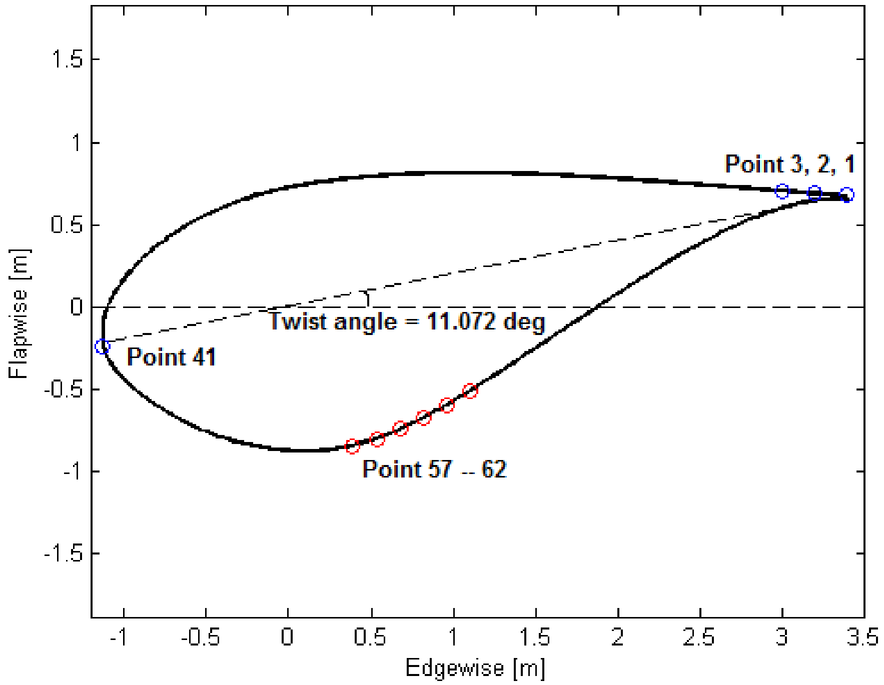

Figure 4.5: Points experiencing maximum fatigue damages at section 8 based on the normal strain method.

The fatigue analysis method also leads to the huge change of the maximum fatigue damage. The maximum principal strain method predicts fatigue damages much greater than those computed using the normal strain method because the normal strain method neglects effects from shear strains (Table 4.4). The normal strain method significantly underestimates the fatigue damage of turbine blades, correspondingly, the maximum principal strain method is more conservative than the normal strain method.

The maximum fatigue damages associated with different incoming winds computed using each of the two strain-based methods are shown in Table 4.4. The trends of fatigue damages computed using the two methods are similar for each of the three FOWT's associated with the incoming winds. Conclusions for the maximum principal strain method are presented in detail. Fatigue damage of the FOWT with 120 m draft increases as the incoming wind speed increases from 9 m/s to 12 m/s, at which speed aerodynamic loads on blades are maximum; fatigue damages associated with wind speeds greater than 12 m/s are less than that associated with wind speed equal to 12 m/s because the active blade pitch control reduces the pitch angle to maintain constant torque and decrease rotor thrust. Fatigue damage of the FOWT with 74 m draft has a similar trend but it increases until the incoming wind speed reaches 13 m/s because the wind component perpendicular to the rotational plane reaches the rated speed of the turbine at a higher incoming wind speed resulting from the larger rotational motion, comparing with the turbine with 120 m floater. Fatigue damage of the FOWT with 67 m draft keeps increasing as the incoming wind speed increases from 9 m/s to 15 m/s because of larger inclining angles comparing with FOWT's with 74 m and 120 m drafts.

Table 4.4 also presents the comparison among the three FOWT's under the same wind condition for the maximum fatigue damage. Fatigue damage of the FOWT with 74 m draft computed using the maximum principal strain method is greater than that of the other two FOWT's under the same incoming wind until the wind speed reaches 13 m/s because of the combined effect from the rotational motions and wind component perpendicular to the rotor disk. The trend of the fatigue damage varying with the truncated floaters computed using the normal strain method is similar to that computed using the maximum principal strain method with exceptions at 9 and 11 m/s winds.

The annual fatigue damage considering the relative frequency of each wind speed is shown in Table 4.5. The maximum principal strain method predicts the maximum fatigue damage locates at the trailing edge of section 15 for all three FOWT models, and the normal strain method predicts that happens at points 57, 58, and 59 of section 8 for FOWT's with 67 m, 74 m, and 120 m drafts, respectively. Parameters D_{MP} and D_{NP} are fatigue damages D_M and D_N multiplying by the relative frequency of each wind speed. Table 4.5 also shows the total fatigue damage of each of the three turbine models computed using each of the two strain-based methods associated with all the presented wind speeds. Total fatigue damages of FOWT's with 67 m and 74 m drafts are almost same predicted using each of the two strain-based methods; total damages of the two FOWT's with shorter floaters are 70% and 30% greater than that of the FOWT with 120 m draft computed using the maximum principal strain method and the normal strain method, respectively. Overall, the truncated floaters with lower stiffness leading to larger rotational motions result in greater fatigue damages.

Table 4.5: Maximum fatigue damage corresponding to frequency of each wind speed

Maximum principal strain method: hot spot at section 15 and point 1						
Wind Speed [m/s]	67 m draft		74 m draft		120 m draft	
	D_M [-]	D_{MP} [-]	D_M [-]	D_{MP} [-]	D_M [-]	D_{MP} [-]
9	0.045	0.0045	0.058	0.0059	0.054	0.0054
10	0.123	0.0110	0.164	0.0147	0.135	0.0121
11	0.266	0.0200	0.303	0.0227	0.229	0.0172
12	0.451	0.0268	0.473	0.0281	0.306	0.0182
13	0.651	0.0290	0.720	0.0320	0.277	0.0123
14	0.893	0.0281	0.624	0.0196	0.285	0.0090
15	0.946	0.0199	0.683	0.0143	0.295	0.0062
Total damage D_{MT}		0.139		0.137		0.080
Normal strain method	section 8 and point 57		section 8 and point 58		section 8 and point 59	
Wind Speed [m/s]	67 m draft		74 m draft		120 m draft	
	D_N [-]	D_{NP} [-]	D_N [-]	D_{NP} [-]	D_N [-]	D_{NP} [-]
9	0.007	0.0007	0.016	0.0016	0.024	0.0024
10	0.017	0.0015	0.028	0.0025	0.028	0.0025
11	0.039	0.0029	0.036	0.0027	0.047	0.0035
12	0.051	0.0030	0.080	0.0047	0.056	0.0033
13	0.104	0.0047	0.135	0.0060	0.057	0.0026
14	0.183	0.0058	0.105	0.0033	0.052	0.0016
15	0.181	0.0038	0.068	0.0014	0.037	0.0008
Total damage D_{NT}		0.022		0.022		0.017

4.3.2.2 *Comparison of Strains*

The normal strain ϵ_{zz} is computed from the normal force and the flapwise and edgewise bending moments resulting from aerodynamic and gravitational loading; the shear strain γ_{xz} is mostly generated from the aerodynamic loading, the main period of which is same as that of the rotor speed; the shear strain γ_{yz} is mainly generated from the gravity of a blade and has the same period as the rotor speed but different phase from γ_{xz} (Figure 4.6 and Figure 4.7). The three strain components of each of the three FOWT's at locations experiencing maximum fatigue damages at sections 8 and 15 at 12 m/s wind are shown in Figure 4.6 and Figure 4.7, respectively. The normal strain ϵ_{zz} is the dominant component at section 8, while the shear strain γ_{xz} is the dominant one at section 15. The normal strain method only has better estimation of fatigue damage at the location that the normal strain is dominant such as section 8; it neglects the huge shear effect resulting from the aerodynamic loading at section 15, which leads to a serious underestimate of the fatigue damage.

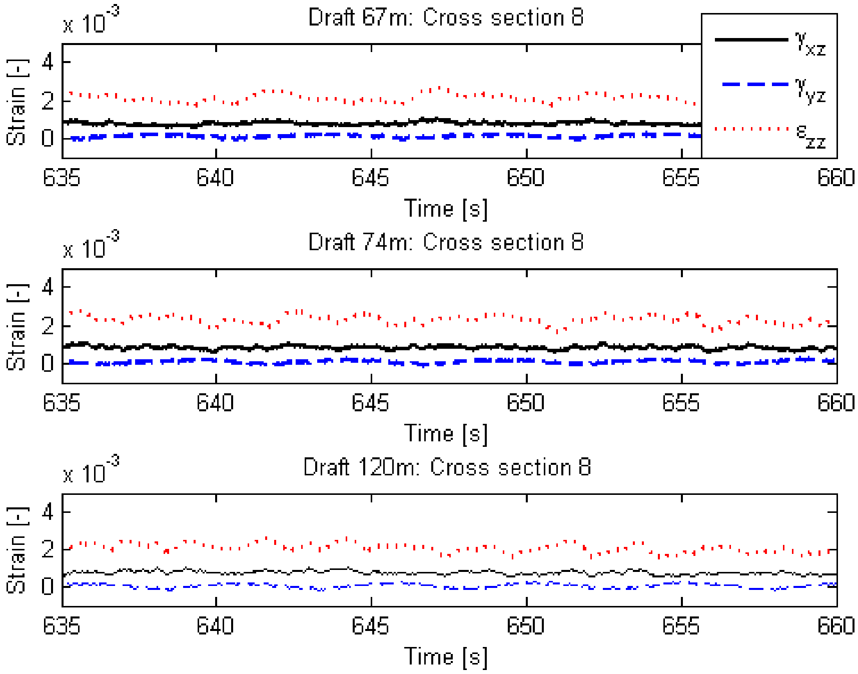

Figure 4.6: Strains at section 8 of the turbine with 74 m draft at 12 m/s wind.

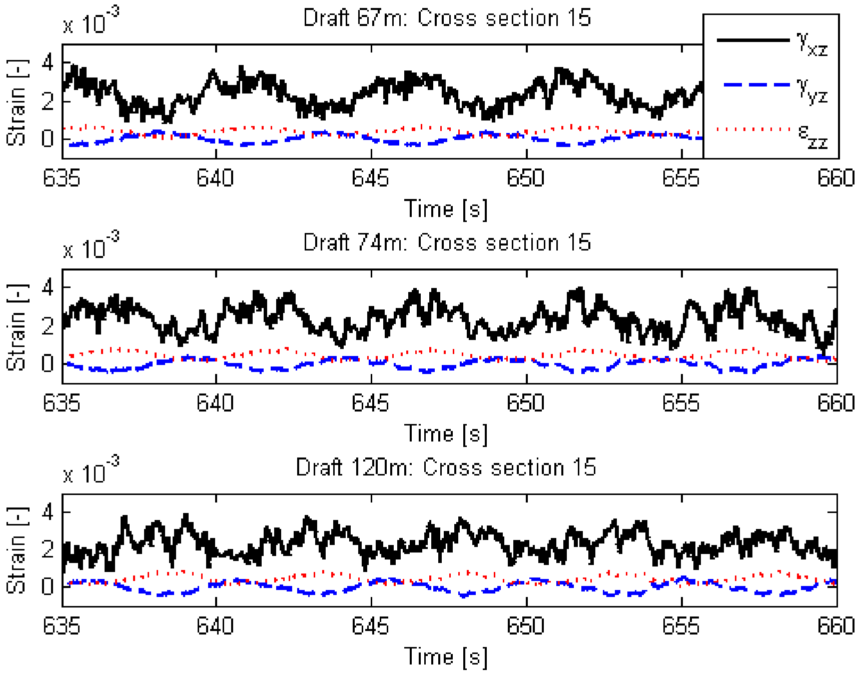

Figure 4.7: Strains at section 15 of the turbine with 74 m draft at 12 m/s wind.

The difference between the maximum principal strain and the normal strain demonstrates the difference of the fatigue damage assessed using each of the two strain-based methods. Figure 4.8 shows the maximum principal and normal strains at locations (Table 4.5) experiencing maximum fatigue damages computed using each of the two methods for the turbine model with 74 m draft at 12 m/s wind. The maximum principal strain at section 8 is overall greater than that at section 15, but amplitudes of different cycles are less. The greater variation of the maximum principal strain in time at section 15 leads to worse fatigue damage comparing with that at section 8 (Table 4.5). The maximum principal strain at section 8 is slightly greater than the normal strain at the same location, which verifies that the normal strain is the dominant component at the location close to the blade root. Both the mean and amplitude of the maximum principal strain at section 15 are much greater than those of the normal strain, which implies that the shear strain is more important than the normal strain at this location.

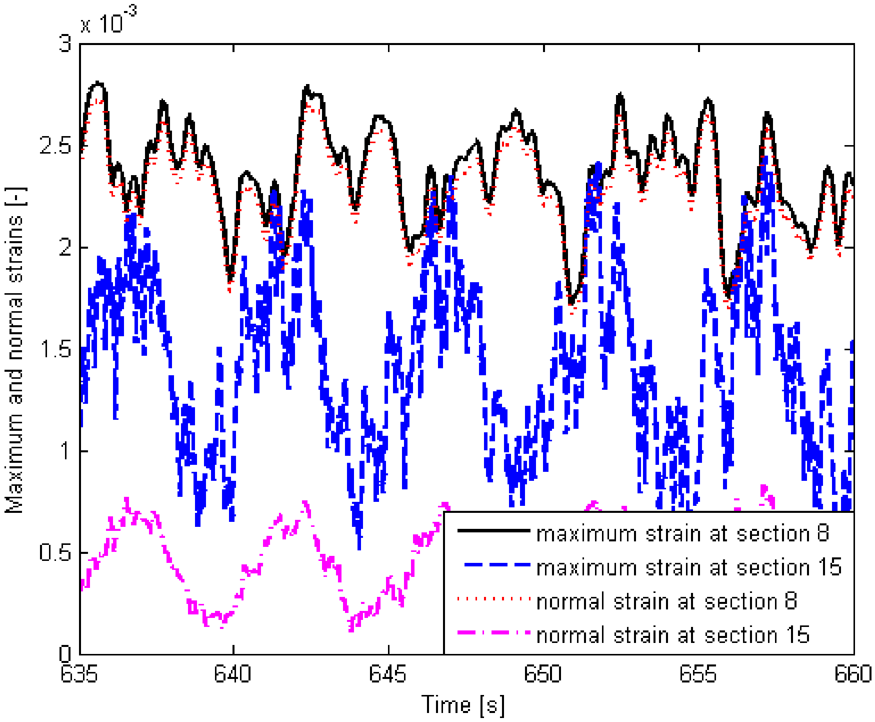

Figure 4.8: Maximum principal and normal strains of the turbine with 74 m draft at 12 m/s wind.

Comparison of the maximum principal strain and the normal strain among the three FOWT models at sections 8 and 15 at 12 m/s wind is shown in Figure 4.9 and Figure 4.10, respectively. The normal strains of each of the three turbines are very close to the maximum principal strains at section 8, and the normal strain of the turbine with 74 m draft is greater than that of the other two turbines, which leads to the greater fatigue damage of this turbine computed using the normal strain method. The mean of the maximum principal strain of the turbine with 74 m draft at section 15 is slightly greater than that of the other two turbines, the amplitude of each cycle of turbines with 74 m and 67 m drafts is slightly greater than that of the turbine with 120 m draft, and the overall trends of the three turbines are similar, which results in the greater fatigue damage of turbines with shorter floaters than the turbine with the longest draft based on the maximum principal strain method.

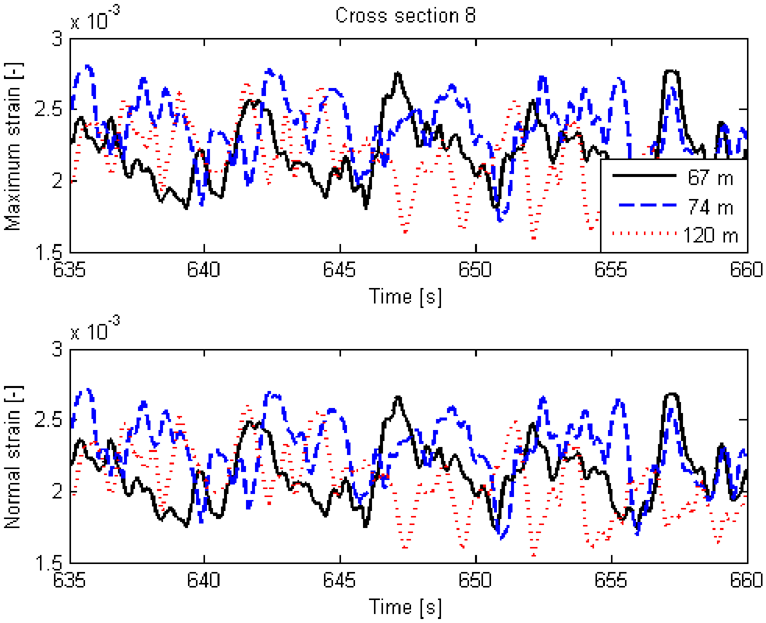

Figure 4.9: Maximum principal and normal strains at section 8 of the turbine with 74 m draft at 12 m/s wind.

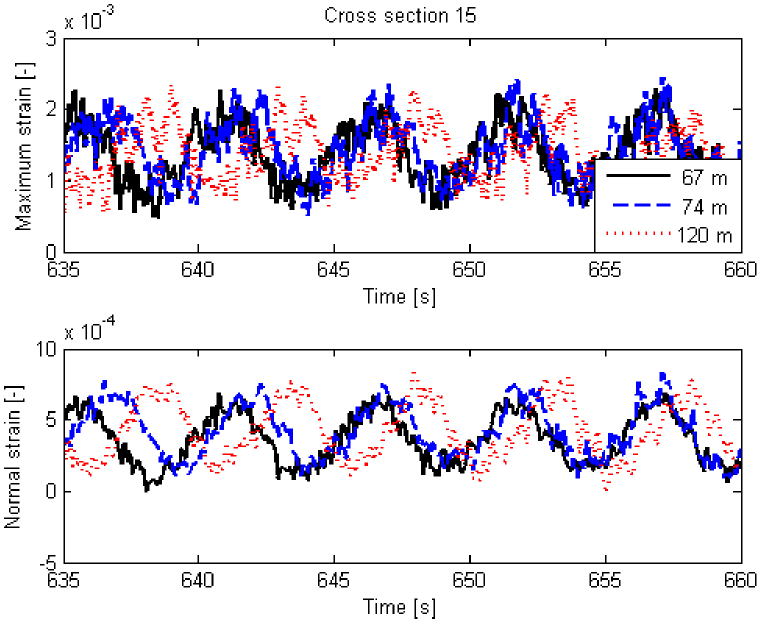

Figure 4.10: Maximum principal and normal strains at section 15 of the turbine with 74 m draft at 12 m/s wind.

4.4 Conclusions

Overall fatigue performance of blade shells of three FOWT's is assessed. The floaters of the three FOWT's are 67 m, 74 m, and 120 m, respectively. The FOWT with 74 m draft has very close total fatigue damage as the FOWT with 67 m draft, and the turbine with 74 m draft has the best trade-off between the structural cost and power generation shown in previous study, such that the FOWT with 74 m draft is better than the one with 67 m draft considering both power harvest and fatigue life of blades. Comparison of maximum fatigue damages associated with the three FOWT's indicates that blades of turbines with more compliant floaters have about 70$\%$ greater fatigue damage than that of the turbine with the stiffest floater, computed using the maximum principal strain method. Materials with better fatigue performance could be applied as blade shells for FOWT's with lower rotational stiffness.

The maximum principal strain method is applied to assess the multiaxial fatigue analysis for blade shells of each of the three FOWT's as well as the normal strain method is used for uniaxial fatigue analysis. The fatigue analysis method leads to changes of both the location experiencing maximum fatigue damage and the value of the fatigue damage. The maximum principal strain method including effects of shear strains shows conservative fatigue results; it predicts that the maximum fatigue damage happens at the trailing edge at about two thirds of the distance from the blade root to the blade tip, where the shear strain component in the flap-wise direction is much greater than the normal strain component. The normal strain method is nonconservative and overestimates fatigue lives of blades; it predicts the location of the maximum fatigue damage located at the tension side of the blade shell at about one fourth of the distance from the blade root. The fatigue damage computed using the maximum principal strain method is much greater than that computed using the normal strain method under the same environmental condition. Comparison between the two strain-based methods indicates that the multiaxial fatigue analysis is absolutely necessary for assessing fatigue lives of turbine blades.

5. ASSESSMENT OF POWER GENERATION AND RESONANCE RESPONSES OF DOWNSTREAM TURBINES

5.1 Introduction

Power generation and structural response of downstream FOWT's are influenced by the wakes from upstream wind turbines. Locations of downstream turbines and wake velocity distributions impact the performance of downstream turbines. Wake velocity deficits may result in less electricity harvest of downstream turbines inside wakes. Wakes having frequencies relating to the natural frequencies of upstream turbines may excite resonant structural responses of downstream FOWT's. This chapter includes assessment of power generation of downstream turbines at different locations and resonant responses between upstream and downstream turbines.

One important goal of layout optimization of a wind farm is to maximize the overall generating efficiency. Both wind directions acting on a FOWF and wake impacts among turbines are necessary to plan the arrangement of a FOWF. Academic work on optimization of layout of FOWT's to include wake effects is not new. Rodrigues et al. [95] develop a layout of a wind farm using movable floating turbines by optimizing the anchoring locations. Yaw control is popularly used to increase power generation by adjusting a turbine's rotational plane to face incoming winds; it is also applied to enhance power generation of downstream turbines without decreasing the energy harvest from the upstream turbine significantly through deflecting the wake flow to reduce impact from wakes on downstream turbines. Schulz et al. and other researchers [96, 97, 98, 99] conclude that yaw control decreases the power output because of the reduced rotational area and effective inflow velocity, but it may also increase the power output of downstream turbines by deflecting the wake. Marathe et al. [100] demonstrate that yaw control motion less than 10 degrees can enhance the overall generating efficiency of a wind farm with only slight decrease of power output of turbines subject to active yaw control. Gebraad et al. and other researchers [101, 102, 27] also verify that yaw control can be used to maximize power generation and optimize turbine layout.

Dynamic responses of FOWT's result from irregular wave and wind loading. Resonant vibration of FOWT's may happen under the coupling effect between winds and waves. Structural resonance should be avoided when designing floaters because excessive resonant response can reduce structural life. Nielsen et al. [103] observe the surge and pitch resonant motions both numerically and experimentally and then apply a blade pitch control algorithm for wind velocities greater than the rated speed to increase damping of tower motions and thereby to avoid large resonant tower motions. Karimirad and Moan [104] conclude that the wave induced responses are decreased by the aerodynamic damping of the rotating rotor through blade pitch control and the resonant response in pitch direction is also reduced through relative motion of the platform; they also find that the resonant responses for FOWT's with catenary mooring lines only occur in lower frequencies and have little effect on the power output. Karimirad [105] demonstrates that large resonance of wind induced motions exist in harsh conditions and both the aerodynamic damping and the hydrodynamic viscous damping decrease resonant response. Pollack et al. [106] also demonstrate that increasing aerodynamic damping suppresses resonant responses of supporting structures of FOWT's.

Numerical simulation models and analysis of simulation results are presented in Section 5.2, including power generation of turbines at different downstream locations and resonant responses between the upstream and downstream turbines; conclusions are presented in Section 5.3.

5.2 Simulation Results

The models in Cases No.2, 3, 8, and 9 described in Section 3.3.1 are used as the upstream FOWT models in this chapter. The same turbine model is used for the upstream turbine and downstream turbines at different locations at one wind speed. Performance of downstream turbines in wakes of a upstream turbine is computed using the in-house simulator Loose. Wind velocities at different downstream locations in the flow field (Figure 3.5) are output from OpenFOAM and taken as incoming winds to downstream turbines. Waves acting on downstream turbines are same as those acting on the upstream turbine; current and surface stretching effect are not considered.

5.2.1 Power Generation

Performance of downstream wind turbines at different locations is assessed. Figure 5.1 shows different locations of downstream wind turbines, in which circles represent centers of downstream wind turbines. Location (0) means a turbine located at $7D$ (D is turbine diameter) downstream distance from the upstream turbine along the x-axis direction; locations (1), (2), and (3) are $0.32D$, $0.63D$, and $0.95D$ from location (0) along the positive y-axis direction; locations (4), (5), and (6) are same distances away from location (0) as locations (1), (2), and (3) but along the negative y-axis direction, respectively; locations (7), (8), and (9) are also same distances away from the x-axis but $9D$ away from the upstream turbine along the x-axis direction.

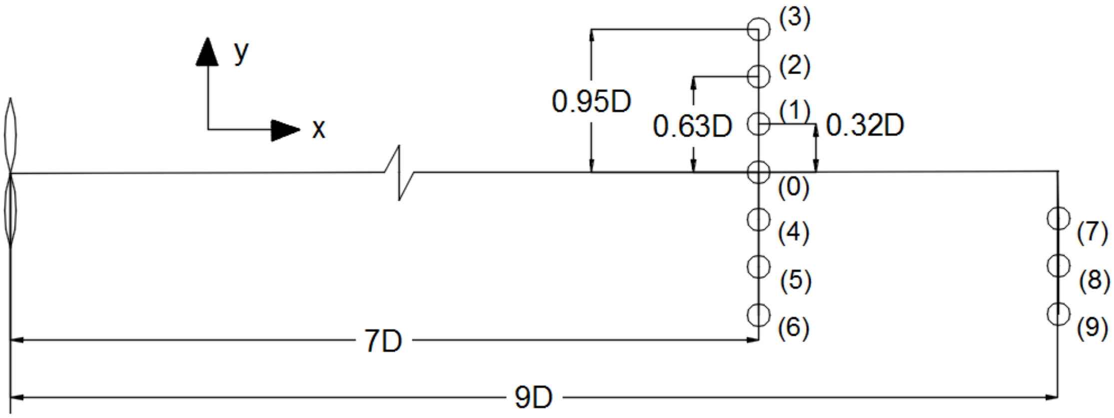

Figure 5.1: Locations of downstream wind turbines.

Figure 5.2 shows platform pitch displacements, rotor speeds, and power generation of the upstream turbine and the downstream turbines located at (1) to (6) (Figure 5.1). Both the upstream FOWT and downstream FOWT's at different locations have 74 m draft, the optimal draft evaluated based on the tradeoff between structural cost and power generation (Chapter 2). The upstream turbine is Case 2 with 11° mean platform pitch angle at 9 m/s wind (Chapter 3). Performances of turbines located at (1), (2), and (3) or (4), (5), and (6) demonstrate that the farther a turbine locates from location (0) along y-axis direction, the better the performance of the turbine is, until the turbine outside of wakes. Performances of turbines at locations (3) and (6) are almost same as that of the upstream turbine because the rotational areas of downstream turbines are mostly outside of the wake from the upstream turbine. Performances of turbines located at (4) and (5) along the negative y-axis direction are better than those of turbines located at (1) and (2) along the positive y-axis direction because the wake coming out from the inclining turbine develops a kidney shape resulting in greater wind speeds acting on turbines located at (4) and (5) than those acting on turbines located at (1) and (2) (Figure 3.7).

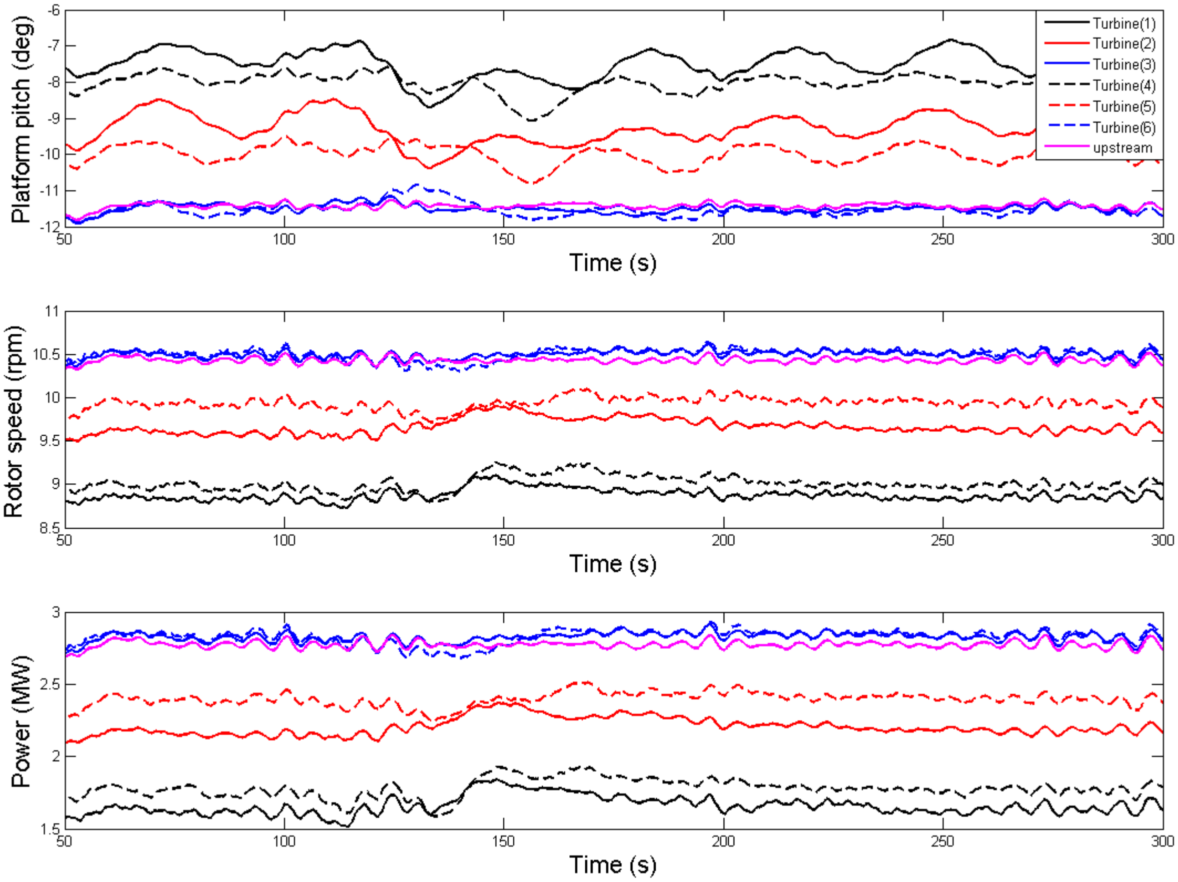

Figure 5.2: Comparison of pitch displacements, rotor speeds, and power output of FOWT's with 74 m draft among turbine locations (1) to (6) at 9 m/s wind.

Figure 5.3 shows platform pitch displacements, rotor speeds, and power generation for the upstream turbines and the downstream turbines located at (4) to (6). Floaters of the FOWT models are 74 m and 120 m long, respectively. The upstream turbines are Cases 2 and 3 in Chapter 3. The wake effects on downstream turbines decrease with increasing turbine distance from location (0); platform pitch displacements are seen to have greater influence on performance of turbines than wakes. Power generation of the turbine with 74 m draft located at (4) is slightly greater than that of the turbine with 120 m draft at the same location because the wake of Case 2 develops a kidney shape and shifts upwards more than Case 3 resulting in greater wind speeds acting on the downstream turbines; power generation of the turbine with 120 m draft located at (5) is slightly greater than that of the turbine with 74 m draft at the same location; power generation of turbines located at (6) have the same trend but greater difference.

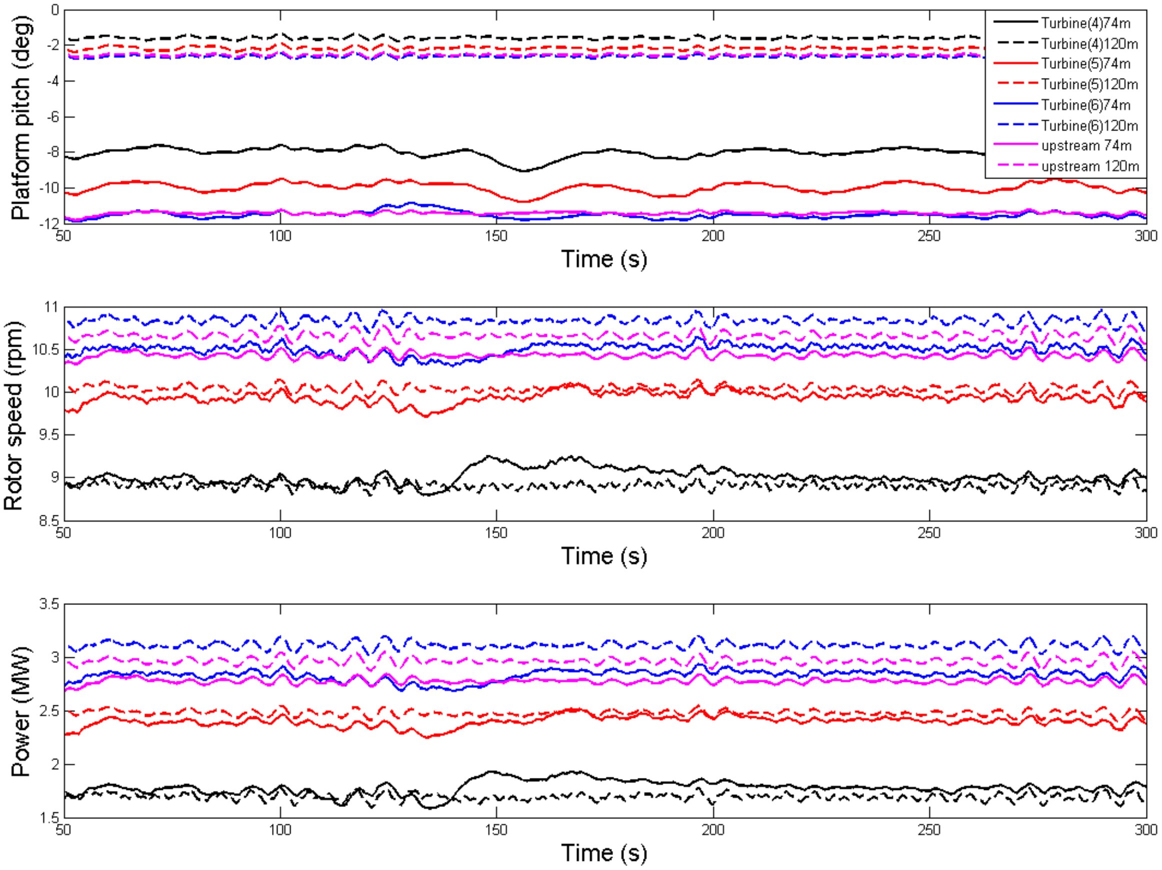

Figure 5.3: Comparison of pitch displacements, rotor speeds, and power output of FOWT's with 74 m and 120 m drafts among turbine locations (4) to (6) at 9 m/s wind.

Figure 5.4 shows platform pitch displacements, rotor speeds, and power generation for the upstream turbines and the downstream turbines located at (4) to (6). Floaters of the FOWT models are still 74 m and 120 m long, respectively. The upstream turbines are Cases 8 and 9 at 13 m/s wind (Chapter 3). Wake velocities at different downstream locations are mostly greater than the rated speed because of the greater free-stream wind speed. Power outputs of all cases are around the rated power and close to each other resulting from the active blade pitch control. The mean of platform pitch displacement of the turbine with a shorter floater is about $12°$ and much greater than that of the turbine with a longer floater.

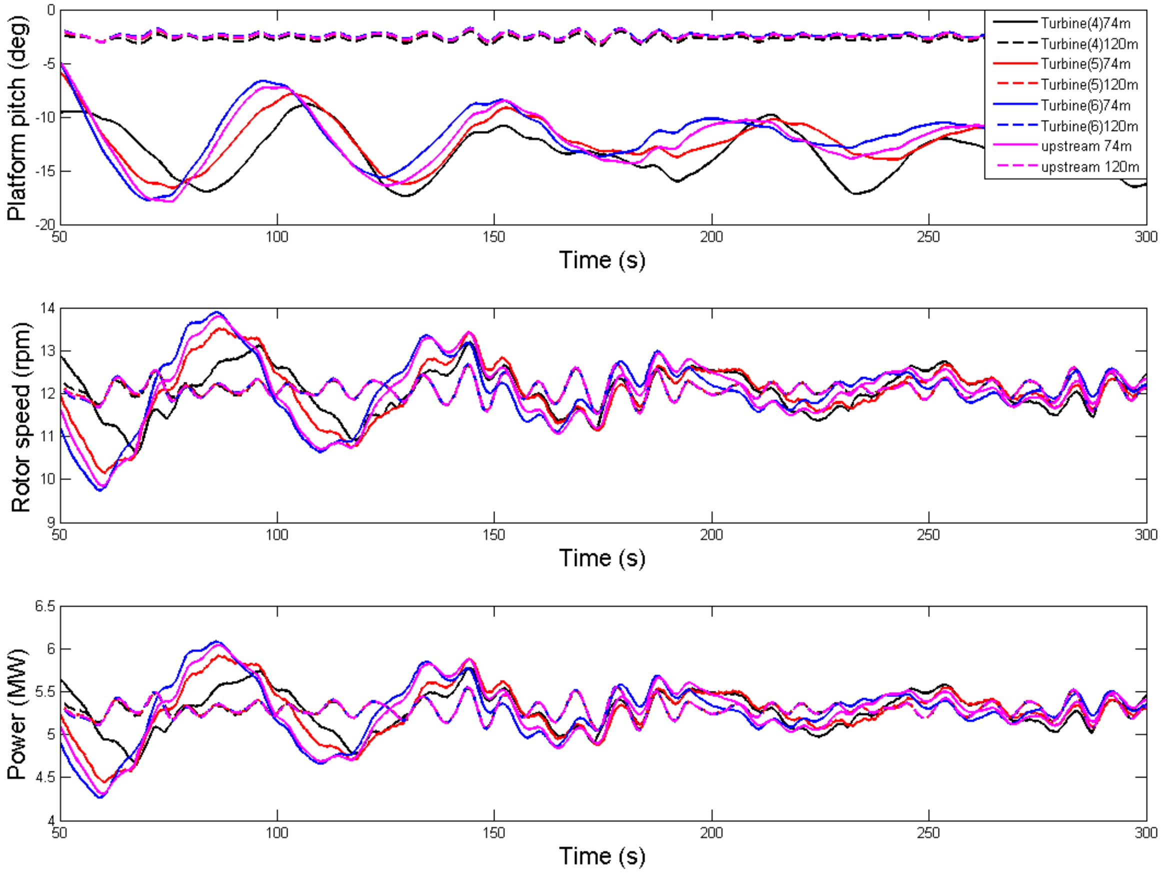

Figure 5.4: Comparison of pitch displacements, rotor speeds, and power output of FOWT's with 74 m and 120 m drafts among turbine locations (4) to (6) at 13 m/s wind.

Figure 5.5 shows platform pitch displacements, rotor speeds, and power generation for the upstream turbines and the downstream turbines located at (4) to (9). The floater of the FOWT model is 74 m long. The upstream turbine is Cases 2 at 9 m/s wind in Chapter 3. Performances of turbines located at (7) to (9) are better than those of turbines located at (4) to (6) because wake effects are less at farther locations.

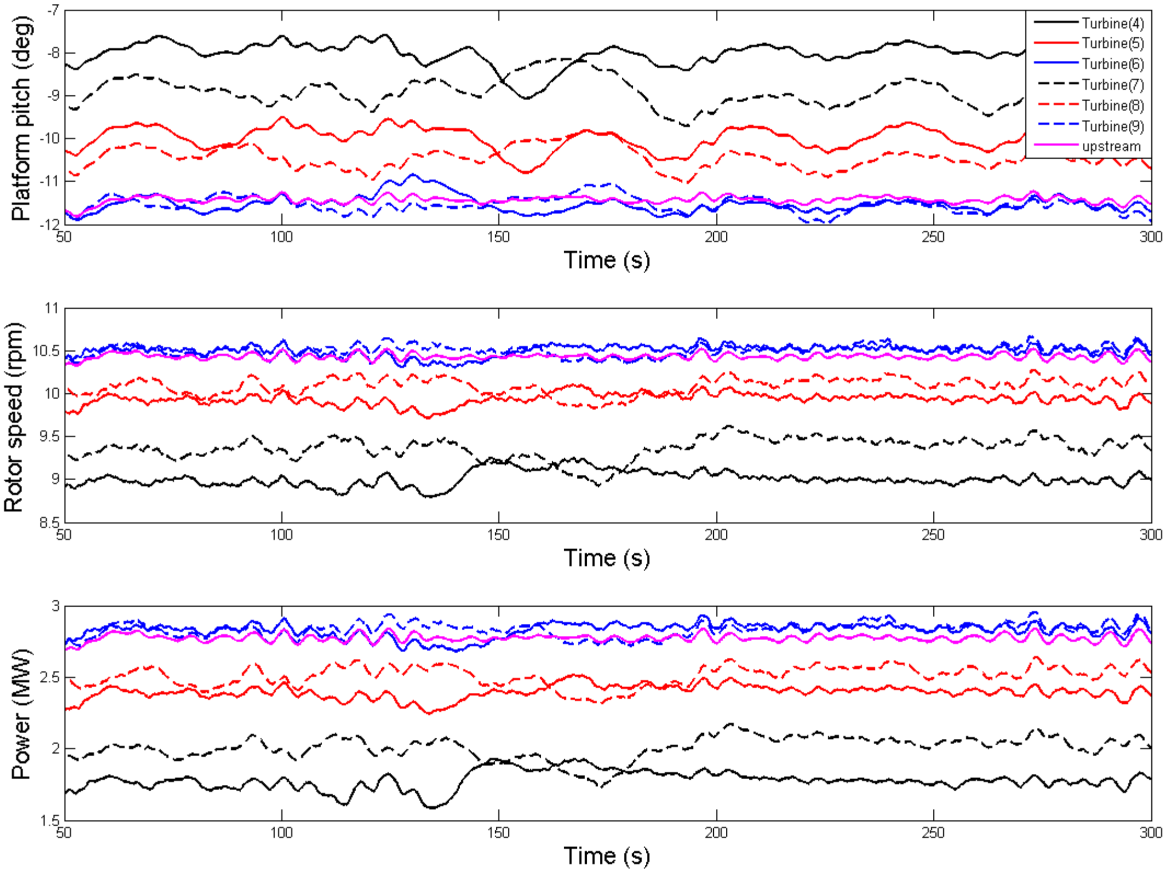

Figure 5.5: Comparison of pitch displacements, rotor speeds, and power output of FOWT's with 74 m draft among turbine locations (4) to (9) at 9 m/s wind.

5.2.2 Resonance of Downstream FOWT's

The towers of FOWT's undergo dynamic motions excited by irregular loadings resulting from turbulent incoming winds and irregular wave loads. Downstream FOWT's are in the wake of upstream turbines. Dynamic disturbances in the wake of the upstream turbine will tend to be at the tower natural period, which may excite an identical downstream turbine at the shared natural period. The potential for this dynamic coupling through the wake is investigated for the optimized turbine with 74 m draft subject to two environmental conditions: the same winds and waves as Cases No.2 (hub-height wind speed is 9 m/s, significant wave height is 1.08 m, and peak period of wave is 5.18 s) and No.8 (hub-height wind speed is 13 m/s, significant wave height is 2.26 m, and peak period of wave is 7.48 s) in Chapter 3. A time-history of displacements of six degrees of freedom of the tower is recorded from Loose and subsequently imposed on the same turbine model in OpenFOAM in order to compute the wake of this turbine including the influence of the turbine dynamic motions, and thus the location of the wind turbine model in OpenFOAM varies according to the time-history of displacements at every time step. The wind condition in OpenFOAM only includes the mean horizontal wind speed varying with altitude, which is generated based on the logarithmic law. The wake flow from this turbine at $7D$ downstream distance in OpenFOAM is recorded and output as the incoming wind of the downstream turbine at this location. The same wave condition applied to the upstream turbine in Loose is applied to the downstream turbine, and then the response of the downstream turbine is computed in Loose and the resonant response is assessed.

Figure 5.6 and Figure 5.7 show displacements of six degrees of freedom of the downstream turbine at 9 m/s and 13 m/s winds, respectively. The resonant structural responses are hard to observe directly, but become apparent on a power spectrum of the displacements. Figure 5.8 and Figure 5.9 show power spectrum of six displacements of the downstream turbine in the wakes of Cases 2 and 8, respectively. The natural frequency of platform pitch is 0.028 Hz (Table 2.1). The resonance peak near the natural frequency of platform pitch is clearly observed in the responses of six displacements of both upstream and downstream wind turbines. The peak values of the downstream turbine are at least twice those of the upstream turbine. The difference in the power spectrum between the upstream and downstream turbines demonstrates that the wake flow acting on the downstream turbine excites resonant responses of the platform.

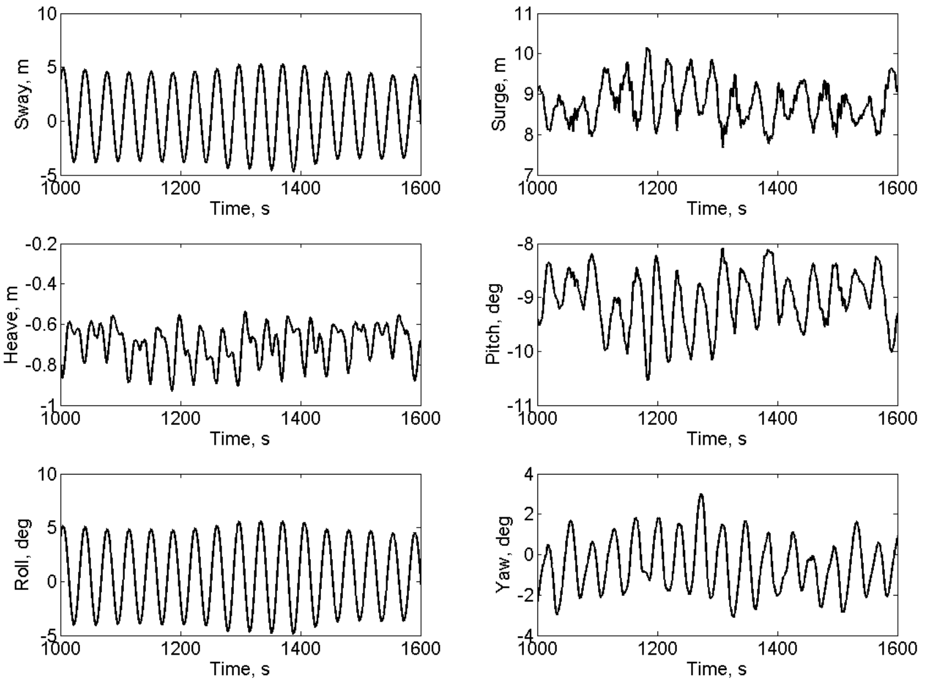

Figure 5.6: Displacements of the downstream turbine with 74 m draft at 9 m/s wind.

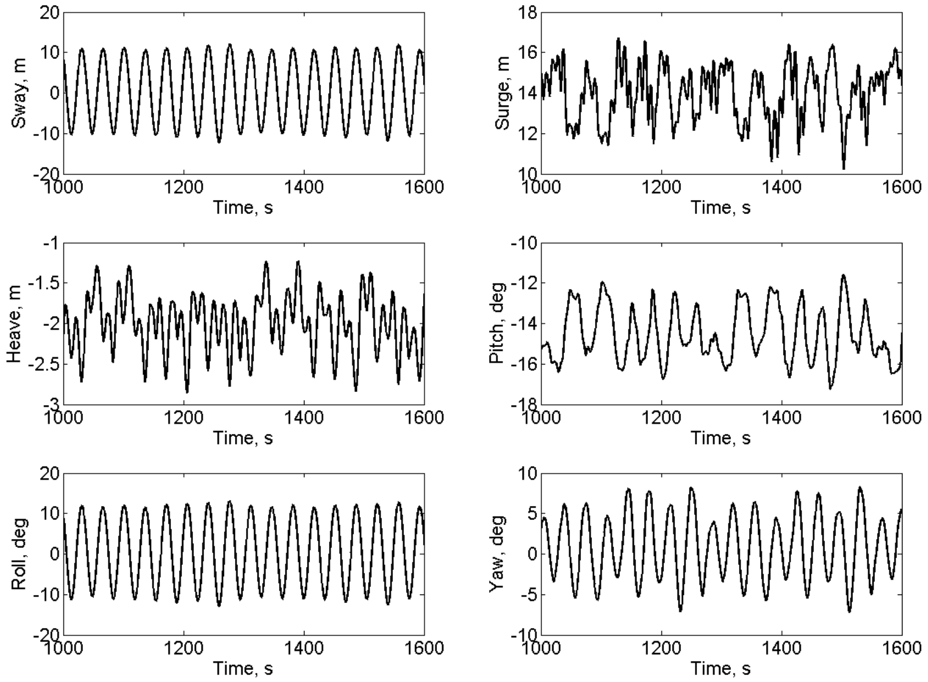

Figure 5.7: Displacements of downstream turbine with 74 m draft at 13 m/s wind.

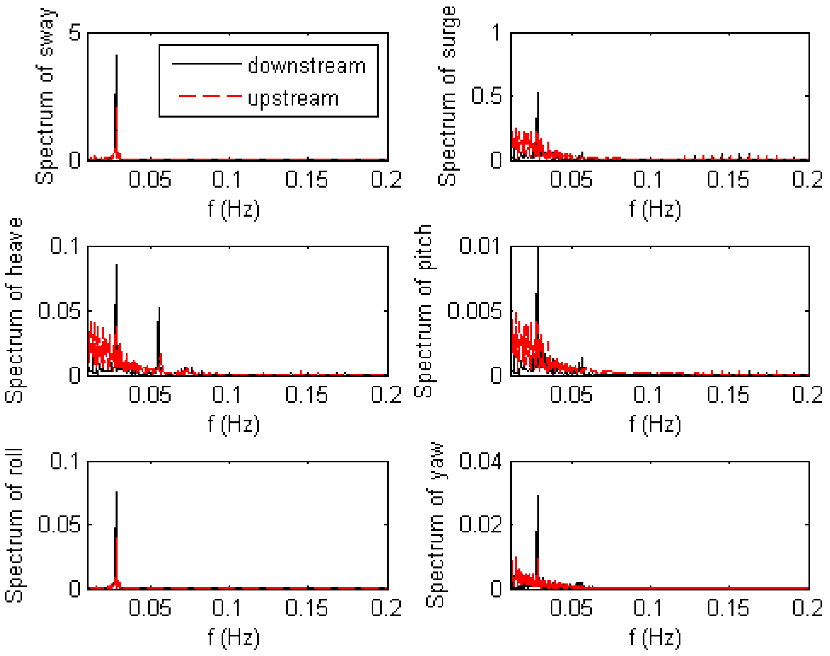

Figure 5.8: Power spectrum of displacements of downstream turbine with draft 74 m under 9 m/s wind.

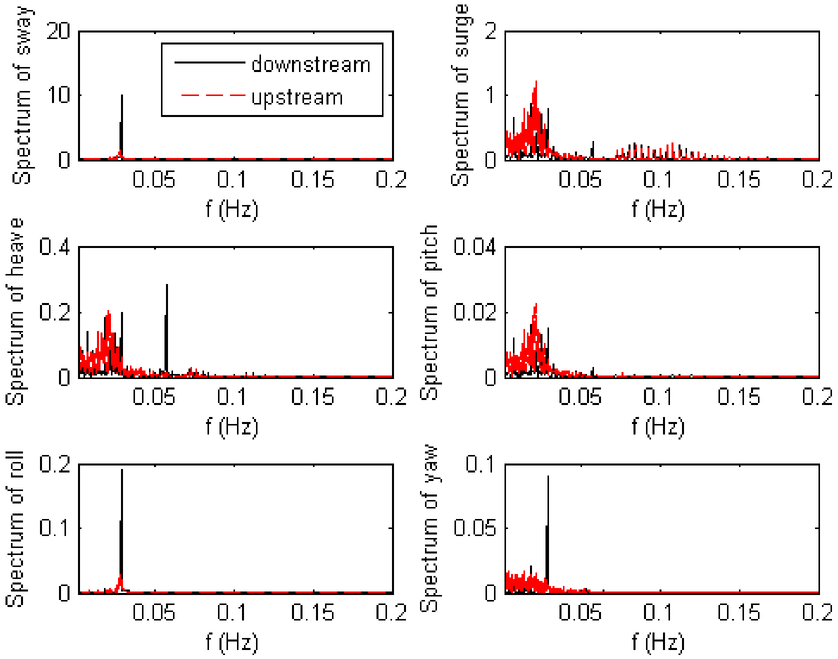

Figure 5.9: Power spectrum of displacements of downstream turbine with draft 74 m under 13 m/s wind.

5.3 Conclusions

Wind turbines are arranged at $7D$ and $9D$ downstream away from the upstream turbine and $0.32D$, $0.63D$, and $0.95D$ offset the x-axis along both positive and negative y-axis directions. Power generation of wind turbines at these downstream locations is assessed. The wake effect on the downstream turbine decreases as the distance between the upstream and downstream turbines increases. Greater power outputs are found for turbines located farther from the upstream turbine both along the x-axis and y-axis directions. The special asymmetric kidney-shaped wake influences the turbine located along the positive y-axis more than that along negative y-axis, and thus performance of downstream turbines located along the negative y-axis is better than that of turbines along positive y-axis. Two methods to enhance the power generation of downstream turbines are to increase the distance between upstream and downstream turbines and to locate the downstream turbine to the negative y-axis direction.

Responses of a FOWT with 74 m draft in the wake of the same turbine model under two incoming wind speeds are assessed. The power spectrum of six displacements of each case shows resonant responses of the downstream turbine around the natural frequency of platform pitch and thus avoidance of structural resonance is necessary to FOWT's. One possible way to avoid resonance is to arrange FOWT's with different floaters in the wake of the upstream turbine such that the resonant frequency of the downstream turbine shifts from that of the upstream turbine. Another possible way is to introduce more hydrodynamic damping to decrease resonant responses.

6. SUMMARY AND CONCLUSIONS

6.1 Summary and Conclusions

Highly compliant designs of FOWT's are developed, assessed, and optimized in this dissertation. This work includes structural design of truncated spar-type floaters, development of individual pitch control for turbine blades, development of wake velocity deficit model, and multiaxial fatigue assessment of turbine blades.

Chapter 2 outlines design of seven new spar-type floaters in conformance with the industrial API rule. The newly designed truncated floaters allow large rotational motions, which violate the small-angle assumption commonly used in the industrial software. The non-linear hydrostatic loads for cylindrical floaters are derived for a pitch-roll-yaw Euler angle sequence without the small-angle limitation. Dynamic structural performance of FOWT's with truncated floaters is evaluated using Loose including the updated hydrostatic loads combined with random hydrodynamic and wind loads. The optimal floater among the seven new designs is 74 m long, which is determined based on the tradeoff between saving structural cost and maximizing power generation. A new individual pitch control method through optimizing the attack angle of each turbine blade is also developed to optimize power performance of FOWT's, but simulation results show that IPC is not an effective way to enhance power generation.

Turbine wakes have great impact on the power output and fatigue life of downstream wind turbines. A new semi-empirical wake model for a yawed or tilted wind turbine is developed based on Joukowski transformation in Chapter 3. The far wake evolves to a kidney shape with the incoming wind component perpendicular to the rotational plane less than the rated speed and the yaw or tilt angle greater than 10 degrees; the wake progresses as an oval for all other conditions. The new wake model assumes the wake has a circular shape at first, then uses the Joukowski transformation to map the circle to a kidney or oval shape, and finally applies conservation of momentum to adjust the wake velocity. This new wake model is applied to assess the power generation and fatigue analysis of downstream turbines and results verify that the new model works well.

Chapter 4 includes assessment of fatigue analysis of three FOWT's with 67 m, 74 m, and 120 m drafts, respectively. Both the maximum principal strain method for multiaxial fatigue analysis and the normal strain method for uniaxial fatigue analysis are applied and compared. The maximum principal strain method estimates that the maximum fatigue damage happens at the trailing tip of the location about two thirds away from the blade root to the blade tip, while the normal strain method predicts that occurs at the tensile side of blade shell at location close to one quarter of the distance from the blade root; the normal strain method significantly underestimates the fatigue damage comparing with the maximum principal strain method. FOWT's with shorter floaters have worse fatigue performance than the turbine with 120 m draft, such that materials of blades of FOWT's with truncated floaters need to have better fatigue performance than that of the turbine with longer draft.

Electricity harvest and resonant responses of downstream FOWT's are analyzed in Chapter 5. Comparison of power generation among turbines at different downstream locations demonstrates that wake effect from upstream turbine is less as the distance from the upstream turbine is farther or as the downstream turbine is offset along the y-axis direction. The resonant effect of the downstream turbine in the wake of the upstream turbine is found through power spectrum of six displacements of the platform. Different floater structures such as floaters with different drafts can be used to avoid structural resonances excited by wakes from upstream turbines.

This work demonstrates that lower stiffness of floaters leads to worse power performance for wind component perpendicular to the rotor disk less than the rated speed of the turbine and has no influence on electricity harvest for greater wind component because of the active blade pitch control. The structural cost saving can compensate for the reduced power output. The designed compliant spar-type floaters are feasible from the perspective of power generation. The large pitch displacement of a floater caused by the lower stiffness results in an upward shift wake from the turbine. The developed wake model has solved the velocity distribution of such case and the upward shift wake results in slightly greater power output from downstream turbines for wake velocity less than the rated speed. FOWT's with compliant floaters have better power performance for both upstream and downstream turbines, however, fatigue performance of blades of such FOWT's is worse than that of FOWT's with stiff floaters. Overall, FOWT's with highly compliant floaters are feasible but an effort to decrease fatigue damage of blades needs to be done.

6.2 Future Work

This work has assessed power and fatigue performance of FOWT's with the newly designed truncated spar-type floaters and developed a new semi-empirical wake model. Further studies of FOWT's include:

1) The feasibility of highly compliant floaters can be expanded to other floater types such as the tension leg platform and the barge. Different types of floaters with lower stiffness may lead to slightly worse electricity harvest but result in saving of cost.

2) The possibility of using individual pitch control to decrease fatigue damage of turbine blades can be studied. IPC improves power generation slightly, but it may be used to optimize fatigue performance of blades by adjusting the blade pitch angle to decrease the variation of aerodynamic loading acting on the blades.

3) Wind turbulences should be considered in computing turbine wakes. The potential effects from turbulences on wakes may include change of the wake expansion shape and the distribution of wake velocities.

4) Fatigue assessment of turbine blades of FOWT's at different locations may be analyzed. Fatigue damage of blades of FOWT's with compliant floaters is worse at greater wind speeds comparing with that with stiff floaters. The change of Weibull distributions caused by the change of locations may lead to the change of total fatigue damage.

5) Possible composite materials with better fatigue performance under multiaxial loading can be applied to blade shells of FOWT's with shorter floaters to guarantee turbine life.

REFERENCES

[1] P. K. Fossum, L. Froyd, and O. G. Dahlhaug, “Design and fatigue performance of large utility-scale wind turbine blades,” *Journal of Solar Energy Engineering*, vol. 135, 2013.

[2] Statoil, “World’s first floating wind farm has started production.” `https://www.statoil.com/en/news/worlds-first-floating-wind-farm-started-production.html`, 2017 (accessed Oct. 25, 2019).

[3] S. Tegen, E. Lantz, M. Hand, B. Maples, A. Smith, and P. Schwabe, “2011 cost of wind energy review,” Tech. Rep. NREL/TP-5000-56266, National Renewable Energy Laboratory, 2013.

[4] J. Jonkman, “Definition of the floating system for phase iv of oc3,” Tech. Rep. NREL/TP-500-47535, National Renewable Energy Laboratory, 2009.

[5] L. Wang and B. Sweetman, “Conceptual design of floating wind turbines with large-amplitude motion,” in *Proceedings of Society of Naval Architects and Marine Engineers*, pp. 58–67, 2011.

[6] I. Fylling and P. A. Berthelsen, “Windopt - an optimization tool for floating support structures for deep water wind turbines,” in *ASME 2011 30th International Conference on Ocean, Offshore and Arctic Engineering*, 2011.

[7] M. Hall, B. Buckham, and C. Crawford, “Evolving offshore wind: A genetic algorithm-based support structure optimization framework for floating wind turbines,” in *OCEANS,MTS/IEEE*, 2013.

[8] J. Jonkman, “Nwtc information portal (fast).” `https://nwtc.nrel.gov/FAST`, 2018(accessed Oct. 25, 2019).

[9] B. Sweetman and L. Wang, "Momentum cloud method for dynamic simulation of rigid body systems," *Journal of Engineering Mechanics*, vol. 140, no. 2, pp. 257–267, 2014.

[10] J. Gao and B. Sweetman, "Design optimization of hull size for spar-based floating offshore wind turbines," *Journal of Ocean Engineering and Marine Energy*, vol. 4, pp. 217–229, 2018.

[11] M. K. AI-Solihat and M. Nahon, "Nonlinear hydrostatic restoring of floating platforms," *Journal of Computational and Nonlinear Dynamics*, vol. 10, no. 4, 2015.

[12] B. Sweetman and B. Wilder, "Numerical simulation of floating offshore wind turbines including aero-elasticity and active blade pitch control," in *Proceedings of Offshore Technology Conference*, 2014.

[13] J. F. Manwell, J. G. McGowan, and A. L. Rogers, *Wind Energy Explained: Theory, Design and Application*. John Wiley and Sons Ltd., 2009.

[14] N. O. Jensen, "A note on wind generator interaction," Tech. Rep. Risø-M-2411, Risø, 1983.

[15] I. Katic, J. Hojstrup, and N. O. Jensen, "A simple model for cluster efficiency," in *Proceedings of European Wind Energy Association Conference and Exhibition*, pp. 407–410, EWEA, 1986.

[16] S. Frandsen, R. Barthelmie, S. Pryor, O. Rathmann, S. Larsen, J. Hjstrup, and M. Thgersen, "Analytical modelling of wind speed deficit in large offshore wind farms," *Wind Energy*, vol. 9, pp. 39–53, 2006.

[17] M. Bastankhah and F. Porté-Agel, "A new analytical model for wind-turbine wakes," *Renewable Energy*, vol. 70, pp. 116–123, 2014.

[18] M. F. Howland, J. Bossuyt, L. A. Martinez-Tossas, J. Meyers, and C. Meneveau, "Wake structure in actuator disk models of wind turbines in yaw under uniform inflow conditions," *Journal of Renewable and Sustainable Energy*, vol. 8, 2016.

[19] M. Bastankhah and F. Porté-Agel, "Experimental and theoretical study of wind turbine wakes in yawed conditions," *J. Fluid Mech*, vol. 806, pp. 506–541, 2016.

[20] G. Qian and T. Ishihara, "A new analyticalwake model for yawed wind turbines," *Energies*, vol. 11, no. 665, pp. 1–24, 2018.

[21] S. Rockel, E. Camp, J. Schmidt, J. Peinke, R. B. Cal, and M. Hölling, "Experimental study on influence of pitch motion on the wake of a floating wind turbine model," *Energies*, vol. 7, no. 8, pp. 1954–1985, 2014.

[22] S. Rockel, J. Peinke, M. Hölling, and R. B. Cal, "Dynamic wake development of a floating wind turbine in free pitch motion subjected to turbulent inflow generated with an active grid," *Renewable Energy*, vol. 112, pp. 1–16, 2017.

[23] S. Xiao and D. Yang, "Large-eddy simulation-based study of effect of swell-induced pitch motion on wake-flow statistics and power extraction of offshorewind turbines," *Energies*, vol. 12, no. 1246, 2019.

[24] H. G. Weller, G. Tabor, H. Jasak, and C. Fureby, "A tensorial approach to computational continuum mechanics using object-oriented techniques," *Computers in Physics*, vol. 12, no. 6, pp. 620–631, 1998.

[25] M. Churchfield and S. Lee, "Nwtc information portal (sowfa)." `https://nwtc.nrel.gov/SOWFA`, 2015 (accessed Oct. 25, 2019).

[26] K. Bhaganagar and M. Debnath, "The effects of mean atmospheric forcings of the stable atmospheric boundary layer on wind turbine wake," *Journal of Renewable and Sustainable Energy*, vol. 7, 2015.

[27] P. M. O. Gebraad, F. W. Teeuwisse, J. W. van Wingerden, P. Fleming, S. D. Ruben, J. R. Marden, and L. Y. Pao, "Wind plant power optimization through yaw control using a parametric model for wake effects-a cfd simulation study," *Wind Energy*, vol. 19, pp. 95–114, 2016.

[28] S. Lee, M. Churchfield, P. Moriarty, J. Jonkman, and J. Michalakes, “Atmospheric and wake turbulence impacts on wind turbine fatigue loading,” Tech. Rep. NREL/CP-5000-53567, National Renewable Energy Laboratory, 2012.

[29] G. Hayman, “Nwtc information portal (mlife).” `https://nwtc.nrel.gov/MLife`, 2015(accessed Oct. 25, 2019).

[30] Q. Wang and M. A. Sprague, “Beamdyn.” `https://nwtc.nrel.gov/BeamDyn`, 2016(accessed Oct. 25, 2019).

[31] S. Tang and B. Sweetman, “A geometrically-exact momentum-based non-linear theory applicable to beams in non-inertial frames,” *International Journal of Non-Linear Mechanics*, vol. 113, pp. 158–170, 2019.

[32] W. J. J. Pierson and L. A. Moskowitz, “Proposed spectral form for fully developed wind seas based on the similarity theory of s. a. kitaigorodskii,” *Journal of Geophysical Research*, vol. 69, pp. 5181–5190, 1964.

[33] K. Hasselmann, T. Barnett, E. Bouws, H. Carlson, D. Cartwright, K. Enke, J. Ewing, H. Gienapp, D. Hasselmann, P. Kruseman, A. Meerburg, P. Mller, D. Olbers, K. Richter, W. Sell, and H. Walden, “Measurements of wind-wave growth and swell decay during the joint north sea wave project (jonswap),” *Ergnzungsheft zur Deutschen Hydrographischen Zeitschrift Reihe*, vol. A(8), 1973.

[34] A. Monin and A. Obukhov, “Basic laws of turbulent mixing in the surface layer of the atmosphere,” *Tr. Akad. Nauk. SSSR Geophiz. Inst.*, vol. 24, no. 151, pp. 163–187, 1954.

[35] “Wind turbines-part 1: Design requirements,” Tech. Rep. EN 61400-1:2005, International Electrotechnical Commission, 2005.

[36] I. Troen and E. L. Petersen, *European Wind Atlas.* Risø National Laboratory, 1989.

[37] S. Voutsinas, K. Rados, and A. Zervos, “On the analysis of wake effects in wind parks,” *Wind Engineering*, vol. 14, pp. 204–219, 1990.

[38] J. F. Ainslie, “Calculating the flowfield in the wake of wind turbines,” *Journay of Wind Engineering and Industrial Aerodynamics*, vol. 27, pp. 213–224, 1988.

[39] L. P. Chamorro and F. Porté-Agel, “A wind-tunnel investigation of wind-turbine wakes: Boundary-layer turbulence effects,” *Boundary-Layer Meteorol*, vol. 132, pp. 129–149, 2009.

[40] Ángel Jiménez, A. Crespo, and E. Migoya, “Application of a les technique to characterize the wake defl ection of a wind turbine in yaw,” *Wind Energy*, vol. 13, pp. 559–572, 2010.

[41] L. C. Berselli, T. Iliescu, and W. J. Layton, *Mathematics of Large Eddy Simulation of Turbulent Flows*. Springer, 2006.

[42] J. Smagorinsky, “General circulation experiments with the primitive equations,” *Monthly Weather Review*, vol. 91, no. 3, pp. 99–164, 1963.

[43] R. Courant, K. Friedrichs, and H. Lewy, “Über die partiellen differenzengleichungen der mathematischen physik,” *Mathematische Annalen*, vol. 100, pp. 32–74, 1928.

[44] D. F. socie and G. B. Marquis, *Multiaxial fatigue*. Society of Automotive Engineers, Inc, 2000.

[45] H. J. Sutherland, “On the fatigue analysis of wind turbines,” Tech. Rep. SAND99-0089, Sandia National Laboratories, 1999.

[46] S. Downing and D. Socie, “Simple rainflow counting algorithms,” *International Journal of Fatigue*, vol. 4, pp. 31–40, 1982.

[47] M. A. Miner, “Cumulative damage in fatigue,” *Journal of Applied Mechanics*, vol. 12, pp. 149–164, 1945.

[48] “Bulletin on stability design of cylindrical shells,” Tech. Rep. G02U03, Aemrican Petroleum Institue, 2004.

[49] K. A. Stol, W. Zhao, and A. D. Wright, “Individual blade pitch control for the controls advanced research turbine (cart),” *Journal of Solar Energy Engineering*, vol. 128, pp. 498–505, 2006.

[50] E. Mohammadi, R. Fadaeinedjad, and G. Moschopoulos, “Implementation of internal model based control and individual pitch control to reduce fatigue loads and tower vibrations in wind turbines,” *Journal of Sound and Vibration*, vol. 421, pp. 132–152, 2018.

[51] X. H. Zeng and X. P. Shen, “Nonlinear dynamics response of floating circular cylinder with taut tether,” in *Fifteenth Offshore and Polar Engineering Conference*, pp. 218–224, 2005.

[52] P. J. Moriarty and A. C. Hansen, “Aerodyn theory manual,” Tech. Rep. NREL/EL-500-36881, National Renewable Energy Laboratory, 2005.

[53] T. Sarpkaya and M. Isaacson, *Mechanics of Wave Forces on Offshore Structures*. Van Nostrand Reinhold Company, 1981.

[54] L. H. Holthuijsen, *Waves in Oceanic and Coastal Waters*. Cambridge University Press, 2007.

[55] “Wind turbines-part 3: Design requirements for offshore wind turbines,” Tech. Rep. EN 61400-3:2009, International Electrotechnical Commission, 2009.

[56] L. Haid, D. Matha, G. Stewart, M. Lackner, J. Jonkman, and A. Robertson, “Simulation-length requirements in the loads analysis of offshore floating wind turbines,” Tech. Rep. NREL/CP-5000-58153, National Renewable Energy Laboratory, 2013.

[57] Wikipedia, “Gansu wind farm.” `https://en.wikipedia.org/wiki/Gansu_Wind_Farm`, 2019(accessed Oct. 25, 2019).

[58] Wikipedia, “Walney wind farm.” `https://en.wikipedia.org/wiki/Walney_Wind_Farm`, 2019(accessed Oct. 25, 2019).

[59] G. N. Abramovich, *The theory of turbulent jets*. MIT Press, 1963.

[60] P. B. S. Lissaman, “Energy effectiveness of arbitrary arrays of wind turbines,” *J. Energy*, vol. 3, no. 6, pp. 323–328, 1979.

[61] N. G. Mortensen, D. Heathfield, O. Rathmann, and M. Nielsen, "Wind atlas analysis and application program: Wasp 11 help facility," tech. rep., Roskilde : Department of Wind Energy, Technical University of Denmark, 2014.

[62] "Openwind theoretical basis and validation," tech. rep., AWS Truepower, LCC, 2010.

[63] G. Hassan, "Gh windfarmer theory manual," tech. rep., Garrad Hassan and Partners Ltd., 2009.

[64] P. Parkin, R. Holm, and D. Medici, "The application of piv to the wake of a wind turbine in yaw," in *Particle Image Velocimetry*, pp. 155–162, 2001.

[65] R. J. Barthelmie, L. Folkerts, G. C. Larsen, K. Rados, S. C. Pryor, S. T. Frandsen, B. Lange, and G. Schepers, "Comparison of wake model simulations with offshore wind turbine wake profiles measured by sodar," *Journal of Atmospheric and Oceanic Technology*, vol. 23, pp. 888–901, 2006.

[66] R. J. Barthelmie and L. E. Jensen, "Evaluation of wind farm efficiency and wind turbine wakes at the nysted offshore wind farm," *Wind Energy*, vol. 13, pp. 573–586, 2010.

[67] L. M. Tossas and S. Leonardi, "Wind turbine modeling for computational fluid dynamics," Tech. Rep. NREL/SR-5000-55054, National Renewable Energy Laboratory, 2013.

[68] M. J. Churchfield, S. Lee, and P. J. Moriarty, "Adding complex terrain and stable atmospheric condition capability to the openfoam-based flow solver of the simulator for on/offshore wind farm applications (sowfa)," in *ITM Web of Conferences*, 2014.

[69] P. A. Fleming, P. M. Gebraad, S. Lee, J.-W. van Wingerden, K. Johnson, M. Churchfield, J. Michalakes, P. Spalart, and P. Moriarty, "Evaluating techniques for redirecting turbine wakes using sowfa," *Renewable Energy*, vol. 70, pp. 211–218, 2014.

[70] N. E. Joukowsky, "Über die konturen der tragflächen der drachenflieger," *Zeitschrift für Flugtechnik und Motorluftschiffahrt*, vol. 1, pp. 281–284, 1910.

[71] H. J. Sutherland and J. F. Mandell, “Application of the u.s. high cycle fatigue data base to wind turbine blade lifetime predictions,” in *ASME*, 1996.

[72] D. D. Samborsky, P. Agastra, and J. F. Mandell, “Effects of glass fabric and laminate construction on the fatigue of resin infused blade materials,” in *46th AIAA Aerospace Sciences Meeting and Exhibit*, 2008.

[73] J. F. Mandell, D. D. Samborsky, and P. Agastra, “Composite materials fatigue issues in wind turbine blade construction,” in *International SAMPE Symposium and Exhibition*, 2008.

[74] T. D. Ashwill and J. A. Paquette, “Composite materials for innovative wind turbine blades,” in *International SAMPE Symposium and Exhibition*, 2008.

[75] D. D. Samborsky, T. J. Wilson, and J. F. Mandell, “Comparison of tensile fatigue resistance and constant life diagrams for several potential wind turbine blade laminates,” *Journal of Solar Energy Engineering*, vol. 131, no. 1, 2009.

[76] J. F. Mandall, D. D. Samborsky, and D. S. Cairns, “Fatigue of composite materials and substructures for wind turbine blades,” Tech. Rep. SAND2002-0771, Sandia National Laboratories, 2002.

[77] D. D. Samborsky, J. F. Mandell, and D. Miller, “The snl/msu/doe fatigue of composite materials database: Recent trends,” in *Structural Dynamics and Materials Conference*, 2012.

[78] J. F. Mandell and D. D. Samborsky, “Snl/msu/doe composite material fatigue database,” tech. rep., Sandia National Laboratories, 2014.

[79] H. J. Sutherland and J. F. Mandell, “Optimized constant-life diagram for the analysis of fiberglass composites used in wind turbine blades,” *Journal of Solar Energy Engineering*, vol. 127, pp. 563–569, 2005.

[80] H. J. Sutherland and J. F. Mandell, “Optimized goodman diagram for the analysis of fiberglass composites used in wind turbine blades,” in *43rd AIAA Aerospace Sciences Meeting and Exhibit*, 2005.

[81] P. A. Kulkarni, W. Hu, A. S. Dhoble, and P. M. Padole, “Statistical wind prediction and fatigue analysis for horizontal-axis wind turbine composite material blade under dynamic loads,” *Advances in mechanical engineering*, vol. 9, no. 9, pp. 1–26, 2017.

[82] M. O. L. Hansen, *Aerodynamics of Wind Turbines*. Earthscan, 2008.

[83] T. P. Philippidis and A. P. Vassilopoulos, “Complex stress state effect on fatigue life of grp laminates. part ii, theoretical formulation,” *International Journal of Fatigue*, vol. 24, pp. 825–830, 2002.

[84] M. Grujicic, G. Arakere, E. Subramanian, V. Sellappan, A. Vallejo, and M. Ozen, “Structural-response analysis, fatigue-life prediction, and material selection for 1 mw horizontal-axis wind-turbine blades,” *Journal of Materials Engineering and Performance*, vol. 19, no. 6, pp. 790–801, 2010.

[85] D. Caous, C. Bois, J.-C. Wahl, T. Palin-Luc, and J. Valette, “Analysis of multiaxial cyclic stress state in a wind turbine blade,” in *20th International Conference on Composite Materials*, 2015.

[86] P. N. Castelos and C. Balzani, “On the impact of multi-axial stress states on trailing edge bondlines in wind turbine rotor blades,” in *Journal of Physics: Conference Series*, 2016.

[87] “Wind turbines-part 3: Design requirements for offshore wind turbines,” Tech. Rep. IEC 61400-3, International Electrotechnical Commission, 2009.

[88] V. M. Radhakrishnan, “Multiaxial fatigue - an overview,” *Sadhana*, vol. 20, pp. 103–122, 1995.

[89] “Standard practices for cycle counting in fatigue analysis,” Tech. Rep. E1049-85, ASTM, 2017.

[90] J. Jonkman, S. Butterfield, W. Musial, and G. Scott, “Definition of a 5-mw reference wind turbine for offshore system development,” Tech. Rep. NREL/EL-500-38060, National Renewable Energy Laboratory, 2009.

[91] C. Lindenburg, “Aeroelastic modelling of the lmh64-5 blade,” Tech. Rep. DOWEC-02-KL-083/0, DOWEC, 2002.

[92] D. A. Griffin, “Blade system design studies volume 1: Composite technologies for large wind turbine blades,” Tech. Rep. SAND-1879, Sandia National Laboratories, 2002.

[93] “Design and manufacture of wind turbine blades, offshore and onshore wind turbines,” Tech. Rep. DNV-DS-J102, DET NORSKE VERITAS, 2010.

[94] W. Mao and I. Rychlik, “Estimation of weibull distribution for wind speeds along ship routes,” *Proceedings of the Institution of Mechanical Engineers, Part M: Journal of Engineering for the Maritime Environment*, vol. 231, 2016.

[95] S. Rodrigues, R. T. Pinto, M. Soleimanzadeh, P. A. Bosman, and P. Bauer, “Wake losses optimization of offshore wind farms with moveable floating wind turbines,” *Energy Conversion and Management*, vol. 89, pp. 933–941, 2015.

[96] C. Schulz, P. Letzgus, T. Lutz, and E. Kramer, “Cfd study on the impact of yawed inflow on loads, power and near wake of a generic wind turbine,” *Wind Energy*, vol. 20, pp. 253–268, 2017.

[97] L. Vollmer, G. Steinfeld, D. Heinemann, and M. Kuhn, “Estimating the wake deflection downstream of a wind turbine in different atmospheric stabilities: an les study,” *Wind Energy Science*, vol. 1, pp. 129–141, 2016.

[98] Y. Uemura, Y. Tanabe, H. Mamori, N. Fukushima, and M. Yamamoto, “Wake deflection in long distance from a yawed wind turbine,” *Journal of Energy Resources Technology*, vol. 139, 2017.

[99] M. T. van Dijk, J.-W. van Wingerden, T. Ashuri, and Y. Li, “Wind farm multi-objective wake redirection for optimizing power production and loads,” *Energy*, vol. 121, pp. 561–569, 2017.

[100] N. Marathe, A. Swift, B. Hirth, R. Walker, and J. Schroeder, “Characterizing power performance and wake of a wind turbine under yaw and blade pitch,” *Wind Energy*, vol. 19, pp. 963–978, 2016.

[101] P. Gebraad, J. J. Thomas, A. Ning, P. Fleming, and K. Dykes, “Maximization of the annual energy production of wind power plants by optimization of layout and yaw-based wake control,” *Wind Energy*, vol. 20, pp. 97–107, 2017.

[102] P. A. Fleming, A. Ning, P. M. O. Gebraad, and K. Dykes, “Wind plant system engineering through optimization of layout and yaw control,” *Wind Energy*, vol. 19, pp. 329–344, 2016.

[103] F. G. Nielsen, T. D. Hanson, and B. Skaare, “Integrated dynamic analysis of floating offshore wind turbines,” in *25th International Conference on Offshore Mechanics and Arctic Engineering*, 2006.

[104] M. Karimirad and T. Moan, “Effect of aerodynamic and hydrodynamic damping on dynamic response of a spar type floating wind turbine,” in *European Wind Energy Conference and Exhibition 2010*, 2010.

[105] M. Karimirad, “Dynamic response of floating wind turbine,” *Transaction B: Mechanical Engineering*, vol. 17, no. 2, pp. 146–156, 2010.

[106] M. L. Pollack, B. J. Petersen, B. S. Connell, D. S. Greeley, and D. E. Davis, “Resonance avoidance of offshore wind turbines,” in *ASME 2010 International Mechanical Engineering Congress and Exposition*, 2010.

[107] N. M. Ismail, “Wave-current models for design of marine structures,” *J. Waterway, Port, Coastal, Ocean Eng.*, vol. 110, no. 4, pp. 432–447, 1984.

[108] N. E. Huang, D. T. Chen, C. chao Tung, and J. R. Smith, “Interactions between steady nonuniform currents and gravity waves with applications for current measurements,” *Journal of Physical Oceanography*, vol. 2, pp. 420–431, 1972.

[109] T. S. Hedges, K. Anastasiou, and D. Gabriel, “Interaction of random waves and currents,” *J. Waterway, Port, Coastal, Ocean Eng.*, vol. 111, no. 2, pp. 275–288, 1985.

[110] L. Chen and B. Basu, “Fatigue load estimation of a spar-type floating offshore wind turbine considering wave-current interactions,” *International Journal of Fatigue*, vol. 116, pp. 421–428, 2018.

[111] J. Wheeler, “Method for calculating forces produced by irregular waves,” in *Offshore Technology Conference*, pp. 72–82, 1969.

[112] G. Hahn, “Influences of wave stretching on the response of wave-excited offshore platforms,” *Ocean Engineering*, vol. 21, no. 6, pp. 507–517, 1994.

[113] J. Azcona, D. Palacio, X. Munduate, L. González, and T. A. Nygaard, “Impact of mooring lines dynamics on the fatigue and ultimate loads of three offshore floating wind turbines computed with iec 61400-3 guideline,” *Wind Energy*, vol. 20, pp. 797–813, 2017.

APPENDIX A

COEFFICIENTS OF NONLINEAR HYDROSTATIC STIFFNESS MATRIX

The submerged length L_{cf} is:

$$\begin{aligned}
L_{cf} &= \frac{L_c + (r_b)_Z - (T_{s\to I} r_b)_Z - X_3}{cX_4 cX_5} \\
&= [L_c - (sX_4 sX_6 - cX_4 sX_5 cX_6)x_f - (sX_4 cX_6 + cX_4 sX_5 sX_6)y_f - cX_4 cX_5 z_f + z_f - X_3]/cX_4 cX_5
\end{aligned}$$

where $\overline{r_b} = [x_f \quad y_f \quad z_f]'$.

Taking the partial derivatives of L_{cf} with respect to the heave (X_3) and Euler angles (X_4 to X_6):

$$\begin{aligned}
\frac{\partial L_{cf}}{\partial X_3} &= -\frac{1}{cX_4 cX_5} \\
\frac{\partial L_{cf}}{\partial X_4} &= [-sX_6 x_f - cX_6 y_f + sX_4(z_f + L_c - X_3)]/c^2X_4 cX_5 \\
\frac{\partial L_{cf}}{\partial X_5} &= [(c^2X_4 cX_6 - sX_4 cX_4 sX_5 sX_6)x_f + (-c^2X_4 sX_6 - sX_4 cX_4 sX_5 cX_6)y_f \\
&\quad + cX_4 sX_5(z_f + L_c - X_3)]/c^2X_4 c^2X_5 \\
\frac{\partial L_{cf}}{\partial X_6} &= [(-sX_4 cX_6 - cX_4 sX_5 sX_6)x_f + (sX_4 sX_6 - cX_4 sX_5 cX_6)y_f]/cX_4 cX_5
\end{aligned}$$

The vector from the center of the body-fixed CS to the midpoint of the submerged length L_{cf} is:

$$[X_F \quad Y_F \quad Z_F]' = T_{s\to I}\overline{r_{CB}} = T_{s\to I}[x_f \quad y_f \quad z_f + 0.5L_{cf}]'$$

in which

$$\begin{aligned}
X_F &= cX_5 cX_6 x_f - cX_5 sX_6 y_f + sX_5(z_f + 0.5L_{cf}) \\
Y_F &= (cX_4 sX_6 + sX_4 sX_5 cX_6)x_f + (cX_4 cX_6 - sX_4 sX_5 sX_6)y_f - sX_4 cX_5(z_f + 0.5L_{cf}) \\
Z_F &= (sX_4 sX_6 - cX_4 sX_5 cX_6)x_f + (sX_4 cX_6 + cX_4 sX_5 sX_6)y_f + cX_4 cX_5(z_f + 0.5L_{cf})
\end{aligned}$$

The partial derivatives of X_F and Y_F with respect to X_3 and X_4 to X_6:

$$\begin{aligned}
\frac{\partial X_F}{\partial X_3} &= \frac{sX_5}{2}\frac{\partial L_{cf}}{\partial X_3} \\
\frac{\partial X_F}{\partial X_4} &= \frac{sX_5}{2}\frac{\partial L_{cf}}{\partial X_4} \\
\frac{\partial X_F}{\partial X_5} &= -sX_5cX_6x_f + sX_5sX_6y_f + cX_5(z_f + 0.5L_{cf}) + \frac{sX_5}{2}\frac{\partial L_{cf}}{\partial X_5} \\
\frac{\partial X_F}{\partial X_6} &= -cX_5sX_6x_f - cX_5cX_6y_f + \frac{sX_5}{2}\frac{\partial L_{cf}}{\partial X_6} \\
\frac{\partial Y_F}{\partial X_3} &= -\frac{sX_4cX_5}{2}\frac{\partial L_{cf}}{\partial X_3} \\
\frac{\partial Y_F}{\partial X_4} &= (-sX_4sX_6 + cX_4sX_5cX_6)x_f + (-sX_4cX_6 - cX_4sX_5sX_6)y_f - cX_4cX_5(z_f + 0.5L_{cf}) \\
&\quad -\frac{sX_4cX_5}{2}\frac{\partial L_{cf}}{\partial X_4} \\
\frac{\partial Y_F}{\partial X_5} &= sX_4cX_5cX_6x_f - sX_4cX_5sX_6y_f + sX_4sX_5(z_f + 0.5L_{cf}) - \frac{sX_4cX_5}{2}\frac{\partial L_{cf}}{\partial X_5} \\
\frac{\partial Y_F}{\partial X_6} &= (cX_4cX_6 - sX_4sX_5sX_6)x_f + (-cX_4sX_6 - sX_4sX_5cX_6)y_f - \frac{sX_4cX_5}{2}\frac{\partial L_{cf}}{\partial X_6}
\end{aligned}$$

The hydrostatic stiffness matrix coefficients K_{ij} expressed in the inertial coordinate system are derived by substituting these partial derivatives into Equation 2.11.

APPENDIX B

INTERACTION OF WAVES AND CURRENTS AND WAVE STRETCHING

B.1 Mathematical Background

Both the current traveling with wave and the stretching effect due to the sea surface movement are studied for the normal condition and extreme condition in this appendix.

B.1.1 Interaction of Waves and Currents

Waves usually travel on currents so it is worth considering the interaction between waves and currents. The hydrodynamic loads due to waves and currents are computed from the Morison equation, in which the interaction of waves and currents are included in the velocities and accelerations in Equation 2.16. Uniform currents associated with random waves are investigated in this work. The dispersion relationship including the influence from currents is expressed as [107]:

$$(\omega - kU_0)^2 = gk\tanh(kh) \tag{B.1}$$

in which ω is the angular wave frequency, k is the wave number, U_0 is the current velocity, g is the gravitational acceleration, and h is the still water depth. The wave spectrum considering the effect of currents is shown as [108, 109, 110]:

$$S'(\omega) = \frac{4S(\omega)}{\sqrt{1 + 4\omega U_0/g}(1 + \sqrt{1 + 4\omega U_0/g})^2} \tag{B.2}$$

in which $S(\omega)$ is the wave spectrum without current effect. The spectrum considering current effect will become infinite when ω is equal to $-g/4U_0$, which indicates wave breaking occurs. The equilibrium range constraint for breaking effect for deep water is provided as [109, 110]:

$$S'_{ER}(\omega) = \frac{Ag^2}{(\omega - kU_0)^5}\frac{1}{[1 + 2U_0(\omega - kU_0)/g]} \tag{B.3}$$

in which A is a constant value in the range of 0.008-0.015. This equilibrium range of the spectrum needs to be used whenever $S'_{ER}(\omega)$ is less than $S'(\omega)$.

B.1.2 Wheeler Stretching

The stretching effect due to the sea surface movement is taken as a modification to the linear wave theory by Wheeler [111]:

$$z_e = \frac{zh}{\eta + h} \tag{B.4}$$

in which z_e is an effective height, z is the actual height, and η is the vertical displacement at the still water level. The Wheeler stretching method is a commonly used method. Hahn [112] studies wave stretching on responses of offshore platforms using this Wheeler stretching method and concludes that wave stretching has small impact on the performance of platforms and it can be ignored in practice.

B.2 Simulation Results

The FOWT with 74 m draft is selected for the simulation, which is the optimal model among all seven new designs (Chapter 2). The normal condition has an incoming hub-height wind speed equal to 21 m/s and the associated wave height and wave period equal to 5.91 m and 12.10 s; the extreme condition has an incoming hub-height wind speed equal to 34 m/s and the associated wave height and wave period equal to 15.49 m and 19.58 s. The uniform current speed for all simulation cases is 1.31 m/s, which is a 50-year current velocity [113]. Five cases are chosen for each of the two conditions to study the influence of current and wave stretching: 1) case one has random wind and wave but no current and no wave stretching; 2) case two has wind, wave, and wave stretching but no current; 3) case three has wind, wave, and current along the wave direction but no wave stretching; 4) case four has wind, wave, current along the wave direction, and wave stretching; 5) case five has wind, wave, current transverse to the wave direction, and wave stretching. The in-house simulator Loose is used for simulation.

Figure B.1 presents comparison of hull pitch displacements for five cases under the normal condition. Mean values of hull pitch displacements of the five cases are -7.84°, -7.77°, -8.42°, -8.37°, and -7.74°, respectively. The stretching effect of the sea surface movement decreases the pitch displacement a little, e.g. cases one and two, and cases three and four. The current traveling along the wave increases the hull pitch displacement by about 0.6°. The current traveling transverse to the wave decreases the hull pitch displacement a little.

Figure B.2 shows comparison of hull roll displacements for five cases under the normal condition. Mean values of hull roll displacements of the five cases are 1.11°, 1.10°, 1.11°, 1.11°, and 1.48°, respectively. Both wave stretching and the current traveling along the wave have little effect on the roll displacement of the floater. The current traveling transverse to the wave has greater impact on the roll displacement because of the direction of the current.

Figure B.3 shows comparison of power output for five cases under the normal condition. Mean values of power of the five cases are 5.65 MW, 5.64 MW, 5.59 MW, 5.59 MW, and 5.66 MW, respectively. Performances of power of the five cases are very close because the active blade pitch control works to maintain the rated generator torque for wind speed greater than the rated speed of the turbine.

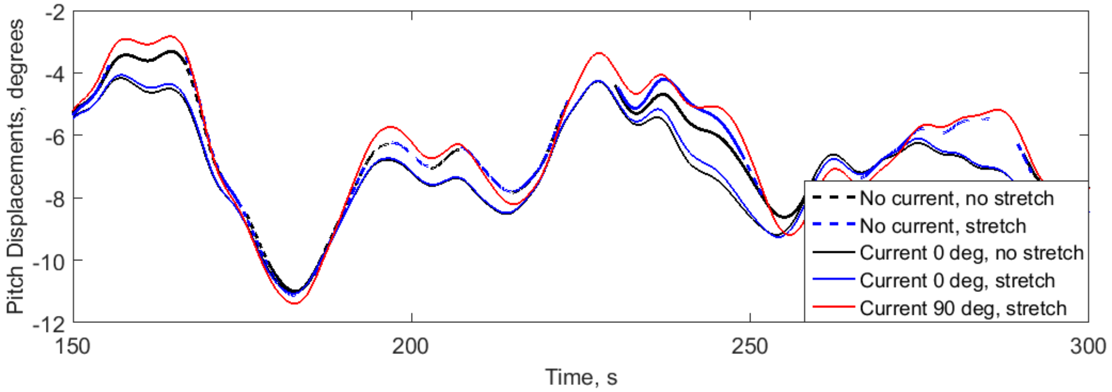

Figure B.1: Comparison of hull pitch displacement for five cases under normal condition.

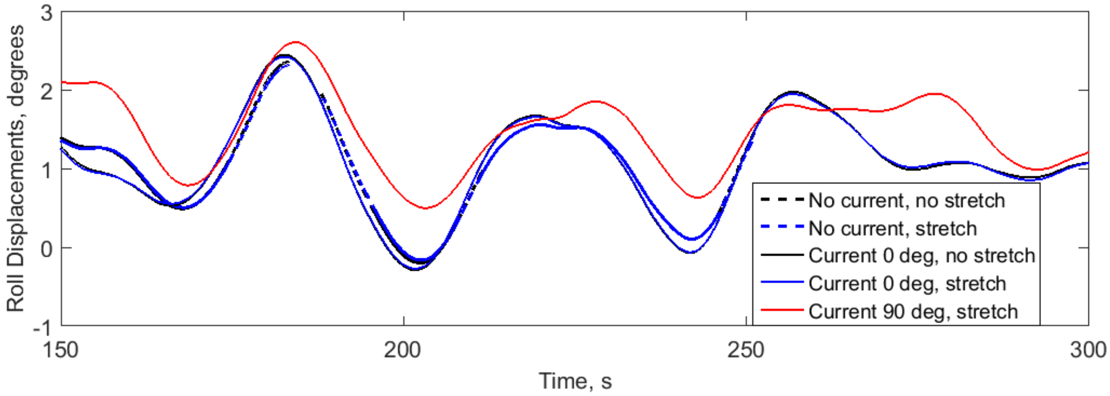

Figure B.2: Comparison of hull roll displacement for five cases under normal condition.

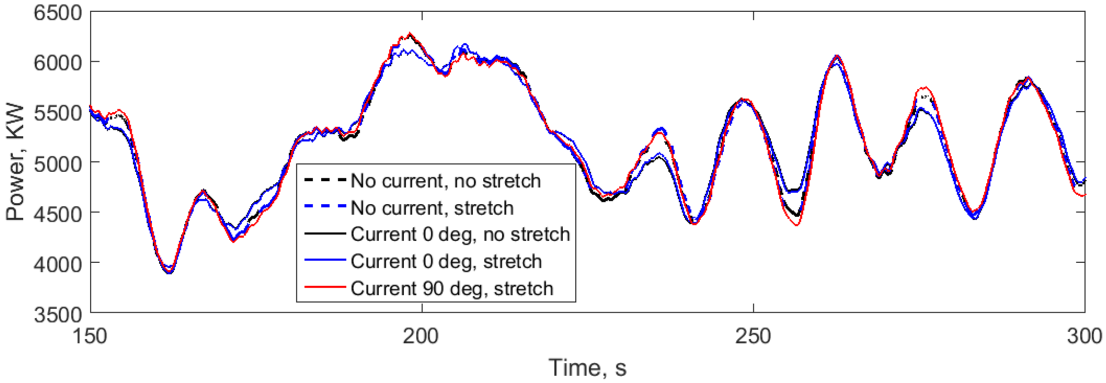

Figure B.3: Comparison of output power for five cases under normal condition.

The effect of currents is not significant for turbines under the normal condition because wind loading acting on turbine blades is dominant. Three more cases for the FOWT with 74 m draft without wind loads and wave stretching are computed to study the effect of currents: 1) no current; 2) current traveling along the wave; 3) current traveling transverse to the wave. Figure B.4 and Figure B.5 show the comparison of hull pitch and roll displacements for these three cases, respectively. Pitch displacements of cases without current and with current transverse to the wave are very close, but the value of case with current along the wave is smaller than that of the other two cases. Roll displacements of cases without current and with current along the wave are very close, but the value of case with current transverse to the wave is greater than that of the other two cases. These results demonstrate that currents have significant influence on hull motions depending on the directions between currents and waves. Wind loads have great effect on the pitch displacement of a FOWT (comparing Figure B.1 and Figure B.4), which decrease the influence from currents.

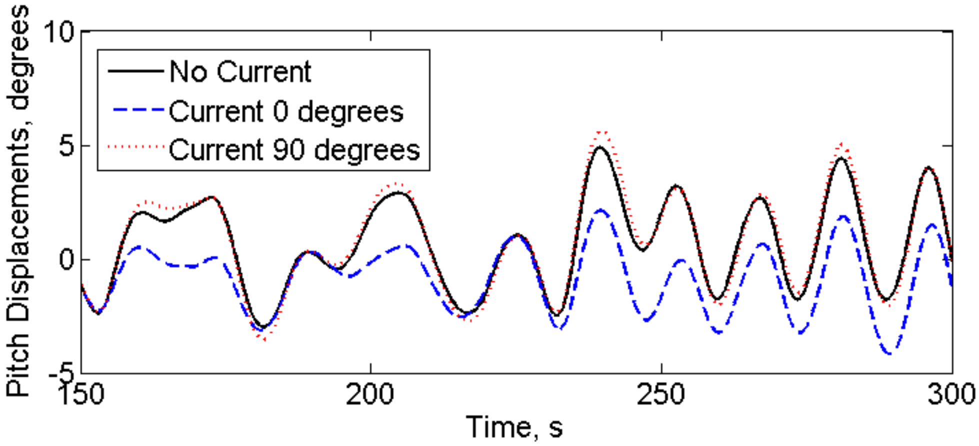

Figure B.4: Comparison of hull pitch displacement for cases without wind loads.

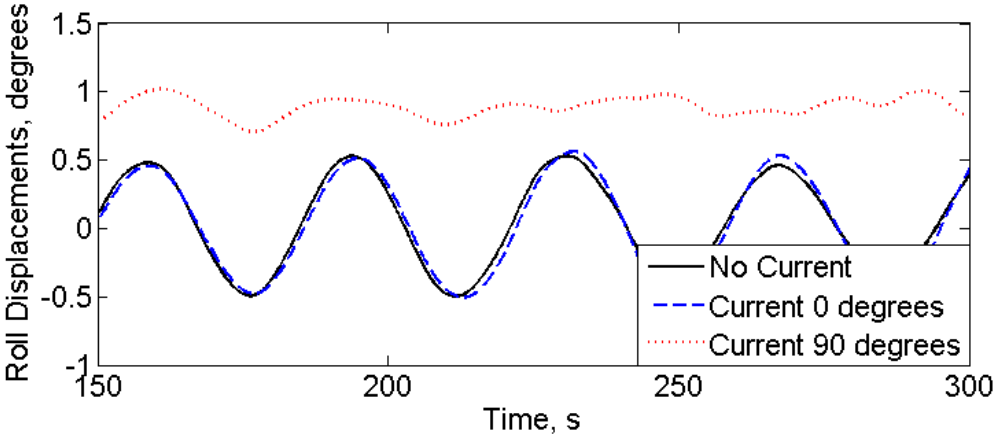

Figure B.5: Comparison of hull roll displacement for cases without wind loads.

FOWT's shut down under the extreme condition and wind loads acting on turbines decrease dramatically. Figure B.6 and Figure B.7 show comparison of hull pitch and roll displacements of five cases under extreme condition. Stretching effects of the sea surface movement on both displacements are slight, which can be found by comparing cases one and two or cases three and four. The variation of pitch motions of floaters experiencing current traveling along the wave is greater than that of floater having current transverse to the wave. The mean value of roll displacement of the case with current transverse to the wave is greater than that of cases with current along the wave. These results demonstrate that influences of currents are much greater than influences of wave stretching. Comparison between cases under the normal condition and the extreme condition demonstrates that effects of currents are more obvious when wind turbines shut down.

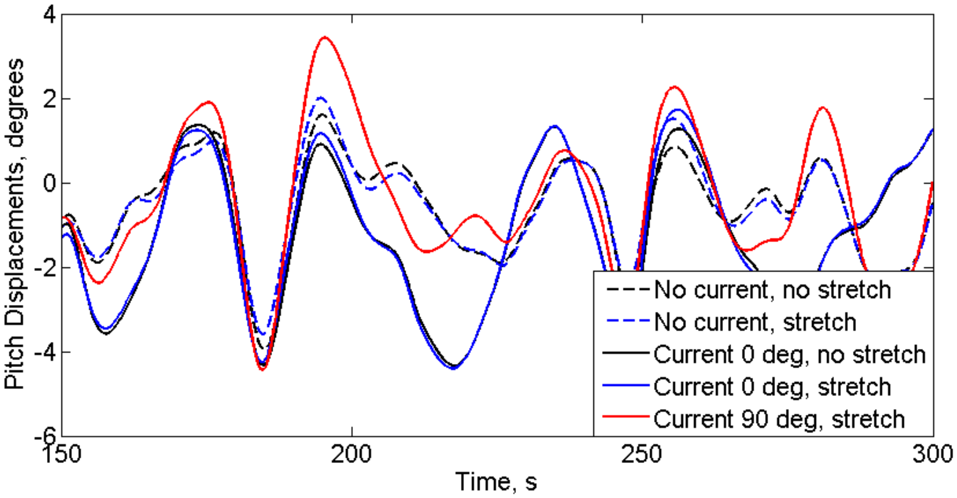

Figure B.6: Comparison of hull pitch displacement for five cases under extreme condition.

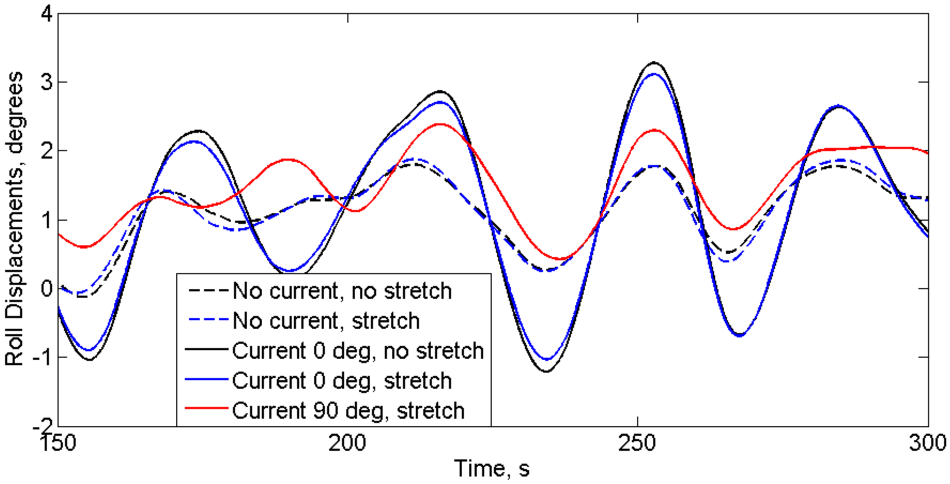

Figure B.7: Comparison of hull roll displacement for five cases under extreme condition.